Local Heat Transfer Coefficients Measured with Temperature Oscillation IR Thermography

Der Fakultät für Maschinenbau
der Helmut-Schmidt-Universität /
Universität der Bundeswehr Hamburg

zur Erlangung des akademischen Grades eines Doktor-Ingenieurs
vorgelegte

DISSERTATION

von

M. Sc. Sebastian Freund

Acknowledgements

This doctoral thesis was written about my research at the Institute for Thermodynamics of the Helmut-Schmidt-University Hamburg. Deutsche Forschungsgesellschaft (DFG) provided the funding for the studies as part of the research project “Wärmeübertragung in komplexen Strömungen”.

Foremost, I like to express my gratitude towards my advisor Professor Dr.-Ing. Stephan Kabelac, who initiated the project and patiently helped me navigating through many difficulties while giving me the freedom for thorough independent research. I like to thank the committee member Professor Dr.-Ing. Heinz Herwig from the Technical University Hamburg-Harburg for the review of this work and the committee Chairman and Dean Professor Dr.-Ing. Franz Joos.

To my dear colleagues and coworkers at the Institut für Thermodynamik and the Helmut-Schmidt-University: Your constant help, encouragement and fruitful conversations have been a great source of support!

I like to thank Professor Tim Shedd and Adam Pautsch of the Multiphase Flow Analysis and Visualization Laboratory at the University of Wisconsin – Madison for the cooperation on the spray cooling project. Also Marc Henze, and Christopher Dietz from the University of Stuttgart and Ulf Ahrend from the Technical University of Braunschweig for the cooperation on the Vortex Generator measurements.

I would also like to thank my former advisors Professor Sandy Klein and Professor Doug Reindl at the University of Wisconsin – Madison, who prepared me well for this work during my M.S. studies.

Last but not least, family and friends: I appreciated your support and understanding for my work during the last years.

Sebastian Freund, Hamburg, December 2007

Abstract

A new method to visualize local heat transfer coefficients on heat exchanger surfaces is presented and numerous experimental measurement results are shown in this thesis. The method relies on IR thermography to measure the heat transferring wall's temperature response to an oscillating heat flux for the calculation of the heat transfer coefficients. The heat flux is generated by periodically modulated laser or halogen light radiation. The IR image data is processed to obtain the phase lag of the temperature oscillation to the heat flux, involving drift compensation, phase synchronization and Fourier transformations. The ill-posed inverse heat conduction problem of deriving a map of heat transfer coefficients from the phase-lag data is solved with a numerical approach based on a complex number 3-D finite-difference method model of the heat- transferring wall. The advantages of this method include that the measurements can be taken contact free at the outside of the heat exchanger wall, that no fluid temperatures or heat fluxes need to be known and that no calibration is necessary. The method was validated and initially employed for the measurement of local convection coefficients on developing pipe flow, agreeing well with correlations.

The mean heat transfer coefficient of a heat exchanger area is calculated either as the arithmetic or as the harmonic mean of the local heat transfer coefficients, depending on whether the boundary condition is a constant temperature or a constant heat flux, for which the mean heat transfer coefficient is lower.

An emphasis in this study is laid on plate heat exchangers; distributions of convection coefficients on various plate areas are obtained. Such locally resolved convection coefficients have not been reported previously. The measurements also allowed investigation of the flow pattern and can be interest for heat exchanger manufacturers. The area-integrated values agree well with established correlations and data from literature. The experimental results are supplemented by CFD simulations of a chevron-type plate heat exchanger cell, aiming at the validation of numerical turbulence models usable for the optimization of plate profiles. The Shear Stress Transport model and an Reynolds Stress Model with explicit algebraic turbulent heat flux model were implemented, leading to CFD results as close as 25% to the area-mean measurement values and clearly showing the shortcomings of current CFD modeling for predicting heat transfer accurately.

The method has also been applied to measure heat transfer on spray cooling systems for high power semi-conductors, showing the distribution of local heat transfer coefficients with previously unrivaled resolution. Further experiments show the convection coefficients surrounding impinging jets of air, as used in many industrial applications. In a joint research project, the heat transfer enhancement on a wind tunnel wall with different arrays of tetrahedral vortex generators proposed for e.g. turbine blade cooling was studied. The results are compared to the data of the project partners using alternative methods based on ammonia absorption and thermochromic liquid crystals and show very good agreement.

Zusammenfassung

In dieser Arbeit wird eine neue Methode zur Messung lokaler Wärmeübergangskoeffizienten vorgestellt und es werden experimentelle Messergebnisse an unterschiedlichen Wärmeübertragern gezeigt. Die Methode basiert auf IR Thermographie zur Messung der Temperaturantwort der Oberfläche eines Wärmeübertragers auf einen schwingenden Wärmestrom, um die innenseitigen Wärmeübergangskoeffizienten zu errechnen. Der Wärmestrom wird mit periodisch moduliertem Laser oder Halogenlampen aufgebracht. Aus den IR Bilddaten werden, nach Temperaturdrift Kompensation und Phasensynchronisation, durch Fourier Transformationen die Phasenverzögerungen zwischen der Wärmestrom- und den Temperaturschwingungen errechnet. Das mathematisch schlecht-gestellte Wärmeleitungsproblem, aus der Phasenverzögerung auf den Wärmeübergangskoeffizienten zurückzurechnen, wird durch ein numerisches Verfahren mit einem 3-D Finite Differenzen Methode Modell der Wärmeübertragerwand iterativ gelöst. Die Vorteile dieser Methode sind, dass die Messung berührungslos an der Außenseite der Wandstattfinden kann, dass keine Fluidtemperaturen oder Wärmeströme bekannt sein müssen und dass keine Kalibrierung notwendig ist. Die Messmethode wurde zunächst an der Einlaufströmung eines Rohres validiert und stimmte gut mit bekannten Korrelationen überein.

Der flächen-gemittelte Wärmeübergangskoeffizient einer Wärmeübertragerfläche wird entweder aus dem flächen-gewichteten arithmetischen Mittel oder aber dem harmonischen Mittel der lokalen Wärmeübergangskoeffizienten berechnet. Dies ist abhängig davon, ob die vorgegebene Randbedingung konstante Temperatur oder konstanter Wärmestrom ist, für den der mittlere Wärmeübergangskoeffizient niedriger ausfällt.

Ein Schwerpunkt dieser Arbeit liegt auf Plattenwärmeübertragern; Verteilungen der Wärmeübergangskoeffizienten wurden über verschiedenen Plattenflächen ermittelt. Solche lokal aufgelösten Wärmeübergangskoeffizienten wurden bisher noch nicht veröffentlicht. Die Messwerte erlauben Rückschlüsse auf die Strömungsverteilung und können für die Hersteller von Wärmeübertragern von Interesse sein. Die flächen-gemittelten Wärmeübergangskoeffizienten stimmen gut mit Literaturdaten überein. Die experimentellen Untersuchungen wurden ergänzt durch CFD Simulationen der Einzelzelle eines Fischgrät-Profil Plattenwärmeübertragers, um numerische Turbulenzmodelle zu validieren um sie zur Optimierung des Plattenprofils einsetzen zu können. Ein Shear Stress Transport Modell und ein Reynolds Stress Model mit explizit-algebraischer Modellierung des turbulenten Wärmestroms wurden eingesetzt. Die Ergebnisse erreichen nur eine Genauigkeit von 25% verglichen mit den flächen-gemittelten Messwerten und zeigen deutlich die Unzulänglichkeiten aktueller CFD Modellierung zur genauen Vorhersage der örtlichen Wärmeübertragung.

Die Messmethode wurde weiterhin zur Messung des Wärmeübergangs an Spray Cooling Systemen für Hochleistungshalbleiter angewendet und zeigt die Verteilung der Wärmeübergangskoeffizienten mit bisher unerreichter Auflösung. Weitere Experimente zeigen die Wärmeübergangskoeffizienten an Prallstrahlen aus Luft, die in vielen industriellen Prozessen zur Anwendung kommen. In einem Verbundprojekt wurde die Erhöhung des Wärmeübergangs an einer Windkanalwand mit unterschiedlichen Anordnungen von

Wirbelgeneratoren, z.B. für Turbinenschaufelkühlung, gemessen. Die Ergebnisse wurden verglichen mit den Daten der Projektpartner, die alternative Messverfahren basierend auf Ammoniak-Absorption und Thermochromischen Flüssigkristallen einsetzen, und zeigen sehr gute Übereinstimmung.

Table of Contents

1 Introduction

"La misère m'empêcha de croire que tout est bien sous le soleil et dans l'histoire; le soleil m'apprit que l'histoire n'est pas tout." [1]

Albert Camus, L'Envers et l'endroit, 1937

1.1 Motivation

As technology progresses and efficiency requirements increase, greater emphasis must be laid upon heat exchanger development to meet the challenge of maximum heat transfer at minimum temperature difference and fluid pressure drop. A precondition for design enhancement with respect to effectiveness is a measurement method that allows quantifying the performance of convective heat transfer. Desirable features of such a method are not only 2-D capability and accuracy, but also swiftness and flexibility. A practical method allowing to resolve local convection effects becomes ever more important to investigate convection and flow features in heat transfer devices ranging from plate heat exchangers over vortex generators to spray cooling systems used in applications as diverse as beer pasteurizing, turbine blade cooling or thermal management of semi-conductors. Measurement data will for instance support the optimization of the corrugation pattern of heat exchanger plates, determine the best options for turbulence promoters to enhance heat transfer on critical components of aircraft engines and predict dangerous hot spots on the surface of sensitive electronics. However, the prevailing methods to measure convective heat transfer either offer no spatial resolution or require a considerable experimental overhead. The research presented in this thesis aims at an advanced measurement method for local heat transfer coefficients; moreover, it shall lead the way towards efficiency improvement of future devices to benefit the economy and the environment.

1.2 Convective Heat Transfer Background

Heat exchangers are major components in power plants, in the chemical and food industry, in HVAC&R, in transportation and many other applications found in everyday life. The performance of heat exchangers depends on the convective heat transfer from the surface to the fluid. The local heat transfer coefficients are responsible for the rate of entropy generation in a heat exchanger and limit the thermal and second-law efficiency of a system. Gaining knowledge of the actual local convection coefficients will lead to performance improvement and subsequently cost and energy savings. For the development and design of

[1] "The misery kept me from believing that all was well under the sun and in history; but the sun taught me that history was not everything."

heat exchangers, engineers rely on correlations or CFD simulations for predicting the heat transfer, both of which in turn rely on precise measurements for validation.

A simple example of how enhanced heat transfer can contribute to saving energy is for instance a boiler providing hot water built as a counterflow heat exchanger. Improved heat transfer, at a given water side heat load, can reduce flue gas waste heat by lowering the flue gas outlet temperature towards the water return temperature. Similarly, improved heat transfer in many processes eventual leads to less waste heat and lower fuel or electric consumption. Another example is the Clausius Rankine cycle, common for power generation or refrigeration applications. Improved heat transfer taking place in the evaporator and the condenser can increase the evaporator temperature and lower the condenser temperature, leading to a better Carnot efficiency, a higher pressure ratio of the working fluid over the turbine of the power cycle or, in the refrigeration cycle, to a lower pressure ratio and lower required compressor power. In a gas turbine, to present a further case in point, improved heat transfer on the blade cooling side to limit the material temperature is a precondition for high turbine inlet temperatures leading to improved efficiency. Such energy-saving advantages come in addition to the obvious fact that improved heat transfer reduces the required area and thus the volume and weight of a heat exchanger, very important e.g. in aerospace applications.

Good introductions to general heat transfer phenomena are given by e.g. Herwig and Moschallski [2006], Baehr and Stephan [2004], Lienhard and Lienhard [2001] and Incropera and DeWitt [1996]; many fundamental heat transfer aspects discussed in this section are lined out in these works. Convective heat transfer, the focal point of this study, is well described e.g. by Merker [1987] and Bejan [1984], very detailed mathematical analysis of convection can be found in the book by Kays, Crawford and Weigand [2005]. Comprehensive references include the Handbook of Single-Phase Convective Heat Transfer [Kakac, Shah, Aung, 1987] and the VDI-Wärmeatlas. Any heat transfer textbook will promptly call attention to the center point of calculating convective heat transfer between a fluid and a solid surface: the heat transfer coefficient. Convective heat transfer coefficients characterize the quality of thermal energy transport between a solid surface and a fluid. The definition of the convection coefficient according to Newton’s law of cooling is:

$$h := \frac{q}{T_{surface} - T_{fluid}} \tag{1.1}$$

This convection coefficient establishes a linear correlation of the heat flux q and the driving temperature difference ΔT between the wall surface and the fluid bulk temperature, $T_{surface}$ and T_{fluid}. A high heat transfer coefficient allows transferring a large heat flux q over a small temperature difference ΔT.

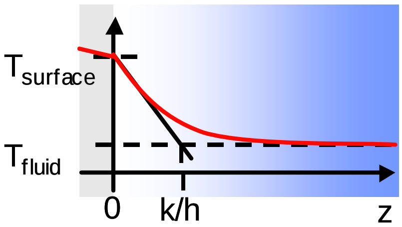

Figure 1.1: Temperature profile of convective heat transfer from the wall (z < 0) into the fluid (z > 0).

Close to a wall surface, the fluid's velocity approaches zero as the fluid sticks to the wall, a region known as the viscous sublayer. In this part of the streaming fluid's boundary layer, thermal conduction is the dominating heat transfer mechanism. Consequently, convective heat transfer depends on conduction over the temperature profile in the viscous sublayer and the temperature gradient near the surface determines the convection coefficient. With conduction in the stagnant fluid near the wall and k the thermal conductivity of the fluid, the heat flux is $q = -k \frac{\partial T}{\partial z}_{|z=0}$, and the heat transfer coefficient becomes $h = -k \frac{\partial T}{\partial z}_{|z=0} \Big/ \left(T_{surface} - T_{fluid}\right)$. The ratio k/h is an illustrative estimation of the thermal boundary layer thickness as shown in Figure 1.1. Typical values for h range from 10 to 1000 W/m^2K for gases and 100 to 10000 W/m^2K for liquids.

Local heat transfer coefficients generally vary over the considered heat transfer area, just as the local temperatures and the heat flux vary. For practical purposes, like heat exchanger layout design, not the local heat transfer coefficients but the mean value h_m is significant, as it factors into the overall heat transfer coefficient. This overall heat transfer coefficient, designated U, includes the inverse of the total thermal resistance between two fluids in a heat exchanger. U multiplied with an equivalent heat-transferring surface area A and divided by the lower fluid heat capacitance rate C_{min} forms the Number of Transfer Units $NTU = UA/C_{min}$, which is a central performance metric for a heat exchanger [Kays and London, 1984]. The relation between the local heat transfer coefficient $h(x,y)$ and the mean value h_m is illuminated in the following. By defining h_m, the total heat flow from the wall surface of a heat exchanger into the fluid becomes

$$Q = A h_m \Delta T_m \ , \tag{1.2}$$

where A is wetted surface area and ΔT_m the mean of the local temperature difference $\Delta T = T_{surface} - T_{fluid} = q/h$, integrated over the area from 0 to x_A and y_A:

$$\Delta T_m = \frac{1}{A} \int_0^{x_A} \int_0^{y_A} \frac{q(x,y)}{h(x,y)} \, dy \, dx \tag{1.3}$$

In convective heat transfer studies and textbooks, two basic boundary conditions are distinguished: constant wall temperature and constant heat flux. Both idealized cases are hardly reached even for instance in evaporators or condensers (constant temperature for pure fluids) or electric heaters (constant heat flux), as the local heat transfer coefficient varies and the wall's thermal conductivity allows lateral heat transfer. Consequently, real applications fall somewhere in between these two ideal cases. Interestingly, the relevant mean heat transfer coefficient h_m as defined in (1.2) is different for these two cases when calculated based on the local values $h(x,y)$. Written as an area integral of the local heat transfer coefficient, h_m becomes for constant temperature ($_T$):

$$h_{m,T} = \frac{1}{A} \int_0^{xA} \int_0^{yA} h(x,y)\; dy\, dx \quad , \tag{1.4}$$

This equation is well known and often appears in literature [e.g. Hausen 1976] when local convection coefficients are averaged. To be strictly mathematically consistent with (1.2) and (1.3), not only the wall temperature, but also the fluid temperature must be constant over the area, so that ΔT becomes a constant. However, when the considered area of constant surface temperature is small and the heat transfer coefficient or the fluid temperature variation is small, the error introduced into the total heat flow (1.2) by using the product of two mean values rather than an exact integration over q also becomes small. For the constant heat flux case ($_q$), to fulfill (1.2) and (1.3), h_m must be different, as the following simple example may point out. Consider a fluid streaming over two surface areas of 1 m^2 each and a constant heat flux of q = 10 kW/m^2 applied to both areas. The heat transfer coefficient on the first area be h_1 = 10000 W/m^{2}K, while the heat transfer coefficient over the second area be h_2 = 2000 W/m^{2}K. Now equation (1.3) yields the correct ΔT_m = 3 K, which becomes clear when assuming a sufficiently high fluid capacitance rate that the bulk temperature stays at 0°C and the surface temperatures become T_1 = 1°C and T_2 = 5°C, for the first and the second area, respectively. The mean heat transfer coefficient as defined in equation (1.2) becomes $h_{m,q} = q/\Delta T_m$ = 3333 W/m^{2}K. In contrast, using equation (1.4) to evaluate h_m from averaging h_1 and h_2 delivers the erroneous value of 6000 W/m^{2}K, which, at the given heat flux q would give an erroneous ΔT_m of only 1.666 K. This example demonstrates that equation (1.4) is strictly invalid for constant q and that a different formula has to be found. Such an equation can be derived by setting $h_{m,q} = q/\Delta T_m$ from equation (1.2) and substituting equation (1.3) for DT_m : $h_{m,q} = q \Big/ \frac{1}{A} \int_0^{xA} \int_0^{yA} \frac{q(x,y)}{h(x,y)}\, dy\, dx$. The constant q cancels out and the total area A can go into the numerator; h_m for the constant heat flux case ($_q$) becomes

$$h_{m,q} = \frac{A}{\int_0^{xA} \int_0^{yA} \frac{1}{h(x,y)}\, dy\, dx} \quad . \tag{1.5}$$

Equation (1.5) delivers for the example above $h_{m,q}$ = 1 m^2 W/m^{2}K / (0.00005+0.00025)m^2, leading to the correct value $h_{m,q}$ = 3333 W/m^{2}K.

This distinction of forming the mean heat transfer coefficient depending on the thermal boundary conditions is especially important when reporting the mean of measured local convection coefficients that vary widely over the area. For discrete measurement data, the integrals in equations (1.4) and (1.5) degenerate into summations and $h_{m,T}$ becomes the area-weighted arithmetic mean while $h_{m,q}$ is the area-weighted harmonic mean; at equal grid spacing, the weights become unity and A becomes the count of the measured points.

When neither the heat flux q nor the temperature difference ΔT approach constant conditions over the area, the rigorous mathematical solution for the mean heat transfer coefficient also accounts for q as it cannot be cancelled out. Consistent with the definitions (1.2) and (1.3), h_m for arbitrary boundary conditions becomes:

$$h_m = \frac{\int_0^{xA}\int_0^{yA} q(x,y)\; dy\, dx}{\int_0^{xA}\int_0^{yA} \frac{q(x,y)}{h(x,y)}\; dy\, dx} \tag{1.6}$$

This equation, which follows directly when substituting (1.3) into (1.2), is rather impractical to use as it requires a priori the distribution of $q(x,y)$. The value of h_m (1.6) coincides with $h_{m,T}$ and $h_{m,q}$ for constant ΔT respectively constant q. For other boundary conditions, h_m is above $h_{m,q}$ and below $h_{m,T}$; the deviations of $h_{m,q}$ and $h_{m,T}$ from h_m depend on how closely the respective boundary conditions are approximated and on the variation of $h(x,y)$. The geometric mean of $h_{m,q}$ and $h_{m,T}$ will give a reasonable estimate of h_m for unknown or mixed boundary conditions.

From a thermodynamic perspective [Baehr and Kabelac, 2006], it is of interest to consider the entropy generation in a heat exchanger [Herwig and Kautz, 2007] as the convective heat flux q undergoes a change in temperature from $T_{surface}$ at the wall to T_{fluid} (with the heat flux counted positive when going into the fluid). A Second Law entropy balance of the convective heat transfer across the boundary layer yields an area-specific local entropy generation rate $\dot{s}_{irr} = q/T_{surface} - q/T_{fluid}$ at the heat-transferring surface. Substitution of $T_{fluid} = T_{surface} - q/h$ and rearrangement leads to the area-specific local entropy generation rate $\dot{s}_{irr}$ as a function of the heat flux, the wall temperature and the local heat transfer coefficient, not accounting for the fluid pressure drop:

$$\dot{s}_{irr} = \frac{1}{h}\,\frac{q^2}{T_{surface}\left(T_{surface} - \dfrac{q}{h}\right)} \tag{1.7}$$

In the equation above, $T_{fluid} + q/h$ can be substituted for $T_{surface}$. It is evident that $\dot{s}_{irr}$ becomes smaller for a larger heat exchanger with lower heat flux and a high heat transfer coefficient operating at high temperature. As T, q and h are generally variable over the length of the flow path x in a heat exchanger with a constant wetted perimeter length L, an integration over the flow length x delivers the total entropy generation rate:

$$\dot{S}_{irr} = L\int_0^x \dot{s}_{irr}\; dx \tag{1.8}$$

Equation (1.7) and (1.8) reveal the fundamental mechanism limiting a heat exchanger's effectiveness, as availability (exergy) is being destructed with $T_0\dot{S}_{irr}$ at a rate proportional to $1/h$ at a given heat flow, area, surface temperature and ambient reference temperature T_0. Consequently, the heat transfer coefficient is directly responsible for the minimum temperature difference, the effectiveness and the availability losses in a heat exchanger. Efforts must be undertaken to experimentally quantify this decisive number in order to optimize convective heat transfer.

A holistic approach of heat exchanger optimization with respect to minimum entropy generation [Bejan, 1996] must also take into account the pumping power P_{diss} that dissipates in the volume flow rate $\dot{V}$ while overcoming a frictional pressure loss Dp within the heat exchanger: $P_{diss} = \dot{V}\Delta p$. P_{diss} is thereby converted into a heat flow at the temperature T_{fluid}, generating entropy at a rate of $\dot{S}_{irr} = P_{diss}/T_{fluid}$. With the Darcy-Weisbach friction factor in a duct of hydraulic diameter D_h, $f = \frac{2D_h}{r\,\mathrm{v}^2}\frac{dp}{dx}$, with the fluid density r and the mean velocity v, the area-specific irreversible entropy rate of the dissipated pumping power becomes

$$\dot{s}_{irr} = \frac{f}{8}\frac{r\,\mathrm{v}^3}{T_{fluid}} \quad . \tag{1.9}$$

This equation yields the entropy generation rate due to frictional pressure losses when integrated analogous to (1.8). The friction factor and the heat transfer coefficient often can be related by the Reynolds analogy, as in most situations the mechanisms that enhance heat transfer also increase friction. An approximate and limited but nonetheless exemplary relation found in literature [e.g. Baehr and Stephan, 2004, Bejan, 1984] with Colburn's *j-Factor* for turbulent pipe flow is:

$$\frac{f}{8} \approx j = \frac{Nu}{Re\,Pr^{1/3}} \tag{1.10}$$

The objective function to be minimized becomes the integral over the sum of (1.7) and (1.9) with respect to the flow length x. Correlations linking f and h with the geometric parameters and fluid properties for the considered type of heat exchanger have to be substituted into (1.7) and (1.9). Such correlations for f and $Nu(f, Re, Pr)$ are given e.g. by Filonenko [1954] and Gnielinski [1975] for pipe flow or by Martin [2002] for plate heat exchangers. Constrains of the optimization are e.g. size and costs. Practical correlations rely on measured data for different geometries and flow conditions. As one integral part of such a heat exchanger optimization strategy, this study will focus on providing measurements of the crucial local heat transfer coefficients with a new method based on temperature oscillations.

Temperature oscillation techniques have been used in heat transfer research for decades. The underlying concept of these methods is to supply periodic modulated thermal energy to a system and measure its temperature response. The measured amplitude and phase of the temperature response is compared to a mathematical solution of a system model. System parameters such as heat transfer coefficients and material properties may be derived from the solution. Characteristics of temperature oscillation techniques are simplicity and no need for calibration. The major challenge lies in the formulation of an appropriate model and the mathematical solution of the temperature response as well as the processing of the measured data. None of the previously developed temperature oscillation techniques for heat exchanger analysis could yield spatially resolved local convection coefficients from a 3-D system model.

The method introduced in this study allows the measurement of local convective heat transfer coefficients on heat exchanger areas with high spatial resolution. This new method is based on Temperature Oscillation IR Thermography, radiant heating and a three-dimensional numerical system model. The method is contact-free and fluid-independent. A schematic of the measurement setup is shown in Figure 1.2:

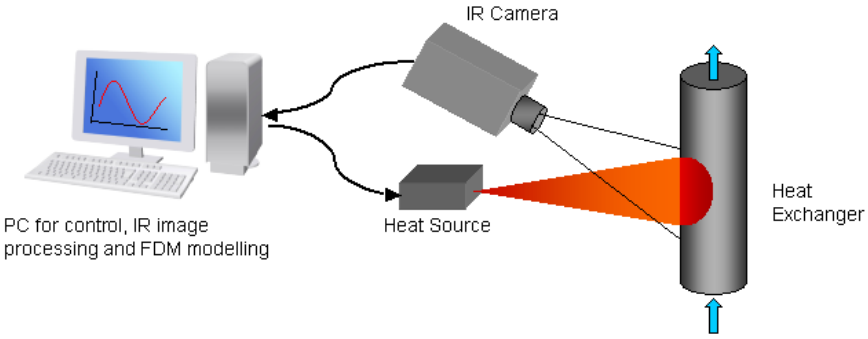

Figure 1.2: Schematic of the measurement setup.

In this thesis, the development of the Temperature Oscillation IR Thermography (TOIRT) method is illustrated and various experiments applying this method are reported. These experiments include convection measurements in pipe flow, at aerodynamic vortex generators in a wind tunnel, at impinging jets, in spray cooling systems and in plate heat exchangers. Finally, the measurement results from the plate heat exchanger are used for the validation of CFD models for turbulent heat transfer that are developed by project partners at the ITLR at the University of Stuttgart. CFD simulations of the heat transfer in different heat exchangers can be carried out with these models in order to optimize the geometry to maximize performance while minimizing pressure loss. Such improvements, made possible due to detailed convection measurements, can lead to the aforementioned benefits of cost and energy savings in future heat exchangers.

2 Previous Research

Convective heat transfer is most commonly measured with a steady state technique that directly provides the heat transfer coefficient from the heat flux and the temperatures according to equation (1.1). Typically, a known heat flux is applied electrically and the surface and fluid temperatures are measured e.g. with thermocouples. When high spatial resolution of surface temperature measurements is required, thermochromic liquid crystals (TLC) or IR thermography are used [Astarita, 2000]. By measuring the color or the hue of the TLC layer the temperature can be calculated after careful calibration [Farina et al. 1993], although in a narrow range. The application of this measurement technique for mapping heat transfer coefficients is well described by Stasiek [1997]. Hohmann and Stephan [2002] used microscale TLC with very high spatial and time resolution to study evaporation phenomena. Considerable drawbacks of such steady state methods are that the local heat flux and the fluid temperature must be known exactly, adding to the experimental complexity. IR thermography allows quick local temperature measurements when calibrated, while TLC's increase the measurement overhead but allow very accurate temperature measurements.

Another technique to measure local heat transfer is the ammonia-absorption method. The amount of absorbed ammonia on a filter paper sheet impregnated with manganese chloride changes its color. The paper sheet covers the heat transfer area, and without actual heat transfer, the convection coefficients can be obtained from a heat-mass transfer analogy through image processing of the paper sheet's color after careful calibration. Advantages of this method are that neither flow interaction with measurement devices occurs, nor does the evaluated structure need to be optically accessible. However, to evaluate the color of the paper, the structure has to be disassembled after the measurement. Since it is based on absorption from a streaming gas, the range of fluids is very limited. Experiments are usually carried out in a wind tunnel; the technique has been used e.g. by Ahrend et al. [2006] and Gaiser and Kottke [1989] for plate heat exchangers. The AAM requires precise knowledge of the local chemical composition in the fluid, unless the color change is calibrated in each measurement directly to a Nusselt number correlation applicable to a certain region unaffected by the studied flow features [Ahrend et al., 2006].

A very different approach to measure convective heat transfer is based on temperature oscillations, described in the following.

2.1 Overview of Temperature Oscillations Techniques

Early work on temperature oscillations in heat transfer research was performed since the 1930's by Hausen [1976] and coworkers in the analysis of regenerators. Large regenerative heat exchangers such as cowpers, used for furnaces in iron processing, and Ljungstrøm air pre-heaters used in coal fired power plants, were examined.

Bell and Katz [1949] presented a method of calculating the convection coefficient on the surface of small channels inside copper and brass specimen. An electric heater induces sinusoidal temperature variations into an air stream; the air temperature before and after passing the specimen is measured. The amplitude ratio of the measured temperatures is compared to a one-dimensional analytical solution derived from an energy balance. Three approaches regarding the thermal conductivity of the specimen are investigated, leading to very similar amplitude ratios. The final solution yields an average convection coefficient in the channels.

Matulla and Orlicek [1971] investigated the mean convective heat transfer coefficients in coaxial tube heat exchangers using temperature oscillations. Temperature oscillations are imposed on the fluid in the inner tube, the temperatures at the entrance and exit of the outer tube flow are measured with thermistors. The convection coefficient is derived from comparing the amplitude ratio of the experimental data to an analytical solution in an iterative process.

Carloff [1994] measured the heat transfer coefficient of the wall of a polymerization reaction tank. An electric heater induces temperature oscillations in either the fluid or the wall, the reactor and the wall temperatures are measured. An integrated energy balance over one oscillation period yields the overall heat transfer coefficient of the reactor wall. The results show a large decrease of the heat transfer coefficient over the 200 min. reaction time of a methyl-methacrylate polymerization process.

Roetzel et al. [1994] applied a temperature oscillation technique for the investigation of the heat transfer performance (NTU) and the axial dispersion coefficient of a plate heat exchanger. Axial dispersion is an effective longitudinal conduction in heat exchangers or porous media due to flow maldistribution within multiple passages, convective mixing and conduction in solid walls. The temperature oscillations are induced into one fluid loop of the heat exchanger by using electric heaters and cooling water. The other fluid loop of the heat exchanger stays dry. The entrance and exit temperatures of the fluid are measured. The NTU and an axial dispersion Peclét Number were calculated by comparison of the measured phase shift and amplitude attenuation to an analytical solution. Plate heat exchanger characteristics such as U-type flow (leading to increased phase-lag) and plate thickness (limited penetration depth and effective thermal capacity depending on the oscillation frequency) are considered. The results are compared to Nusselt Numbers derived from steady state tests and show good agreement at low Reynolds Numbers. For higher flow rates, the transient experiments indicate higher heat transfer, which is attributed to dispersion effects that are not considered separately in steady state measurements. The results from these experiments are particularly useful when the transient behavior of heat exchangers is of interest.

Similar to temperature oscillation techniques, although not periodic, is a method based on the wall temperature's response to a step change in the fluid temperature and an analytical solution assuming a semi-infinite wall. The time dependent temperature change of the heat transfer surface is recorded with either IR thermography or TLC's and CCD digital video, the bulk fluid temperature can be measured with thermocouples. Recently employed by Henze et al. [2007] for measuring heat transfer coefficients on an array of vortex generators, this method proved to be accurate with a very high spatial resolution. An advantage is that for this transient method the local heat flux needs not to be known. However, the method requires a heat exchanger model with thermally semi-infinite walls when using an analytical solution, optical access to the surface and means of providing a step change of the fluid temperature.

2.2 Infra Red Thermography in Heat Transfer Research

Although the methods above give fair results of the average convection coefficients or the NTU (Number of Transfer Units) of complete heat exchangers, no knowledge of the local convection coefficients and their spatial distribution can be derived from these experiments. Temperature measurements that are taken with thermocouples that are wall-mounted or inside a fluid stream have very limited spatial resolution, places inside heat exchangers may be difficult to reach and the probes may cause interactions. IR thermography is a contact-free technique for temperature measurements; no probes interact with the surface and can disturb the measurements. IR thermography cameras allow high spatial resolutions of surface temperatures. The immediate response of IR cameras to rapid temperature changes perfectly suits this technology for transient effects. However, thermography is limited to outside surfaces.

IR thermography is based on the emission of IR radiation of a surface. Wavelength and intensity depend on the temperature and emissivity according to Planck's Law, equation (2.1):

$$E_l = e(l)\frac{C_1}{l^5\left(e^{C_2/lT}-1\right)} \tag{2.1}$$

Here E_l is the monochromatic radiation intensity, $e(l)$ is the hemispherical spectral emissivity, l is the wavelength, C_1 = 3.7418·10^{-16} Wm^2 and C_2 = 14.388·10^{-3} mK are the radiation constants and T is the absolute temperature. The infrared spectrum begins above the visible light at 750 nm and reaches to 1000 µm. It is generally subdivided into four bands: near infrared, medium infrared, far infrared and extreme infrared. The derivative of Planck's Law with respect to the wavelength gives the wavelength at the maximum intensity (2.2), known as Wien's Displacement Law:

$$l_{\max} = 2898\,\mu\mathrm{mK}^{-1}/T \tag{2.2}$$

Surfaces at room temperature emit infrared radiation with the peak intensity around 10 µm in the far infrared band with wavelengths of 6 – 15 µm.

An overview of IR thermography in heat transfer research within the last decades is given by Astarita [2000]. Thermography was mainly employed in combination with thin-film surface heating. The experiments included external flow from impinging jets to various aerodynamic bodies such as airfoils, wings and space shuttle models, as well as internal flow through duct steps and turns. Nusselt numbers could be derived from known heat flux and surface temperature maps. Free convection Nusselt and Grashoff numbers are evaluated by Farid [1991] at a steady state heated horizontal cylinder by means of IR thermography. Using the Boundary Element Method, the heat flux and the local convection coefficients are obtained from the numerical solution for the surface temperatures at every node.

2.3 Temperature Oscillation IR Thermography

IR thermography in combination with temperature oscillations for heat transfer measurements is a new technique that rarely appears in literature. That technique has been used by Prinzen [1991], Wandelt [1997], Roetzel [1997] and Turnbull [2002]. The groundbreaking work of Prinzen and Wandelt will be discussed in detail because of their significance for the current project. Prinzen's and Wandelt's work also exemplary demonstrates the principle of Temperature Oscillation IR Thermography. Turnbull [2002] employs IR thermography and square wave modulated thin film heater to investigate the convection coefficient on the surface of model turbine blades. A sinusoidal temperature response function is extracted from the measured data by means of bandpass filtering and Fourier transformations. Turnbull and Oosthuizen [1998] present a one-dimensional analytical solution for periodic heat flux generated in a foil heater with surface convection on a semi-infinite substrate. The analytical solution agrees very well with a numerical solution using a finite difference model. The convection coefficient can be derived from the phase-delay of the temperature oscillations on the heater surface.

2.3.1 The Prinzen Method

Likely the first practical Temperature Oscillation IR thermography method has been developed by Prinzen [1991] and Roetzel. The method allows the calculation of local convective heat transfer coefficients inside tubes and vessels. The method is contact-free and requires no knowledge of fluid properties or temperatures. The Temperature measurements are only taken on the outside surface of a heat-transferring vessel with an IR scanner. The temperature oscillations are induced into the vessel by laser spot heating of the wall. The laser output is modulated to square pulses with known frequency by a rotating aperture. Originating from the laser-heated spot, the heat is diffused in radial direction into the wall material, causing a concentric temperature wave.

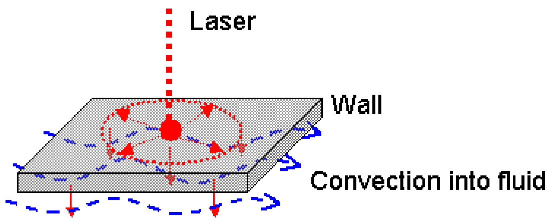

Figure 2.1: Laser spot heating the wall, radial conduction and convection.

The conduction along the wall can be described by Fourier's Law of heat conduction (2.3). On the fluid side, the temperature difference between the wall and the fluid leads to convective heat transfer into the fluid according to Newton's Law (2.4).

$$q_{cond} = -k\nabla T \tag{2.3}$$

$$q_{conv} = h\Delta T \tag{2.4}$$

Both, the convective heat transfer and the thermal diffusion, increasingly attenuate and phase-shift the temperature wave propagating along the wall. Thus, the amplitude and phase-shift of the temperature oscillations are functional related to both, the radial distance from the heated spot and the convection coefficient. Knowledge of either number allows calculating the other; the method can be used to for the evaluation of the thermal diffusivity as well. For calculating the convection coefficient, density, conductivity and capacitance of the wall material are required.

An analytical solution of this conduction-convection problem has been found by Prinzen and Roetzel under a few simplifying assumptions. First, the thermal diffusivity of the material is constant and isotropic. Second, the convection coefficient is constant within the area of analysis. Third, no thermal gradient exists perpendicular to the wall, i.e. the wall is thin. Fourth, the system has a steady-periodic state without transient effects. Now the problem can be reduced to heat conduction (thermal conductivity *k* and diffusivity *a*) in a symmetric cylindrical plane (thickness *d*) with a negative volumetric generation term due to fluid side convection *h*, equation (2.5):

$$\frac{\partial^2 T}{\partial r^2} - \frac{1}{r}\frac{\partial T}{\partial r} = \frac{1}{a}\frac{\partial T}{\partial t} + \frac{h}{kd}T \tag{2.5}$$

The analytical solution has been derived from an approach of complex combination and Bessel functions K_0 (originating from the cylindrical coordinates) in analogy to Myers [1971]. The solution yields equations for the amplitude ratio, the mean temperature ratio and the phase-shift as a function of the radius and the convection coefficient. It has been shown by Prinzen as well as by Roetzel, Wandelt [1997] and Turnbull [2002], that using phase-shift data in the analysis bears the least errors. Henceforth the phase information only is used in the calculation of the convection coefficient. The phase-shift f between the steady oscillating temperatures of two measurement points *1* and *2* is given as equation (2.6):

$$\tan f = \frac{\mathrm{Im}\left\{\dfrac{\mathrm{K}_0(x_1\sqrt{y+i})}{\mathrm{K}_0(x_2\sqrt{y+i})}\right\}}{\mathrm{Re}\left\{\dfrac{\mathrm{K}_0(x_1\sqrt{y+i})}{\mathrm{K}_0(x_2\sqrt{y+i})}\right\}} \tag{2.6}$$

Here $y = \dfrac{ha}{kdw}$ is the dimensionless convection coefficient and $x = r\sqrt{\dfrac{w}{a}}$ is the dimensionless radius *r* measured from the laser spot heated with the angular frequency *w*.

The phase-shift is calculated by applying a Fourier analysis to the temperatures at the pixels of a measurement point in a time-step series of IR images. In theory, the convection coefficient can be calculated when the temperature response phase-shift and the radii measured from the heated spot of any two points within the area of analysis are known. However, due to measurement inaccuracies and errors, individual measurement points are relatively unreliable. For that reason a high number of measurement points are evaluated and treated with statistical methods to even out random variations and errors. A regression polynomial of second order of the phase lags of all measurement points over the radius is calculated. From this regression polynomial, two statistically averaged artificial measurement points are derived. Finally, the phase-shift between these two measurement points is used to iteratively calculate the convection coefficient by comparison with the analytical solution (2.6).

Finite element computations were carried out by Prinzen in an effort to investigate the influence of real conditions versus the simplifying assumptions of the analytical solution. It turned out that, for the expected range of parameters of the actual experiments, an axial wall temperature gradient, slightly varying fluid temperatures or small un-periodic variations of the heat flux had little effect and the FEM model showed good agreement with the analytical solution. Since the fluid temperature is not strictly constant within the range of the heated zone as the fluid warms up, the temperature field of the wall is not exactly symmetrical around the heated spot. This results in measured convection coefficients that are different depending if the location is after or before the heated spot with respect to the fluid flow. To compensate for this error, Prinzen suggests to use the arithmetic mean values of convection coefficients measured on locations symmetrically arranged around the heated spot. Random signal variations from the infrared detector, noise, cause inaccuracies when the signal-noise ratio is low or the number of time steps is small. Prinzen points out that the harmonic analysis averages the noise during the time-step integration of the Fourier analysis and extracts the underlying sine function of the temperature response fairly accurate.

Prinzen's experimental setup includes an Ar-Ion laser (3.5 W, ca. 500 nm) with a rotating aperture for heat flux modulation, an Agema 880 LWB IR scanner with a spatial resolution of 140 x 140 pixel, 6.25 images per second and an accuracy on the order of 0.1 K, and a PC with a camera interface for IR image and data processing. Experiments were first carried out for a copper and steel tube in a thermostatic and flow rate controlled water cycle, where the convection coefficient is well known from Nusselt number correlations. The experimental results from the tubes agree to data calculated using Gnielinski's Nusselt number equation [Gnielinski, 1975]. It is therefore concluded that the assumptions made in the analytical solution are valid. Further experiments considered a stirred reactor vessel with unknown inside convection. The results in form of Nusselt numbers were compared to limited literature data on stirred tank heat transfer. Beyond these experiments proving feasibility on the tubes and the measurements on the stirred reactor vessel, no attempt was published to further develop this method for other applications.

Even with good agreement found between the convection coefficients inside the tubes and literature data, the method has a few constrains and limitations that arise from the measurement principle and the conditions the analytical solution is based on. First, the method is limited to thin-walled structures without an axial temperature gradient. Second, the convection coefficient has to be constant within the zone of analysis between the measurements points. Third, the spatial location of every pixel to be considered for the measurement must be known exactly relative to the heated spot. Most importantly, measurements of sizeable areas with varying convection coefficients have to be performed in a grid like fashion point by point. This can be a time consuming procedure when the whole object surface is covered. Generally, the method is not suited for sizeable heat exchanger areas with varying convection coefficients.

2.3.2 The Wandelt Method

The method developed by Wandelt and Roetzel [1997] allows for evaluation of local convection coefficients on either side of a uniform heat-transferring wall. The advantages of this method compared to Prinzen's are, that first the convection coefficients do not have to be constant over the evaluated area and second, that all measurement points in the area can be estimated at once within a few oscillation periods. Similar to Prinzen's method, it also relies on a laser for modulated surface heating and an infrared camera for surface temperature measurements. Again, only contact-free temperature measurements and radiant heating are necessary, only knowledge about the wall material is required and the phase-lag information on each measurement point is used for computation of the convection coefficient.

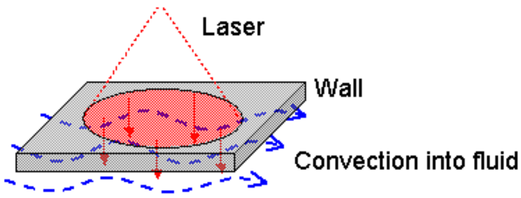

Figure 2.2: Uniform heating of the wall, axial conduction and convection.

The principle is different from Prinzen's method. The radiant heating effects not spot wise, but uniform-laminar by means of a fiber coupled laser with a wide beam. Thus, contrary to Prinzen's method, the temperature wave propagates perpendicularly through the material rather than laterally along the surface. Any lateral conduction is neglected. The analytical approach is based upon one-dimensional conduction through a slab:

$$\frac{\partial^2 T}{\partial z^2} = \frac{1}{a}\frac{\partial T}{\partial t} \tag{2.7}$$

The boundary conditions are generation terms including the convection coefficients h_0 (inside) and h_d (outside) at constant fluid temperatures and the radiant heat flux at the outside surface, where the temperature $T(z=d,t)$ is to be evaluated. Equation (2.7) with these boundary conditions has been solved by applying the Laplace transform. Further mathematical steps are omitted here for the sake of brevity. The solution of the temperature response phase lag at the surface is given as (2.8):

$$\tan f = \frac{c_1 + 2xy_0 c_2 + 2x^2 y_0^2 c_3}{2xy_0\left(1+\frac{h_d}{h_0}\right)c_0 + 2x^2 y_0^2\left(1+2\frac{h_d}{h_0}\right)c_1 + 4x^3 y_0^3 \frac{h_d}{h_0} c_2 + c_3} \tag{2.8}$$

Here the parameters are

$$
\begin{aligned}
c_0 &= \cosh^2 x \cos^2 x + \sinh^2 x \sin^2 x \\
c_1 &= \cosh x \sinh x + \cos x \sin x \\
c_2 &= \cosh^2 x \sin^2 x + \sinh^2 x \cos^2 x \\
c_3 &= \cosh x \sinh x - \cos x \sin x
\end{aligned}
$$

with the dimensionless convection coefficient $y_0 = \dfrac{h_0 a}{kdw}$ and the thickness $x = d\sqrt{\dfrac{w}{2a}}$.

The temperature response phase-lag f is derived from a series of infrared images by applying Fourier analysis to every pixel. The images have to be recorded synchronized to the heat source modulation after the temperature oscillation reaches steady state and transient effects are diminished. When the images series range over a few oscillation periods, the Fourier analysis filters the detector noise and extracts amplitude, mean temperature and phase of the oscillation.

To demonstrate the feasibility and accuracy of the method, an experiment was carried out to evaluate local heat transfer coefficients and compare the values with well-established equations. The convection coefficients were measured on the surfaces of a thin copper plate of 25 x 7 mm in a laminar air stream. A fiber-coupled laser diode array with a wavelength of 685 nm providing 15 W optical power is used as a heat source. An Agema Thermovision 900 LWB IR scanner records the surface temperatures with a spatial resolution of 272 x 68 pixels and 30 frames/s. The results show agreement on principle between the experimental heat transfer coefficients and values from literature, but local errors are considerable.

Although Wandelt's method has proven feasible in very limited experiments, it bears great difficulties associated with lateral conduction in the wall. Variations of the local surface emissivity e.g. due to differences in surface oxidation or stains cause the calculated temperatures to be inaccurate. The computation of temperatures from the infrared detector's signals assumes constant emissivity over the focused area; also, the absorption of the heating energy will vary, leading to non-uniform heat flux. The way to overcome this problem is coating the surface uniformly with blackbody paint of exactly known emissivity. For the calculation of the phase-lag, the local emissivity is not essential. However, non-uniform surface heat flux induces lateral temperature gradients and leads to a smaller phase-lag at positions with higher heat flux; a radiant heat source providing uniform heat flux is difficult to come by.

Since the method is based on a one-dimensional analytical approach that neglects lateral thermal conduction, it is principally unsuited to evaluate locally varying convection coefficients, unless the gradients are small and the wall is thin. The higher the gradients of the convection coefficients over the evaluated area and the higher the wall conductivity and thickness, the more will lateral conduction influence the local surface temperature phase delay; the phase delay will not correspond to the actual local convection coefficients according to the one-dimensional solution (2.8).

Wandelt's method is in comparison to Prinzen's approach a step further towards a practical measurement technique; it allows the quick evaluation of sizeable areas with limited local variation of convection coefficients. However, when significant lateral conduction comes into play, the analytical approach is no longer valid.

2.3.3 Lock-In Thermography

Currently an infrared imaging method based on the preceding principle of temperature oscillation thermography that is known as Lock-in Thermography is industrially used for non-destructive testing of materials. Like Wandelt’s method, periodically modulated thermal energy is uniformly supplied to the target surface e.g. by lamps. A thermal wave of absorbed energy propagates into the material. An infrared camera measures the thermal response of the inspected surface over a few oscillation periods after steady periodic state has been approached. The temperature data for each pixel is recorded in a sequence of images. Each pixel sequence undergoes Fourier transformation and harmonic analysis. Rather than calculating heat transfer coefficients as mentioned above, the applied methods create an image based on either the surface temperature response phase shift or the amplitude at each pixel’s position. Thereby the differences in thickness and thermal diffusivity caused by flaws within the material or between layered materials are made visible. Examples for the application of this method are laminated compound structures for aircrafts and automobiles and quality control on surface coatings [AT, 2004].

Lock-In thermography was studied on various reinforced plastic samples by Meola [2002]. The samples were prepared with holes and delaminations. In addition, a steel sample was checked for welding defects. The penetration depth of the thermal wave that limits the depth in the material beyond which no information can be observed at the surface depends to the oscillation frequency and the thermal diffusivity. They give a penetration depth of $d = 1.8\sqrt{2a/w}$. Repeated measurements with variation of the frequency until material flaws become visible in the image allows the depth to be calculated, thus offering 3-D analysis capabilities.

Lock-In Thermography is also applied to determine thermal properties of materials. Meola [2002] measures the thermal diffusivity of various samples with known thickness based on the penetration depth by adjusting the frequency. Horny [2003] evaluates the conductivity of an epoxy coating with a lock-in thermography method that is similar to the method of Prinzen [1991]. An analytical solution of a periodic 2-D conduction equation for a cylinder plane including the heat source is found by means of a Hankel transform. The phase-lag information is used because of its independency of experimental parameters, as opposed to the amplitude. An Ar-ion laser with an acousto-optical modulator serves as a spot heat source. Muscio and Grinzato [2002] showed how to measure the thermal diffusivity of metal and plastic samples with a lock-in method based on the analytical solution of a thermal wave that propagates along a slap with a certain phase-velocity. The thermal wave is generated by alternated heating and cooling with a Peltier element and the slab surface temperatures are measured with an Agema 900 IR camera.

A commercially available Lock-in Thermography system consists of an IR camera, a modulated radiation heat source, a PC card including IR frame grabber and function generator software and software for controlling the camera and the heat source, as well as recording, analyzing and visualizing the IR images [AT, 2002].

2.4 Summary of Temperature Oscillation Research

Temperature oscillation techniques have proven to be helpful tools for the investigation of convective heat transfer for many decades, although not widely used as a standard method. The beauty of using temperature oscillations for heat transfer measurements rests in the fact that periodic oscillations of known frequency, amplitude and phase can be mathematically treated with harmonic analysis and incorporated into the solution of steady-periodic heat conduction problems.

None of the previously developed methods allows obtaining the spatial distribution of local convection coefficients in a single measurement. Only the Prinzen and the Wandelt method allow for measurements from the backside of the heat-transferring wall.

The high power demand to induce temperature oscillations into the fluid limits the achievable amplitude and the scale of the test objects. Also the experimental setup consisting e.g. of heating and cooling devices, fast-switching valves and controlled pumps can become rather complex. The present method of supplying radiant energy from the outside of a heat exchanging surface and the application of an infrared camera can overcome these disadvantages. Thermal energy can be supplied e.g. by a modulated laser or a halogen lamp, much less energy is needed and the experimental setup is simpler. The fluid temperature merely has to be kept constant for a few periods to reach a steady periodic state and take the measurement data. It is possible to evaluate the convection on the front or the backside of a heat-transferring wall. The evaluation of the convection coefficient depends on the mathematical formulation of an appropriate system model and its solution with the input of measured temperature data.

The temperature oscillation IR thermography methods described above illuminated the principle of convection measurements and showed the feasibility and their limitations. For the wall model a harmonic solution rather than a transient solution is sufficient, i.e. only the amplitude and phase angle of the temperature are considered. The previous methods yield average heat transfer coefficients; generally, no local surface distribution $h(x,y)$ can be obtained since they are based on 1-D mathematical wall models. A practical method needs a 3-D conduction-convection wall model to relate the measured phase delay of the temperature response to the local convection coefficients.

Summarizing these conclusions provides the prospect for the present measurement method. An approach including IR thermography data from radiative heating of the outside of a heat exchanging surface together with a three-dimensional harmonic wall conduction model offers outstanding advantages:

- Quick and simultaneous measurement of the local convection coefficient distribution with high resolution
- Lock-In thermography using phase delay information is independent of heat flux, surface emissivity and ambient reflections
- Contact-free, no surface preparation with probes or heaters, no fluid interaction

Such a method will be developed in this study.

3 Numerical Heat Conduction Modeling

3.1 Heat Conduction

Heat diffuses in solid volumes by conduction along the temperature gradient:

$$\vec{q} = -k\nabla T \tag{3.1}$$

This is known as Fourier's Law. To describe the space- and time-dependent temperature field in a body that results in the heat flux vector $\vec{q}$, one needs to obtain the temperature T at any location x,y,z as a function of the time t. Starting from Fourier's Law, integration over the volume and inclusion of a volumetric heat source S yields the common heat diffusion equation:

$$\nabla^2 T + \frac{S}{k} = \frac{1}{a}\frac{\partial T}{\partial t}\,. \tag{3.2}$$

Here the thermal conductivity k and the thermal diffusivity a are usually assumed constant over the considered temperature range. This is a partial differential equation because the temperature T appears in the form of space- and time-derivatives. For many problems, the equation can be reduced and solved, e.g. when the temperature gradient is one-dimensional or the time-derivative vanishes if steady state is reached. Many standard solutions for steady state, periodic and transient conduction problems have been published, mostly in dimensionless form so that the solutions can be applied to groups of similar problems; references include Carslaw and Jaeger [1959], Hausen [1976], Myers [1971], Özisik [1993] and VDI-Wärmeatlas [1997]. However, temperature oscillations in finite volumes are not such simple cases; Wandelt's solution [Wandelt and Roetzel, 1997], discussed in chapter 2 Previous Research, demonstrates the complexity of an analytical solution in a one-dimensional case.

Standard heat conduction problems are concerned with finding the temperature distribution in a solid volume based on the boundary conditions. Inverse heat conduction problems on the other hand are posed in a way that the cause has to be calculated based on the effect, e.g. boundary and initial conditions or properties are unknown, but the temperature distribution or the heat flux in a volume is measured. Standard problems are considered mathematically well-posed, i.e. they always have a solution that is

1. existent
2. unique
3. stable under small changes of input data.

Opposed to standard heat conduction problems, inverse problems often are ill-posed, i.e. any of the criteria above are not satisfied [Özisik, 1993]. The solution of problems of this type may be inherently difficult or impossible due to the high sensitivity to input errors, a large number of parameters to be estimated, or an infinite number of possible solutions of which the "right" one has to be found.

Finding the heat transfer coefficient on a three-dimensional conducting wall subjected to temperature oscillations is an ill-posed problem. The only information is the phase-lag of the surface temperature and the existence of a periodic surface heat flux with known phase and frequency. Generally, an infinite number of possible solutions exist for that problem, since lateral conduction can blur features on the backside that are small compared to the thickness. However, most solutions have no physical meaning and are characterized by steep gradients. One particular solution is the simplest and physically most likely with the smoothest convection coefficient gradients. This solution is sought in the calculation process.

This ill-posed problem can only be solved in one direction, with a given convection coefficient as a boundary parameter that is adapted to the temperature phase delay in an iterative solution process. Such iterations would take very long if transient calculations with many time steps were involved. The system therefore is transformed into the frequency domain in order to perform harmonic rather than transient computations. This is possible since the system is in steady periodic state and can be fully described with frequency, amplitude and phase of the temperature.

3.2 Thermal-Electrical Analogy Model

A model of a thermal system can be translated into a mathematically analogous model based on electrical parameters. When defining the electrical properties analogous to the thermal properties, all numerical values conveniently stay the same in the analysis.

In a thermal-electrical analogy, temperature is equal to electric potential difference. Heat flow finds its equivalent in electrical current, thermal energy can be substituted by electric charge. The material property of thermal conductivity immediately corresponds to the electric conductivity. Steady state calculations in a conducting volume are readily solved for thermal as well as electrical problems.

Table 1: Corresponding thermal and electric parameters

Thermal model	**Electrical analogy model**
Temperature, *T*	Voltage, *U*
Convection coefficient times area, *hA*	Inverse resistance, *1/R*
Conductivity, *k*	Conductivity, Inverse resistivity, *1/r*
Heat flux, *q*	Current density, *s*
Heat capacity, *C*	Electric capacity, *C*
Energy, *Q*	Charge, *Q*

For transient problems, the thermal and electric capacities become important. Electric capacity is a function of the geometric configuration of the electrodes and the dielectric properties of the insulation material. While electric and thermal conduction can be modeled equally in a volume, electric capacity, however, cannot be modeled homogenously distributed over the volume and has to be discretized.

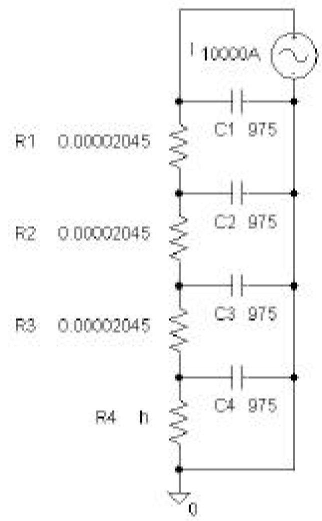

Figure 3.1: 1-D thermal-electrical analogy model of a wall with four nodes loaded with an oscillating heat flux (created with Pspice®). Units (for 1 m^2): I = [A], R = [W], C = [F].

3.2.1 Discretization and FDM

In the theory of the Finite Difference Method, a homogenous body like a line, an area or a volume, can be modeled as a mesh of interconnected nodes. Thus, following the thermal-electric analogy, a thermal conducting domain including thermal capacity is discretized into a grid of nodes connected with resistors and capacitors, just as in an electric circuit. The parameters of the resistors depend on the direction, distance and cross section of the elements surrounding the node; the capacity of each node depends on the element’s volume, the capacitor is electrically grounded. The discretization bares the analogy’s great advantage: the heat transfer problem can be solved employing well-established techniques of electric network analysis. The electric current balance for each node with the application of Ohm's law for the voltage and the resistance to the neighboring nodes leads to a system with one equation per node. For steady periodic conditions, an AC analysis can be made using complex numbers. At each node, the voltage, amplitude and phase can be evaluated from u. Boundary conditions such as adiabatic (no current), constant temperature, heat flux or convection (voltage and resistance) can be coupled onto the boundary nodes instead of the respective neighboring node resistor connection. The current balance equation for an inner volume node with the coordinates x, y, z, becomes

$$\frac{u_{x+1,y,z}+u_{x,y+1,z}+u_{x-1,y,z}+u_{x,y-1,z}-4u_{x,y,z}}{R_{xy}}-\frac{u_{x,y,z+1}+u_{x,y,z-1}-2u_{x,y,z}}{R_z}-u_{x,y,z}\, i\, w\, C = 0 \qquad (3.3)$$

with the resistance in the x- and y-direction R_{xy}, (3.4), and z-direction R_z, (3.5), the capacity of the element C, (3.6), the frequency w and the imaginary unit i.

$$R_{xy} = \frac{d_{xy}}{k}\frac{z_{max}}{d_{xy} d} \qquad (3.4)$$

$$R_z = \frac{1}{kd_{xy}^2}\frac{d}{z_{max}-1} \tag{3.5}$$

$$C = \frac{r\,cd_{xy}^2 d}{z_{max}} \tag{3.6}$$

In these equations appears the wall thickness d, the grid spacing in x- and y-direction d_{xy}, the number of nodes in thickness z-direction z_{max} and the density r along with the specific heat capacity c. The boundary conditions adiabatic (no current), constant heat flux and convection (voltage zero and resistance $1/h$) are applied to the boundary nodes. For the heat-transferring wall with oscillating heat flux, the upper surface nodes receive a heat flux with the amplitude $q_0(x,y)$ and the natural convection h_0, the bottom surface is stressed with the convection coefficients $h(x,y)$ that are to be found.

Eventually, the equation (3.3) for every node (x,y,z) can be combined into a matrix K of complex conductivities, a vector u of the nodes voltages and a heat flux amplitude vector q:

$$\begin{pmatrix} k_{1,1} & \cdots & k_{1,xyz} \\ \vdots & \ddots & \vdots \\ k_{xyz,1} & \cdots & k_{xyz,xyz} \end{pmatrix} \begin{pmatrix} u_1 \\ \vdots \\ u_{xyz} \end{pmatrix} = \begin{pmatrix} q_1 \\ \vdots \\ q_{xyz} \end{pmatrix} \tag{3.7}$$

This is a square sparse matrix with a size of the number of nodes of $m = x\ y\ z$. The symmetric structure of the matrix shows seven diagonal bands of non-zero elements. This system of linear equations now has to be solved for the complex nodal temperatures $u_{x,y,z}$:

$$u = K^{-1}q \tag{3.8}$$

Such systems of linear equations in matrix form can be solved with a variety of methods, subdivided in direct and iterative methods. Direct methods approach the solution in an algebraic way, the most common and simplest of the direct methods being the Gauss algorithm. For large sparse matrices, direct methods are not suited because computation time and memory requirements are prohibitive. Large sparse matrices can be solved favorably in a numerical, iterative way. Here the computational effort is proportional to the number of variables unlike for direct methods where it increases exponentially and the storage space requirements in the RAM memory are limited to the non-zero elements of the matrix. Although such methods do not yield “exact” solutions, the errors after a sufficient number of iterations are lower than the discretization errors and the inevitable inaccuracies of the input data.

The system of equations is solved in Matlab® with a method specialized for a square symmetric coefficient matrix. This method, called “Minres”, was developed by Paige and Saunders [1975] and implemented in Matlab in a formulation modified by Barrett et al. [1996]. Minres attempts to find a minimum norm residual solution based on Lanczos vectors and orthogonal factorization. The Minres method turned out to be very fast and accurate in comparison to alternative methods. It solves the system with a maximum of 50 internal iterations and, to tremendously increase speed, starts with applying an estimated solution vector that is taken from a previous step.

Since the mathematical problem of obtaining the boundary parameter h from the phase angle f = atan(u) is an ill-posed inverse problem, i.e. the phase angle can only be evaluated in reverse for a given $h(x,y)$, the final solution is obtained by repeatedly solving equation (3.8) in an iterative process. The iteration starts with an estimated set of convection coefficients $h(x,y)$ and solves equation (3.8), then compares the calculated $f(x,y)$ to the measured phase angle $f_{exp}(x,y)$. Then the current set $h_{old}(x,y)$ is modified to a new set $h_{new}(x,y)$ according to the iteration rule (3.9). Next, the coefficient matrix is updated with h_{new} and equation (3.8) is solved again to minimize the error between $f(x,y)$ and $f_{exp}(x,y)$; this loop is repeated multiple times.

$$h_{new} = h_{old} \left(f / f_{exp} \right)^n \tag{3.9}$$

To speed up convergence while stabilizing the solution and increasing accuracy, the ratio f/f_{exp} is raised with an exponent n that decreases with the number of iterations from 1.5 to 0.5. The final solution is obtained after ca. 10 to max. 50 iterations when the RMS phase error stagnates. However, the solution is satisfactory only for “perfect” input data, otherwise many spikes and random variations occur in $h(x,y)$; real experimental data is rarely good enough. To reduce these outliers and extreme gradients without physical meaning that are caused by the ill-posed nature of the problem together with measurement noise, a smoothing algorithm is employed to the matrix h at in the solution process at every iteration step. This smoothing algorithm averages every $h(x,y)$ with the eight neighboring values weighted each by a factor of 0.125. A further improvement is achieved by a similar smoothing of the matrix of the phase error with a weighting factor of one before computing (3.9). The smoothing is a compromise that allows minimizing the RMS of the phase error while producing a physically meaningful distribution of h. The Matlab® script code for the calculation of the heat transfer coefficients with the 3-D FDM wall model can be found in the Appendix.

For demonstration and comparison purposes, a one-dimensional, four-node electric model of a heat-transferring wall was created as shown in Figure 3.1. The parameters are set for a 1 m^2 plate of 1 mm ANSI 304 / DIN 1.4301 stainless steel. The surface of the wall is subjected to a sinusoidal oscillating heat flux modeled as an AC current on the top node with a density of 10000 A/m^2. The phase delay of the temperature response of the top surface node is compared in Figure 3.2 to the analytical solution equation (2.8) discussed in chapter 2 [Wandelt 1997].

3.2.2 Discretization Error

The phase error shown in Figure 3.2 between the analytical and the 4-node FDM solution has a range from 0.4% to 1.4% for a modulation frequency of 0.1 Hz and a 1 mm wall of stainless steel. Increasing the number of nodes reduces the error considerably. However, the number of nodes will always be a compromise between the desired accuracy and spatial resolution and the allowable computation efforts. Higher thermal conductivity, lower frequencies and a thinner wall also reduce the error. Calculations with an FDM model with a number of four nodes in z-direction turned out to give significantly better results than three nodes, whereas the very modest improvement in accuracy when using five nodes, given realistic experimental and material parameters, did not justify the increase in computing time.

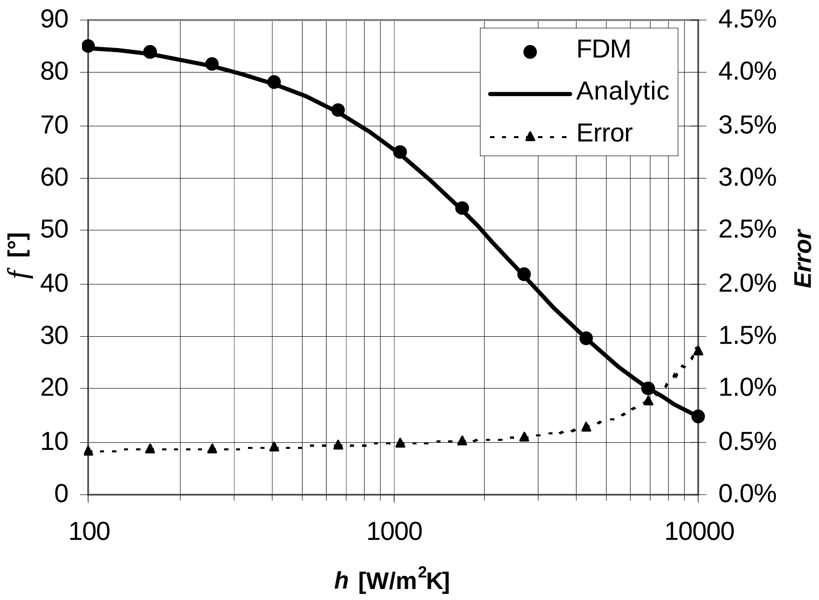

Figure 3.2: Comparison of the 1-D FDM and the analytic solution for the phase delay over the convection coefficient *h* for a 1 mm wall of steel (1.4301) with a frequency of 0.1 Hz.

Although small, the FDM discretization error might cause larger errors in the convection coefficient h due to non-linearity. Knowledge of this error allows calculating a correction factor that can be applied to the experimental phase delay to match the FDM phase lag corresponding to the expected h. The numerical error turned out to be strongly correlated to the wall thickness d, the thermal conductivity k, the oscillation frequency $1/p$ and the convection coefficient h. An estimation of the functional relation of these parameters to the error yielded a quadratic influence of d, a linear relation to $1/p$ and an exponential increase with h that is higher at longer oscillation periods p and smaller at high k. An empirical formula that fits numerical phase delay error data for four nodes is given in equation (3.10):

$$\frac{f_{FDM} - f_{exp}}{f_{exp}} = 765000 \frac{d^2}{k\ p} \exp\left(\frac{\sqrt{p}}{2700} \frac{h}{k} \right) \qquad (3.10)$$

This equation was found by comparison of a large number of 1-D FDM calculations with the analytical solution for a range of parameters as expected under real measurement conditions. It fits the numerical error for a stainless steel wall with an RMS deviation of 36% and allows a reduction of a numerical error that averages 1.2% (1.9% RMS) to an average of 0.1% (0.5% RMS). For a copper wall, the already negligible error can be reduced from 0.03% (0.04% RMS) to 0.006% (0.015% RMS). Thus, the discretization error is compensated in the FDM computation process by modification of the measured input data f_{exp} to f_{FDM} according to (3.10).

A Matlab® script for the calculation of the heat transfer coefficients by numerical modeling can be found in the Appendix.

4 Measurement Data Processing

Measurements with the TOIRT require a substantial amount of data processing to deduce a map of the surface temperature phase delays from the time series of surface temperature matrices recorded with the IR camera. The phase delay data will be the input for the actual calculation of the heat transfer coefficients with a numerical wall model in the subsequent step.

4.1 Phase Delay Computation

The phase delay between the heat flux modulation and the surface temperature oscillation is the input for calculation of the convection coefficients with the numerical model. This phase delay is derived from the temperatures measured with the IR camera for every pixel and is the only required experimental data for the TOIRT method. A Fourier analysis is applied to the time series of temperature data for the computation of the phase delay. The raw temperature data is generally preconditioned with drift compensation (see paragraph 4.2). The accuracy of the phase delay data is critical for the calculated convection coefficients and is discussed in the sensitivity analysis in chapter 6 Sensitivity Analysis.

4.1.1 Single-Frequency Discrete Fourier Transform

The single-frequency discrete Fourier Transform (SFDFT) is a mathematical procedure to obtain the amplitude and the phase angle of any series of discrete values compared to a sine function. First, the Fourier coefficients a and b are calculated according to Equations (4.1) and (4.2). The discrete values are the measured temperatures $T(x, y)$ of every pixel over the frames i. Equations (4.1) and (4.2) are computed in a double loop over the column and row coordinates x and y of the temperature array:

$$a = \frac{2}{n}\sum_{1}^{n} T_i \cos(wt_i) \tag{4.1}$$

$$b = \frac{2}{n}\sum_{1}^{n} T_i \sin(wt_i) \tag{4.2}$$

with n the number of frames in the array, w the angular frequency and t the time of each frame. Then the amplitude A and the phase f of the fundamental sinus function is derived from the Fourier coefficients:

$$A = \sqrt{a^2 + b^2} \tag{4.3}$$

$$f = \arctan\frac{a}{b} \tag{4.4}$$

The number of frames considered in the analysis must comprise one or more full oscillation periods; the more periods are integrated the better the accuracy and the less noisy the data will be. Although the computational effort for these operations is considerable, a complete analysis over e.g. 900 frames with 272 x 68 pixels may only take a few seconds on a state of the art PC. The phase delay is the shift relative to a sine curve with same time *t*. For scanner type IR cameras, the time *t* is adjusted for the difference between the base time of the frame and the actual time of each pixel in the frame, as the pixels are scanned row-wise subsequently. For the Agema Thermovision THV 900 IR camera, that scans 30 frames per second with 272 columns and 68 rows, the time per pixel is 1.8022 µs. Such the time *t(x,y)* is defined as zero for the first pixel in the first frame and 1/30 s for the first pixel in the second frame and so forth for all frames.

4.1.2 Frame-Time Synchronization

During a the TOIRT measurement, the heat flux must be synchronized to the IR camera frame recording to later compute the phase lag between the temperature and the heat flux. The Fourier analysis delivers this phase delay *f* of the fundamental sine function of the temperature relative to the time of the first frame. The time *t* of the frames relates to the time dependent function of the heat flux modulation, e.g: $q = q_0(1+\sin(wt))$. Thus, the first frame must be recorded at time zero of the heat flux modulation, i.e. the exact timing of the heat flux must be known, otherwise the computed phase delay has to be corrected for the additional time shift *Dt* between the heat flux and the frame recording. The synchronization between the heat flux and the temperature frame recording is critical for the accuracy of the measurement and must be very precise. However, experiments showed that this was not always the case with the IRFlashLink frequency generator and frame grabber and the AT IRLockIn Software [AT 2002]: differences of up to +/- 2 frames occurred, leading to substantial measurement uncertainty. Also any additional time delay within the heat source and it's power electronics must be taken into account for the synchronization. The laser power supply time delay between the trigger signal from the frequency generator and the actual power output was 10 ms, measured with a digital oscilloscope. The high uncertainty and the hardware dependency make this frame-time synchronization method rather difficult to cope with.

4.1.3 Square Wave Phase Synchronization

Above problems with the frame-time synchronization could be solved if information of the exact phase of the heat flux function could be obtained directly from the recorded temperature frames rather than from the assumed recording time. Moreover, no synchronization between the heat flux control and the frame recording would be necessary. This hardware-independent method would make the phase measurements more precise and allow for a simpler measurement setup with a broader choice of equipment for IR image frame grabbing and heat flux modulation.

To trace of the timing of the heat flux modulation in the temperature data, a step change resulting in an immediate discontinuity of the temperature response must occur. Square wave modulation is applicable. The authors of previous temperature oscillation research using phase delay data including Prinzen [1991], Wandelt and Roetzel [1997] and Turnbull [2002] agree, that the phase delay of the temperature response is independent of the waveform, i.e. an equal phase lag will be observed whether the heat flux modulation is a sine or a square wave.

In addition, own experiments carried out on semi-infinite specimen show that there is no difference whatsoever in the temperature phase delay to a sine wave or a square wave modulated heat flux.

The SFDFT given in equations (4.1) and (4.2) extracts the fundamental sine function of any periodic series of values, including square waves; the measured temperatures and the Fourier transformed of these values for a semi-infinite specimen are shown in Figure 4.1:

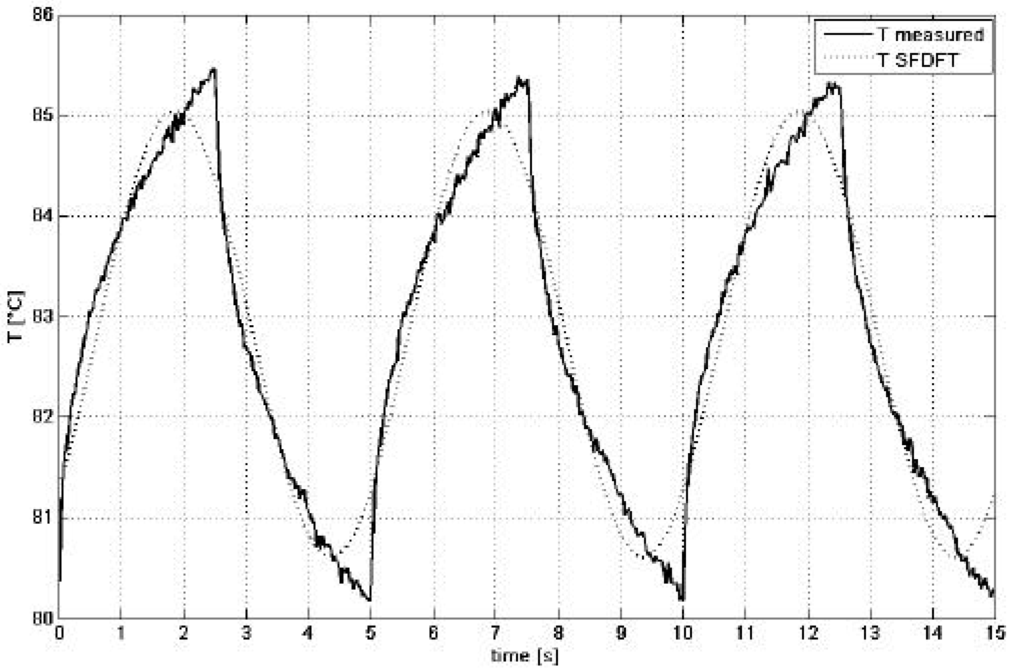

Figure 4.1:Measured temperature response of a semi-infinite body and the Fourier transformed of these temperature (SFDFT).

In Figure 4.1 the periodic exponential temperature increase and decrease with the extrema at the discontinuities can be seen. The maximum occurs right at the time when the square wave heat flux is switched from the maximum to the minimum level; the minimum is found where the heat flux is switched from the minimum to the maximum level. By finding the minimum or the maximum in the data, the timing respectively the phase of the heat flux waves relative to the frames can be obtained. The extrema are not clearly defined in a time series of a single pixel due to noise. However, the area-averaged temperatures show the extrema more distinctly. Finding the extrema in the data is achieved in two steps, first the minimum respectively the maximum of the time derivative is located and then the maximum respectively the minimum of the temperature in the direct vicinity before the largest step is found. This procedure prevents from mistaking a local extremum due to data fluctuations for the timing base. Extrema that lie on the beginning or end of the data series are left out.

Since the temperature data is represented in time-discrete frames rather than in a continuous function, the actual extrema will lie at a time somewhere between two frames. To find these values, two polynomial fit functions of first and second degree, respectively, are derived from the data that lie on the increasing respectively the decreasing branch before and after the extrema. The intersection point of these curves is the actual extrema and is calculated analytically. In Figure 4.2, the area-averaged temperature and the two curve fits with the extremum are illustrated. For some data sets with lower temperature gradients, recorded e.g. for a measurement on semi-infinite body with a halogen lights heat source, the curve fitting to find the extrema works better with a sum of two exponential functions which approximates the real curve closely instead of the polynomial approach. When the shape of the mean temperature approaches a sawtooth profile, as found for low heat transfer coefficients e.g. in a wind tunnel, the extrema are found best between two first degree polynomial fits over 5 to 10 data points before and after the extremum.

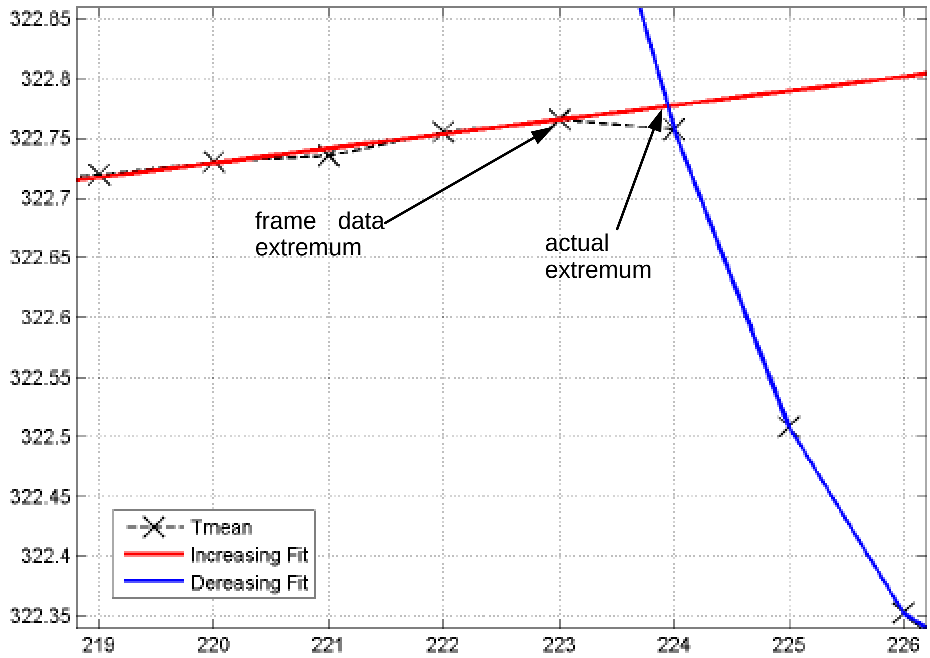

Figure 4.2: Area-averaged temperature and curve fits of the last six values before and the first three values after the extremum.

When the timing of the heat flux modulation of the extrema relative to the frames is known, the phase angle of the modulation can be calculated with the oscillation period length. For 50% duty cycle square waves, the maximum follows the minimum with a phase delay of π. Both extrema in each period are used for the phase evaluation; the final phase is taken as the weighted mean of all values. To minimize the influence of outliers while using as much information from the data as possible, a special algorithm is applied for deriving this mean. This algorithm delivers a weighted mean where the weight of each value is the inverse of the squared deviation from the arithmetic mean.

4.1.4 Comparison of the Synchronization Methods

A comparison of the phase delay obtained using the two different synchronization methods for 12 measurements on a semi-infinite specimen is shown in Figure 4.3. The actual phase delay is $f = -0.785$, see chapter 5 Validation. The uncorrected time/frame method delivers very unreliable results with high deviation. The "corrected" method refers to a manually corrected synchronization by adding or subtracting a few frames to account for the apparent time difference between the start of the frame recording and the heat flux modulation. The correction gives much better results, but requires a prior guess value of the result to estimate how many frames are offset relative to the heat flux modulation. This number can be found by the time deviation of a single measurement from the mean of a larger sample. The square wave phase synchronization yields results that are at least as good as the corrected time/frame method, but without the somewhat arbitrary data manipulation. This synchronization method is henceforth primarily used in the experiments.

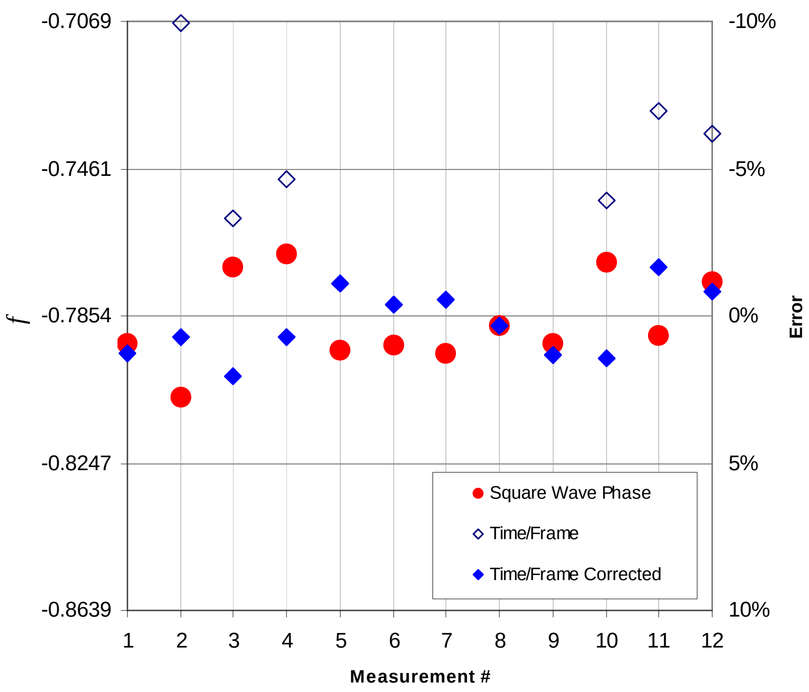

Figure 4.3: Comparison of the phase delay for 12 measurements on a semi-infinite body calculated with the square wave phase synchronization and the time/frame synchronization method.

4.2 Drift Compensation

Drift of the surface temperature during a measurement is a stepless change of the mean temperature caused by the transient effects at the start of the heat flux oscillation when the surface heats up under a positive the heat flux. The drift occurs before steady-periodic state has reached and has usually the shape of an exponential decay function. In principle, drift has to be avoided since it contradicts the measurement method's precondition of steady-periodic state and affects the measurement results. However, reaching steady-periodic state may take very long for measurements where mean surface temperatures are high compared to the environment. For longer measurements, also small changes of the environmental conditions or the heating of the fluid can lead to temperature drift. Generally, temperature drift during measurements can be minimized but never fully avoided.

The temperature drift affects the phase delay calculated by Fourier transform as follows: positive drift, or heating, leads to a larger phase delay than actual; negative drift has the inverse effect. Therefore, measurement data containing significant temperature drift cannot be evaluated readily and have to be mathematically processed to compensate the drift. After successful compensation, the data can be treated with the standard procedure and will give the same results as data attained without a drift.

As an example for temperature drift, Figure 4.4 shows measured raw temperature data of one pixel on the surface of a semi-infinite body (see also chapter Validation) for 900 frames. The data comprises six oscillation periods with a frequency of 1/5 Hz from time zero to 30 s. The drift amounts to 8.6 K.

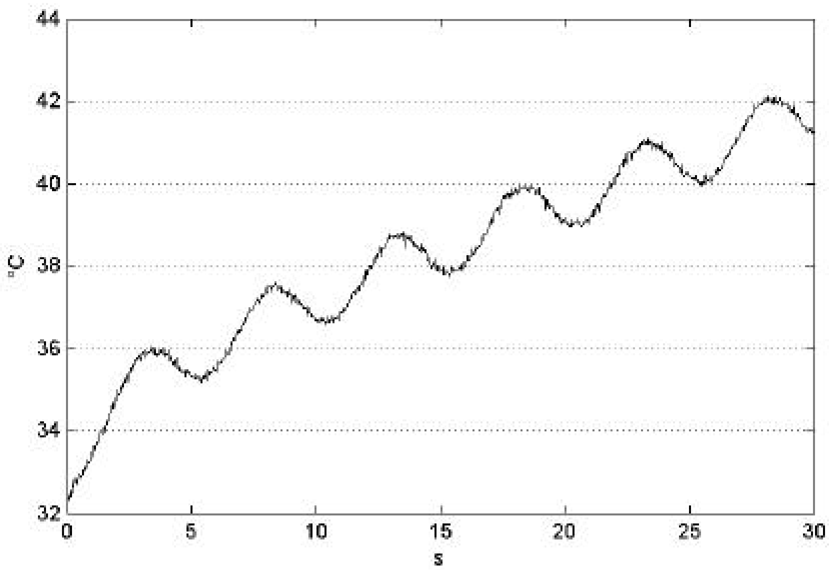

Figure 4.4: Original temperature data recorded in 900 frames at 30 fps for one central surface pixel.

Using these data for computation of the phase delay without drift compensation leads to a phase angle of $f = -1.04$. The correct value that has been expected and verified in this experiment is $f = -0.785$. The resulting error equals 32%.

The algorithm created to compensate the temperature drift in a data set works as follows:

1. The mean temperature of each pixel in each period is calculated. The mean of these mean temperatures gives the total mean temperature of the data set.
2. For each period, a linear function is derived from the difference of the mean temperatures of the two neighboring periods that yields the deviation from a zero-mean data set for each frame.
3. For each frame in each period, the mean of this period is added to the function and the total mean is subtracted
4. The 1st to the 3rd step is continued in a loop over every pixel and forms an array corresponding to the original data set

5. This array of compensation function’s values is subtracted from the array of original data

After application of the period-wise linear compensation algorithm to the measured data, the temperature drift is considerably reduced.

Figure 4.5 shows the compensated temperature over time for the same pixel as before.

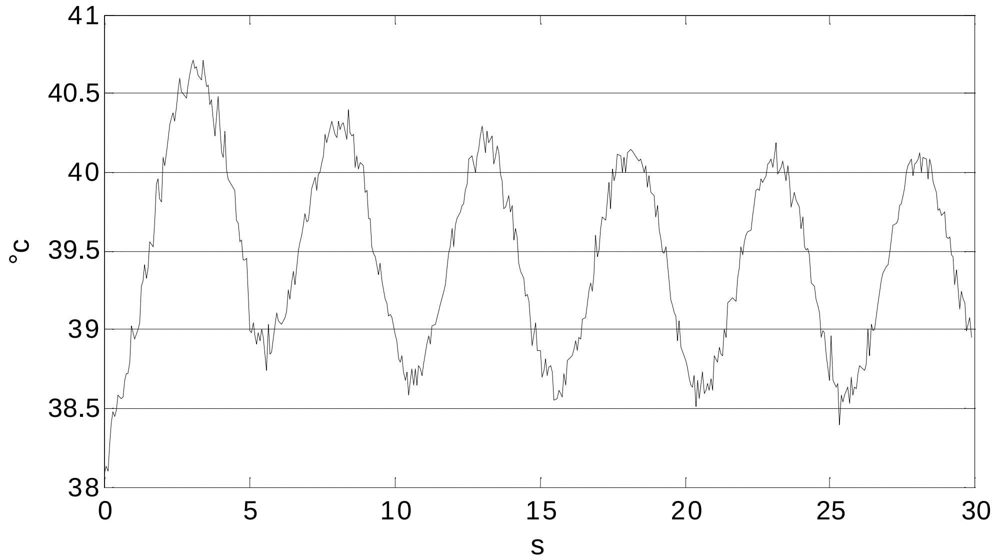

Figure 4.5: Measured temperature after the first drift compensation.

The temperature now oscillates sinusoidal around a mean value of approximately 39.5°C. Instead of the increase, now a slight negative trend appears. It can be concluded that, although a significant drift reduction is reached, the data can still be improved. Nothing besides increased computing time should stop us from applying the same algorithm again to the modified data set until the result is satisfying:

Figure 4.6 is a plot of the pixel’s temperature after applying the drift compensation 4 times iteratively; the data shows no trend anymore and oscillates around the mean value of 39.4°C. Only the first period still shows relicts of the transient effects. For this reason, the first couple of periods are normally not considered for data evaluation. The drift compensation does not affect any un-periodic or random effects such as measurement fluctuations (noise).

The computation of the phase delay after applying the drift compensation yields $f = -0.789$. With a real value of $f = -0.785$, the error now is 0.5%. Thus, the application of drift compensation facilitated the usage of a substantially drifting set of temperature data and reduced the error from unacceptable 32% down to 0.5%.

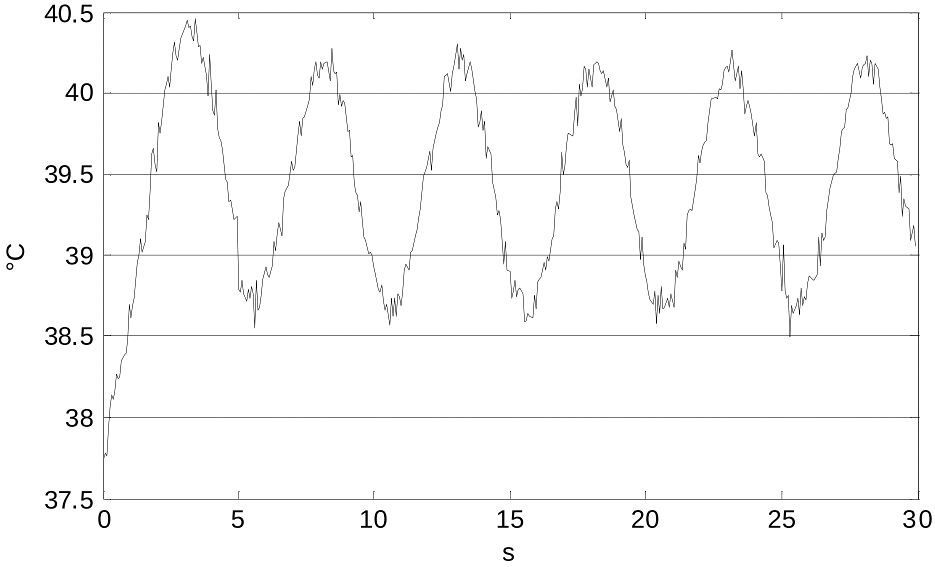

Figure 4.6: Measured temperature after iterative drift compensation.

4.3 Resolution, Averaging and Aliasing

Since infinitively fine spatial resolution is not attainable, the measured temperature at one pixel is the average temperature of a certain area, which determines the spatial resolution of the measurement. Obviously, the spatial resolution must be fine enough relative to the size of the expected prominent features to conserve them throughout the calculation process. Efforts of noise reduction by local averaging over multiple pixels of temperatures or phase-delays may further decrease the resolution. Whether measured with low resolution by the camera or downgraded later by arithmetical averaging of neighboring pixels, the phase-lag supplied to the numerical modeling may not lead to the correct local heat transfer coefficients if the averaged area comprises large gradients. Due to the non-linear relation between the measured phase-lag and the convection coefficients, an “average” local heat transfer coefficient can be significantly lower when the number is calculated based on spatially averaged phase delays instead of being the average of multiple values computed with higher resolution. Similar, aliasing effects can occur either when considering periodically structured convection coefficients during the actual measurement, at the data processing steps when averaging takes place or specifically during numerical modeling, when the spatial resolution is inadequate. Thus, to properly resolve local features and even to estimate area-averaged convection coefficients correctly, the averaging of high gradients of the temperature phase-lag has to be avoided; with a fixed IR camera resolution and limited computing resources, only partial areas may be studied when the heat transfer coefficients vary widely.

An example for the occurrence of aliasing effects are plate heat exchangers with their periodic pattern of strongly varying convection coefficients. Here the spatial resolution must be chosen carefully to avoid above problems and gain reasonable results, details and accuracy come at the expense of the size of the evaluated area.

A Matlab® script including all steps of the data processing described above can be found in the appendix of this thesis.

5 Validation

The new TOIRT technique is validated for each substep of the measurement process to ensure reliable and accurate results for the local heat transfer coefficients.

5.1 Experimental Validation

The validation process verifies the measurement technique and the experimental set-up by reproduction of a priori known results. This was done by measuring the temperature response of a semi-infinite specimen. The temperature response of a semi-infinite body to a periodic heat flux is constant and nearly independent of the frequency and heat transfer. These characteristics make the semi-infinite body an ideal object for validation.

5.1.1 Temperature Oscillations in a Semi-infinite Body

An analytical solution of the periodic temperature field and the heat flux in a semi-infinite body is developed in the following. The solution leads to the desired surface temperature phase delay. The starting point is one-dimensional conduction through a slab:

$$\frac{\partial^2 T}{\partial z^2} = \frac{1}{a}\frac{\partial T}{\partial t} \tag{5.1}$$

With a solution approach for the periodic temperature that is dependent on the time t and the depth z,

$$T = A(z)e^{iwt} \ , \tag{5.2}$$

equation (5.1) yields the complex homogeneous differential equation (5.3):

$$\frac{\partial^2 A}{\partial z^2} = \frac{iw}{a} A \tag{5.3}$$

This equation can be solved with an exponential approach for *z*®¥ : *A(z)*®*0*, and the amplitude $T_0 = A(z=0)$, Equation (5.4):

$$A = T_0 e^{-z(1+i)\sqrt{\frac{w}{2a}}} \tag{5.4}$$

Substituting Equation (5.4) into the solution approach (5.2) and further modification leads to the temperature distribution of a thermal wave in a 1-D semi-infinite body, Equation (5.5):

$$T = T_0 e^{-z\sqrt{\frac{w}{2a}}} \cos(wt - z\sqrt{\tfrac{w}{2a}}) \ . \tag{5.5}$$

Given the function $T(z,t)$ for the temperature, the surface heat flux q_0 at $z=0$ can be calculated as the derivative of T times thermal conductivity k:

$$q_0 = -k\frac{\partial T}{\partial z}\bigg|_{z=0} = kT_0\sqrt{\tfrac{w}{a}}\,e^{-z\sqrt{\frac{w}{2a}}}\cos(wt - z\sqrt{\tfrac{w}{2a}} + \tfrac{p}{4})\bigg|_{z=0} \tag{5.6}$$

Above equation reduces to

$$q_0 = kT_0\sqrt{\frac{w}{a}}\cos(wt + \frac{p}{4})\,. \tag{5.7}$$

Equation (5.7) shows that the phase-lag of the surface temperature responding to the heat flux q_0 is $p/4$.

The damping of the amplitude and the phase-lag in the material with increasing z can be found to be a function of the frequency divided by the thermal diffusivity. The length of the thermal wave is

$$l = 2p\sqrt{\frac{2a}{w}}\,. \tag{5.8}$$

At a distance $z = l$ from the surface, the amplitude has decayed to 0.187 % of T_0. Since the thermal wave is very attenuated, the question rises how deep into a real wall material the thermal wave is citing any effects that can be observed on the surface or, formulated differently, how thick a wall must be at least to become semi-infinite.

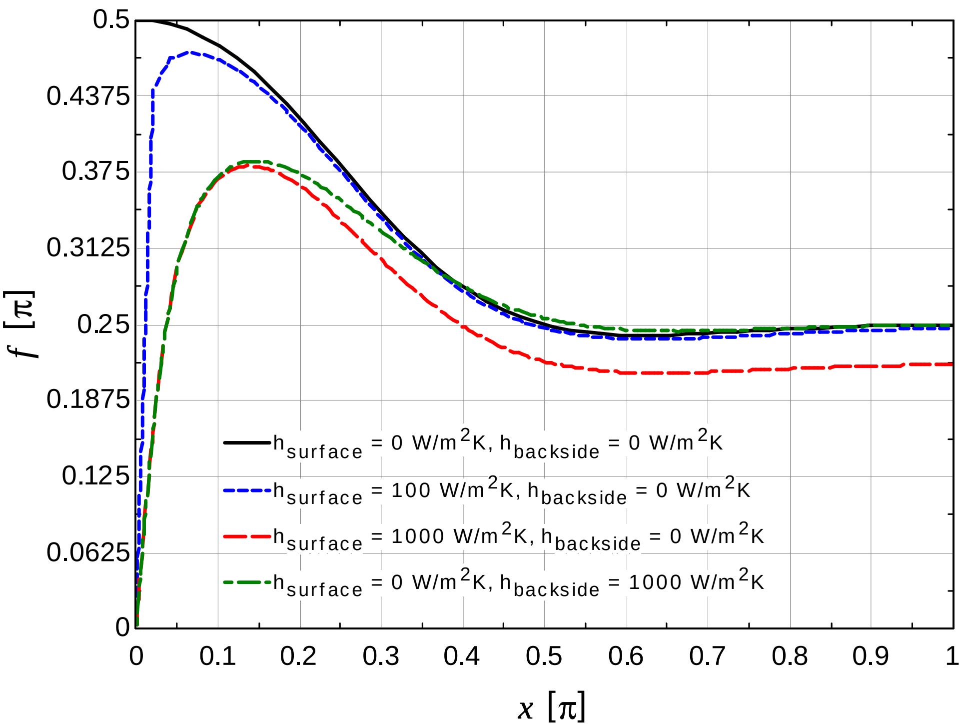

Figure 5.1: Phase delay as a function of the wall thickness x**. and convection** ***h*****.**

Figure 5.1 shows the phase delay of a temperature oscillation over the dimensionless thickness x for 1-D conduction through a slab of stainless steel at a frequency of 0.1 Hz according to Equation (1.15). The wall starts to behave semi-infinite for $x > \pi/2$, equal to a thickness of λ/4, where the phase lag without the influence of convection on either side reaches π/4. For bodies thicker than λ/4, the phase-lag briefly becomes smaller than π/4, before asymptotically approaching the final value of f = π/4 again. For thinner bodies, $x < \pi/2$, the phase-lag is clearly dependent on the heat transfer conditions on both sides. Figure 5.1 shows that indeed the backside convection coefficient has negligible influence on the phase-lag once the thickness passes the semi-infinity threshold, as the upper three lines merge according to the conclusion from Equation (5.7). The surface convection, however, may lower the phase-delay below the value expected for the semi-infinite body when the heat transfer coefficient is high enough; in the case of Figure 5.1, the surface heat transfer coefficient has to be larger than 100 W/m^2K to have a significant effect. For very thin walls, the phase delay becomes the same whether a certain heat transfer coefficient is applied to the surface or the backside, as shown in Figure 5.1 in the lower two lines with surface or backside convection, respectively, for $x < \pi/10$.

Thus, as long as surface heat transfer is low, the phase-lag of the temperature response will be constant and independent of the heat transfer f = π/4 for all bodies thicker than $l/4$. The thermal wave, attenuated to 21% at that point, will not feed back to the surface from the backside. The penetration depth d of the thermal wave is defined here as one quarter of the thermal wavelength, or π/2 = 1.5708 times the root term:

$$d = \frac{l}{4} = \frac{p}{2}\sqrt{\frac{2a}{w}} \tag{5.9}$$

This result is similar to Meola [2002], where a penetration depth of 1.8 times the root term is suggested for observing material flaws, and the IRLockIn Manual [AT, 2002], where just the root term is given as the penetration depth for thermal imaging. Carslaw and Jaeger [1959], who derived the equations for the semi-infinite body in an analogous way, consider a body to appear semi-infinite when the thickness is greater than λ. Knowledge of the penetration depth is of high practical importance when undertaking measurements to choose the appropriate frequency depending on the material properties (see also chapter 6 Sensitivity Analysis).

The conclusion from the discussion above is that the semi-infinite body with 1-D periodic conduction is well suited for calibration due to a constant phase-lag of f = π/4. A limitation is a sufficiently low surface heat transfer coefficient on the order of 10 W/m^2K; a typical value for the convection coefficient on a surface under calm air is 3 W/m^2K.

5.1.2 Validation Measurements

The experimental set-up for the validation of the measurement method with a semi-infinite body includes the following components:

- A fiber-coupled laser diode array with a wavelength of 685 nm providing 15 W optical power used as a heat source with a Lambda 50A programmable power supply.
- An Agema 900 LWB IR scanner that records the surface temperatures in the long wave IR band of 9-11 µm with a spatial resolution of 272 x 68 pixels and 30 frames/s.
- IRLockIn [AT, 2002] Software and IR frame grabber and function generator heat source control PCI-card.

The experiments were conducted on various specimens. Initial tests on cylinders made of aluminum showed an uneven phase lag distribution over the surface that on average is smaller than expected for a semi-infinite body. This is attributed to three-dimensional conduction induced by the inhomogeneous radiation field of the laser and radial heat losses. The laser radiation exiting the fiber has a Gaussian intensity distribution and a strong divergence, the distance between the fiber's end and the surface determines the diameter of the heated region and the lateral heat flux gradients, which have to be low to reduce lateral conduction. Samples made of stainless steel give much better results and can be shorter, thus leading to a faster decay of transient effects. However, stainless steel still also exhibits the aforementioned effect similar to aluminum. To eliminate the influence of 3-D conduction, a homogeneous material of relatively low conductivity that suppresses lateral conduction should work best. Ordinary glass turned out to be well suited. In fact, the specimen was a beer bottle. The low thermal conductivity of 0.8 W/mK together with a heat capacity of 0.84 kJ/kg and a density of 2550 kg/m^2 allows for a wall thickness of only 3 mm to behave semi-infinite for frequencies down to 0.1 Hz, the wall thickness is ca. 4 mm.

The phase images of this semi-infinite body show a quite uniform value over the evaluated area of 272 x 68 pixels. For 30 measurements with frequencies of 0.2 Hz and 0.1 Hz, the average relative phase error compared to $-\pi/4$ is -0.6% (1.4% RMS) with a standard deviation of 1.3%. The standard deviation of the phase-lag of single pixels in the evaluated area is ca. 2%. The error is not significantly affected by the measurement frequency; similar results are obtained for other frequencies between ½ Hz and $^1/_{20}$ Hz. Since the experimental results show sufficiently close agreement to the analytically calculated number, the measurement setup delivering the phase delay of the temperature oscillation is considered valid.

Figure 5.2: Per aspera ad Astra: validation of the experimental set-up with a semi-infinite body made of glass. Arrangement of the IR camera (right) and the fiber-coupled laser (next to the camera lens).

5.1.3 Heat Source Time Delay

Any radiation heat source other than a semiconductor laser, which responds instantaneously and linearly to the input power, exhibits a time delay between the modulated electric input and the radiative output power. This time delay is due to the thermal capacity of the heat source. It adds an additional phase delay to the surface temperature since the change-rate of the heat flux is lower, the temperature response is slower compared to a perfect sine or square wave modulation assumed in the SFDFT and synchronization. To extract the true phase delay of the surface temperature to the radiative heat flux, this additional phase delay must be known and compensated for. The heat source time delay is converted into a phase delay and subtracted from the temperature phase delay delivered by the SFDFT. The time delay is dependent on the modulation frequency and amplitude and has to be evaluated experimentally. This can be achieved by comparison with a sample that has an a-priori known phase delay, such as a semi-infinite body. From the time delay, the characteristic time constant of the heat source could be derived.

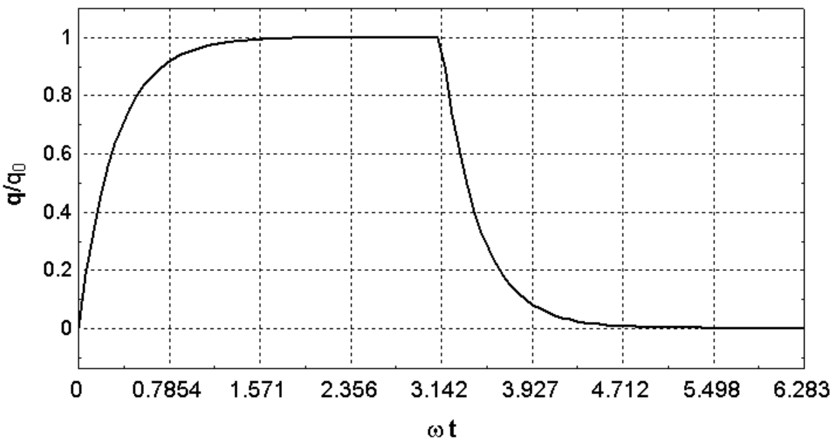

Figure 5.3: Square wave modulated heat flux with a time constant t of 0.05 period lengths.

A simple analytical approach of a square-wave heat flux with a time constant t is shown in Figure 5.3 and given in Equation (5.10):

$$\frac{q(t)}{q_0} = 1 - e^{-\frac{t}{t}} \quad \text{for } 0 \le t < \frac{p}{2}\,, \qquad \frac{q(t)}{q_0} = e^{-\frac{t-\frac{p}{2}}{t}} \quad \text{for } \frac{p}{2} \le t < p \tag{5.10}$$

An ideal radiation heat source such as a laser with proper square-wave modulation has a time constant of zero, whereas the radiative power of halogen lamps lags the input electrical power similar to Figure 5.3. The phase delay of the oscillation due to the time constant compared to a perfect square wave can be calculated by a Fourier analysis. The Fourier coefficients are obtained by integration of the heat flux (5.10) in Equations (5.11) and (5.12):

$$a = \frac{2}{p}\left[\int_0^{\frac{p}{2}} \left(1 - e^{-\frac{t}{t}}\right) \cos\frac{2p}{p} t \; dt \; + \int_{\frac{p}{2}}^{p} -e^{-\frac{t}{t}} \cos\frac{2p}{p} t \; dt\right] \tag{5.11}$$

$$b = \frac{2}{p}\left[\int_0^{\frac{p}{2}} \left(1 - e^{-\frac{t}{t}}\right) \sin\frac{2p}{p} t \; dt \; + \int_{\frac{p}{2}}^{p} -e^{-\frac{t}{t}} \sin\frac{2p}{p} t \; dt\right] \tag{5.12}$$

These integrals deliver

$$a = -\frac{4}{pt}\left(\frac{e^{-\frac{p}{2t}} + 1}{\frac{1}{t^2} + \frac{4p^2}{p^2}}\right) \quad \text{and} \tag{5.13}$$

$$b = \frac{2}{p} - \frac{8p}{p}\left(\frac{e^{-\frac{p}{2t}} + 1}{\frac{1}{t^2} + \frac{4p^2}{p^2}}\right)\,, \tag{5.14}$$

from which the phase delay compared to a sine wave can be calculated with Equation (4.4). With the function $Df(t)$ = atan(a/b) known, a measured phase delay could be related to the frequency independent time constant t of the heat source, when the actual phase delay f and the additional phase delay $Df(t)$ are known. To minimize the influence of measurement errors when calculating the time constant, a differential method could be employed. For a series of measurements with two frequencies and the assumption that the averaged value for a semi-infinite body is the same for both frequencies, t could be calculated from the measured total phase delay and $f_{semi\text{-}infinite}$ by adapting t to minimize the error for both frequencies. However, the experiments indicated that the analytical approach above is too simplified to capture the time-behavior of halogen lamps as accurately as desired. In addition, the experimentally derived time delay showed greater frequency dependency than the equations suggest, rendering invalid the concept of a frequency independent time constant t. A numerical first law analysis of the transient heating and cooling of a wire including electric heating with the temperature dependent resistance of tungsten and convective heat losses, shows that the radiative power over time indeed does not quite match the plot shown in Figure 5.3. Because of the nonlinear relation of the temperature and the radiative power, the gradients of the radiation heat flux when switching on and off are different. The asymptotic approach of a steady state value is slower, leading to a stronger dependence of the time delay on the modulation frequency. The model calculations indicate a time delay that is 14% higher for p = 10 s than for p = 5 s and 27% higher for p = 20 s. Experiments to measure the time delay were carried out on the semi-infinite body used for calibration. The results given are averaged from multiple runs with a standard deviation of 5 ms. The time delay for Osram Ministar 50 W halogen spotlights turned out to be 139 ms at 0.2 Hz and 155 ms at 0.1 Hz for modulation between 20% and 100% input power. For 150 W floodlight-style halogen lamps, the time delay was 106 ms at 0.2 Hz, 113 ms at 0.1 Hz and ca. 150 ms at 0.05 Hz, for a modulation between 20% and 100%.

5.1.4 Data Processing Validation

The temperature data processing to derive the phase delay from the temperature data measured with an IR camera are shown in the previous validation efforts to work well in conjunction with the whole experimental setup. However, the algorithms described in Chapter 4 that compute the phase delay, can be conveniently studied in detail and validated with arrays of test data without any influence of the experimental conditions. Such test data are data closely resembling the measured temperature-time data from the IR camera but are derived from mathematical functions as described in 5.1.3, with known phase delay and amplitude. The outcome of the data processing, the phase delay, phase synchronization and the amplitude can be compared to the predetermined values from the test data generation. Errors in the program can be debugged and inaccuracies recognized and reduced by optimizing the algorithms. The test data included sinusoidal and “delayed” square-wave functions, Equation (5.10), that are similar in shape to temperature data from a surface under oscillating heat flux. The analytical solution for the Fourier coefficients, (5.13) and (5.14), provides the phase delay for the square wave data. To imitate temperature data from scanner cameras like the Agema 900, the test data includes frames with pixels that have a row-column wise consecutively progressing timing of the temperature-time function. The data can be superimposed with noise to simulate realistic conditions. The use of delayed square-wave temperature data in addition to sinusoidal data not only provides a more realistic shape of the temperature curve, but also allows testing and fine-tuning the square-wave phase synchronization procedures. The validation of the data processing algorithms showed no phase errors for perfectly sinusoidal data and relative phase errors of less than 0.5 % for the numerical integration of square-wave test data for the entire range of realistic parameters regarding phase, amplitude, frequency, frame rate and noise.

5.2 Theoretical Validation

The theoretical validation aims on verifying the mathematical model that relates the temperature response data to the convection coefficients. This is achieved by feeding the model with simulated ‘measurement’ data and comparison of the model output to the simulation input. The data is generated with the FEM program ANSYS. ANSYS is a market leading FEM program developed since the 1970’s with a solid track record of accuracy. Based on the ANSYS simulated surface temperature output data, the numerical model calculates convection coefficients. The convection coefficients from the model output are then compared to the original defined as ANSYS input. In case the ANSYS input and the model output is the same, the model yields correct results.

The ANSYS data results from a 3-D simulation of convection in a copper tube. The 20 mm OD copper tube has an inside convection coefficient of 5000 W/m^2K and is heated by a laser spot with an intensity profile over a diameter of 30 mm, sinusoidal modulated with 0.1 Hz. The simulation parameters were chosen in accordance with expected values for the real experiment on the copper tube. For symmetry reasons, the FEM model can be reduced to a quarter of the 1 mm thick unrolled tube wall. A transient simulation was carried out over four oscillation periods with 200 substeps. A phase image of the surface temperature response is shown in Figure 5.4.

The numerical model calculates h = 5137 W/m^2K for these phase data, 3% higher than the original 5000 W/m^2K given in ANSYS. The small error is attributed to different discretization schemes and a certain numerical uncertainty. It is concluded that the numerical model of the heat transferring wall with convection boundary condition and the iterative calculation process are valid.

Besides the validation with data from ANSYS and the calculation of an area-constant heat transfer coefficient, the numerical model is tested with convection coefficients that vary over the evaluated area. In a first step, the numerical model is solved in reverse to yield a phase delay map $f(x,y)$ for a given set of heat transfer coefficients $h(x,y)$. Now the phase delay data is used as an input for the model to calculate a set of convection coefficients. Ideally, the original set would be restored. Figure 5.5 and Figure 5.7 illustrate the original test heat transfer coefficients and the calculated heat transfer coefficients as well as the relative error between both for two cases. In these cases, the convective heat transfer through a 1 mm thick metal plate is considered.

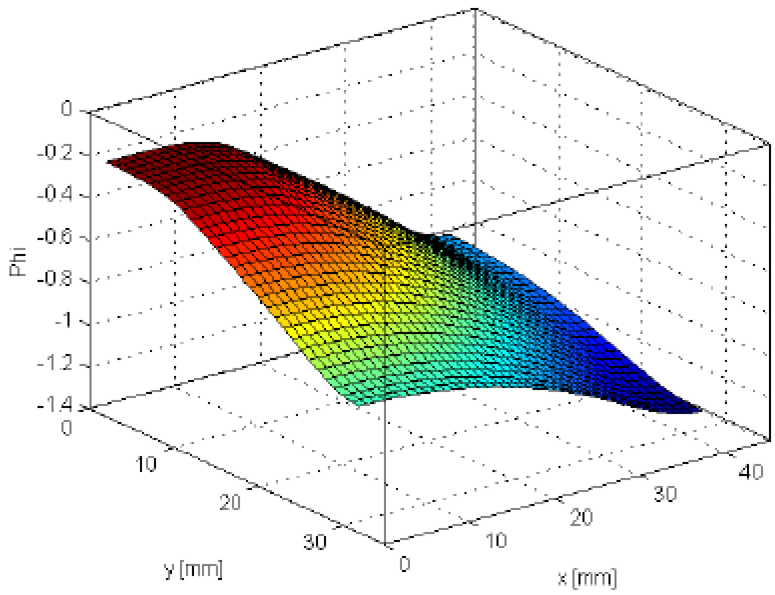

Figure 5.4: Phase image of an ANSYS simulation of a ¼ symmetric tube.

Figure 5.5 shows very good agreement of calculated and test convection coefficients; the gradients of *h(x,y)* are smooth as one would expect in most real world applications. The error RMS is 0.8%. For the second case in Figure 5.7, the parameters are chosen to make the evaluation most difficult: a material (copper) with high thermal conductivity and step-changes of the convection coefficients. The model correctly calculates *h(x,y)* for low gradients. However, near the positions of step changes, the calculated *h(x,y)* is somewhat smoothed out and an error may exist even after hundreds of iterations due to the ill-posed nature of the problem. The error in this case has an RMS of 12% with a maximum of 70 % at the step. Since this error is locally limited, it is considered marginal and acceptable. Lower thermal conductivity, lower wall thickness and smaller mesh spacing will considerably decrease the error. In a repeated calculation at this instant for a thin walled steel structure with a fine discretization, the maximum error at the steps could be reduced to less than 30% with a negligible RMS error of the whole area. It is concluded that Figure 5.5 and Figure 5.7 prove the numerical model capable to calculate local convection coefficients that vary widely over the evaluated area.

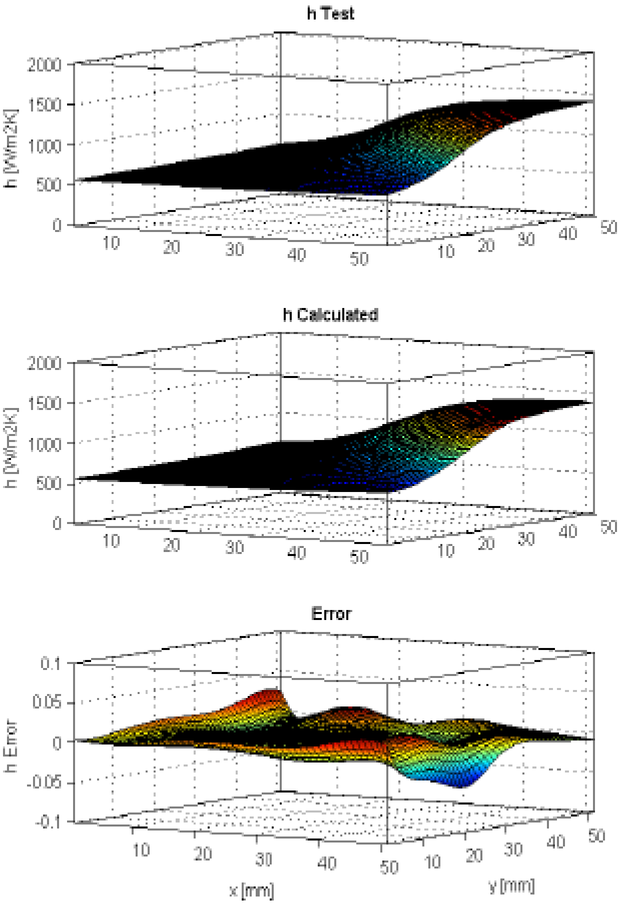

Figure 5.5: Smooth gradients and low error.

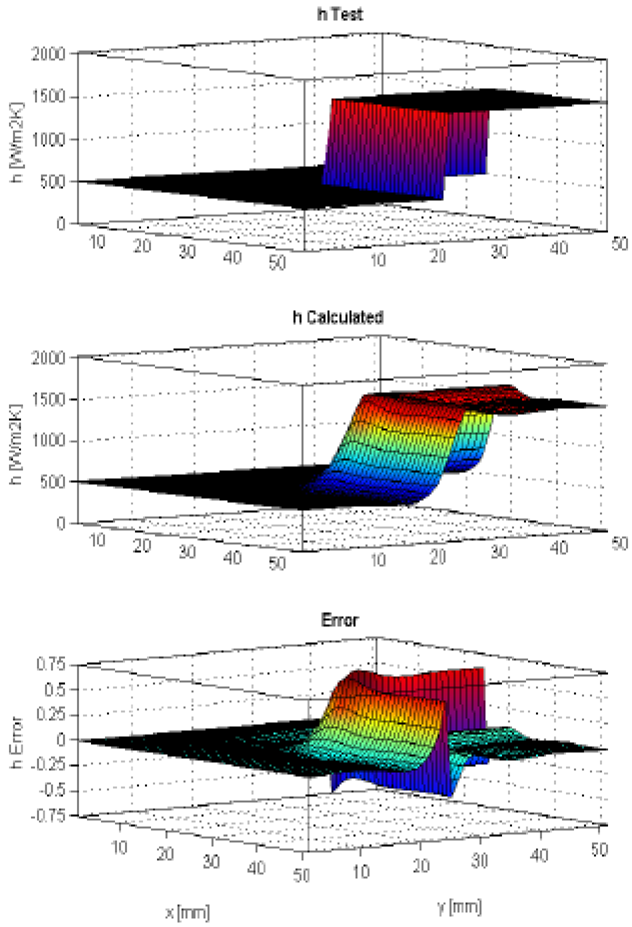

Figure 5.6: Step change, locally high error.

6 Sensitivity Analysis

The aim of this analysis is to investigate how sensitive the calculated heat transfer coefficient responds to uncertainties in the measured phase delay of the temperature. Furthermore, this analysis seeks to find the optimum frequency and show the accuracy of the measurement method that can be expected depending on the experimental parameters.

For this analysis the material parameters, the convection coefficient and the frequency are combined into two dimensionless groups according to Wandelt and Roetzel [1997], the non-dimensional convection coefficient

$$y = \frac{ha}{kdw} \tag{6.1}$$

and the dimensionless thickness

$$x = d\sqrt{\frac{w}{2a}} \quad , \tag{6.2}$$

with a the thermal diffusivity, k the conductivity, d the wall thickness and w the angular frequency. This allows covering the range of all possible experimental parameters with just two variables. Figure 6.1 shows the phase delay f as a function of these dimensionless parameters, derived with the one-dimensional analytic solution.

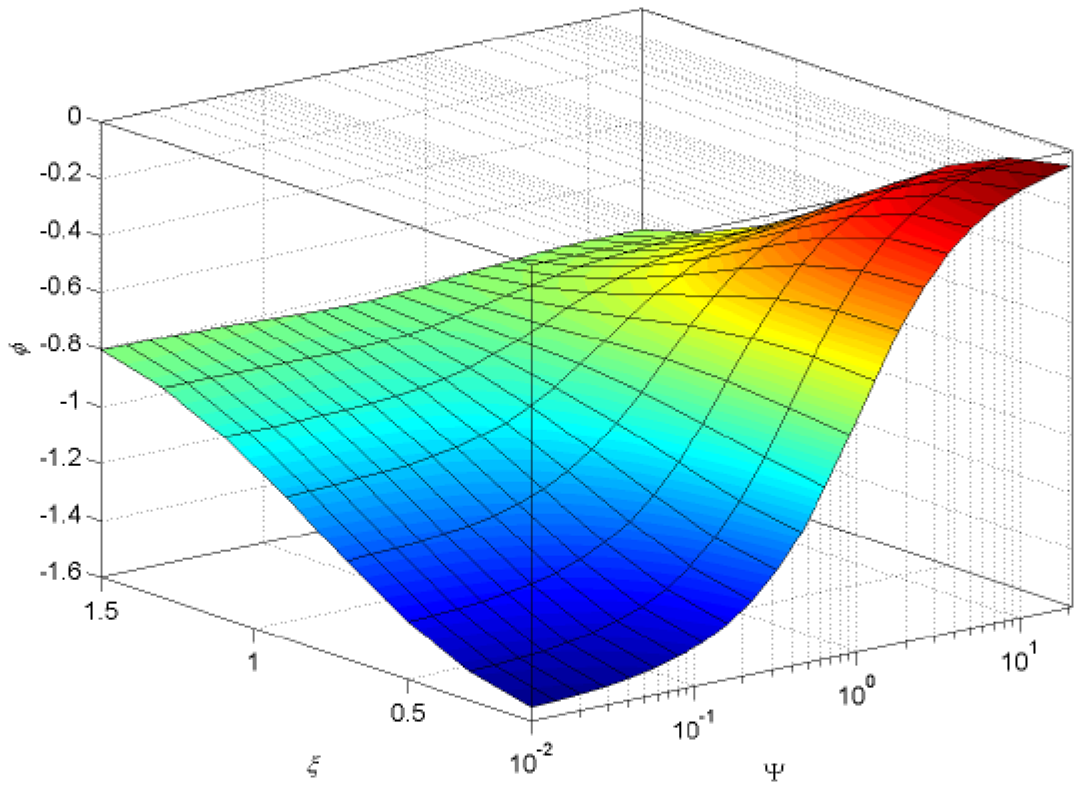

Figure 6.1: Phase delay f as a function of the dimensionless parameters x and y.

6.1 Sensitivity to the Phase Delay

The accuracy of the calculated convection coefficient h relies on the accuracy of the measured variable f when an exact solution for $h(f)$ is provided. The relation of the measurement accuracy and the final error after the calculated is established by defining a sensitivity coefficient such that the relative error *Dh/h* equals the measurement error Df times this sensitivity coefficient. Since the convection coefficient ranges over four orders of magnitude and the relative errors rather than the absolute numbers are of physical significance, h is treated logarithmical. Thus, the sensitivity coefficient X is the derivative of $\log(h)$ with respect to f. With the dimensionless parameters, the sensitivity coefficient becomes

$$X = \frac{\mathrm{d}\log y}{\mathrm{d}f} \tag{6.3}$$

and the relative error of the heat transfer coefficient is

$$\frac{h+\Delta h}{h} = 10^{X\Delta f}. \tag{6.4}$$

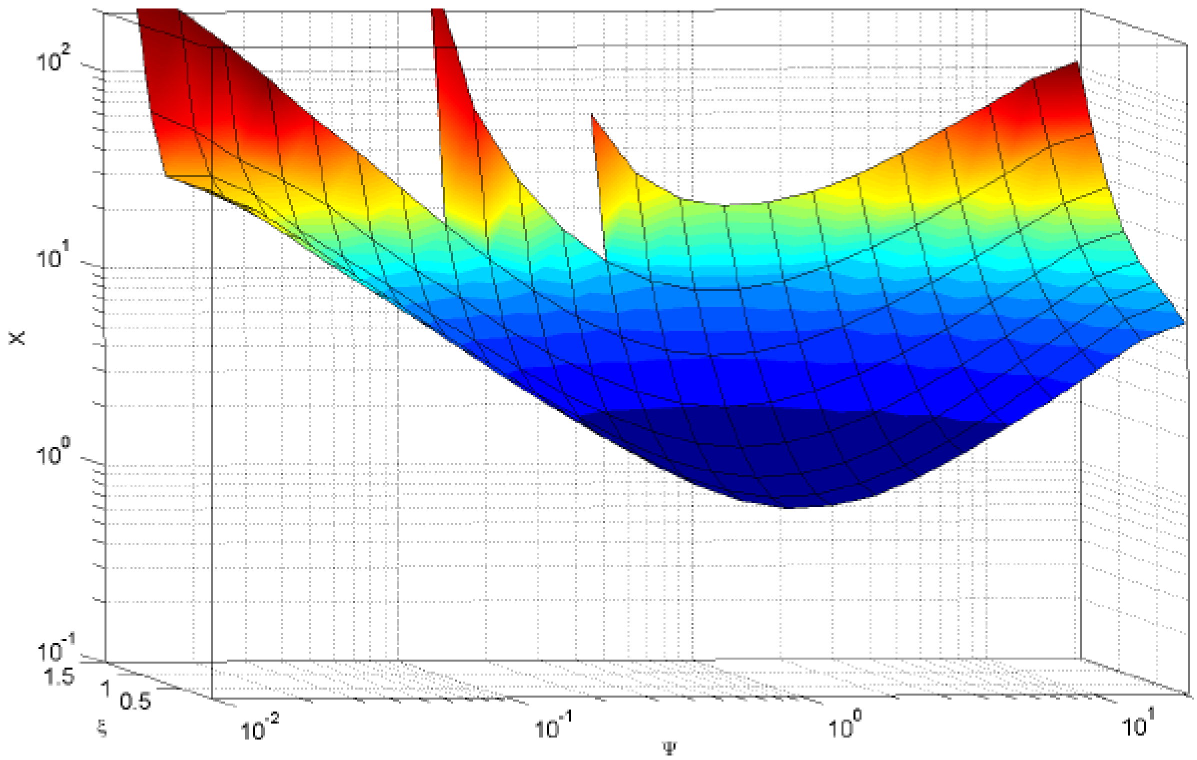

Figure 6.2: Sensitivity coefficient *X* as a function of the dimensionless parameters x **and** y.

The minimum of X = 0.9 occurs near y = 1. Here the relative sensitivity of h to f is lowest; the relative error *Dh* caused by a measurement error Df is at the minimum. Measurements will be most accurate when the convection coefficient and the frequency match to a y near unity. It is evident from Figure 6.1 and Figure 6.2 that with increasing thickness x

the change of y over f decreases, i.e. the sensitivity increases. For $x > 1$, the sensitivity increases disproportional and even jumps to negative numbers, since with increasing thickness the body starts to behave semi-infinite (semi-infinity reached at $x = p/2$). Any attempt to do convection measurements in this region will fail. Ultimately, measurements can only be successful close to the minimum of the sensitivity coefficient, i.e. with a y on the order of unity and a low x.

6.2 Sensitivity to the Material Parameters

The wall parameters d, r, c and k influence the phase delay as they appear in the dimensionless parameter groups. From the definition of y and the functional relationship follows that the relative error Dh/h is linear correlated to a small relative error of the material parameters d, r, and c at constant f, i.e. for $x << 1$. An error of e.g. 5% in any of these leads to an equal error Dh/h. The thermal conductivity k however does not influence y, but only appears in the root term of x. Since the sensitivity of h to x is low, an erroneous value of k of e.g. 10% only leads to an error Dh/h <1% at $x = 0.17$ or <5% at $x = 0.6$. The exact knowledge of the material parameters d, r, and c is of great importance. Unfortunately, d may be difficult to measure; due to the linear relationship, the relative measurement error Dh/h equals at least the error in d.

6.3 Sensitivity to the Outside Heat Transfer

The outside heat transfer in many cases is natural convection and radiation. The combined effect at near-ambient temperature is often several orders of magnitude smaller than the heat transfer coefficient on the inside that is being studied. Therefore the outside surface heat transfer coefficient is neglected in above considerations, set to zero and does not appear in the dimensionless parameters. Only in cases where the measured convection coefficient and the outside heat transfer coefficient are on the same order of magnitude, the outside boundary affects the results and has to be known as accurately as possible to calculate the correct inside heat transfer coefficient h and suppress an error. Although normally of little influence, of course the outside heat transfer coefficient is a boundary condition in the 1-D analytical solution as well as in the numerical model calculations and is generally set to a roughly estimated value depending on the conditions during a measurement.

6.4 Optimum Frequency

With the material parameters and the expected convection coefficient fixed, the angular frequency $w = 2p/p$ is the only independent parameter to be adapted to the experimental conditions. In general, the optimum frequency increases with the heat transfer coefficient. There are practical limits, however, and the measurement setup and equipment specifics must be taken into account. The amplitude is proportional to the period length, i.e. with higher frequency the amplitude may become too small to be measured, this is aggravated by the high heat transfer rate that also reduces the amplitude. The maximum heat source power and the sensitivity of the camera present an upper limit to the frequency. For low heat transfer coefficients and thicker walls, the optimum frequency may become very low; the period length may be too long to generate for the heat source control and the measurement may take too long to maintain steady state, such imposing a lower limit. Concluding from these considerations, the frequency should be picked to yield a y in the range from 0.1 to 10 and a $x < 1$.

6.5 Phase Delay Measurement Error

The error of the measured phase delay is sensitive to two factors, the signal-noise ratio and the phase synchronization. The signal-noise ratio is defined here as the temperature oscillation amplitude divided by the standard deviation of the zero-mean fluctuation of the IR camera's detector. Generally, the signal-noise ratio (SNR) in these measurements is very low, only due to the averaging of hundreds of temperature values within the Fourier transforms any useful data can be derived. The higher the number of frames recorded, the lower the error induced by the SNR. The phase delay error RMS is inverse proportional to the SNR and to the square root of the number of frames. For instance, at a measurement with a frequency of 0.2 Hz and 30 frames per second over three periods, the RMS of the phase delay error is ca. 0.0167 at an SNR of 4, found by statistical analyses conducted in Matlab®. A generalized formula found empirically for the local phase error is given in Equation (6.5), with i the number of frames:

$$\Delta f\left(SNR,i\right)=\frac{\sqrt{2}}{SNR\sqrt{i}} \tag{6.5}$$

This error is the local standard deviation of the phase delay values. Area averaged phase delay values are much less affected by the noise, the SNR induced error decreases with the square root of the number of averaged values. Usually the phase delay values of at least four pixels are averaged before calculating the convection coefficients, reducing the noise induced errors by a factor of at least two. The error in the phase synchronization arises from any inaccuracy in the relation of the heat flux and the frame timing. In case the hardware independent square wave phase synchronization is used, the phase error also depends on the SNR and the number of evaluated periods. For low SNR, the errors of the phase synchronization increases and more periods should be evaluated to gain a better average of the phase angles of the extrema. Typically, the standard deviation of the extrema phase angle is less than half the frame time step. Thus, a maximum phase synchronization error of ½ of the frame time step can be assumed, which is e.g. 0.02 at 30 frames per second. For local values $f(x,y)$, the sum of both errors must be considered while for area-average values the synchronization error dominates.

For focal-plane array cameras, opposed to scanner-type cameras, the noise of the single pixel may be superposed by an additional error from the read-out and image processing circuitry affecting the entire frame.

The errors discussed above do not include any inaccuracies of the heat flux period length and of the frame recording frequency; these errors are hardware dependent and assumed negligible when using digital function generators. The phase delay measurement errors are not systematic and apply to every single measurement, unlike the errors caused by the material parameter uncertainties.

6.6 Uncertainty Propagation

As a conclusion of this analysis, an exemplary uncertainty propagation was carried out to investigate the overall accuracy that can be expected with the errors of all discussed experimental parameters combined. The parameters were chosen for the realistic case of a 1 mm stainless steel wall with a convection coefficient of h_0 = 5000 W/m^{2}K, measured with frequency 0.1 Hz to yield y = 2 and x = 0.3, close to the optimum conditions. The error of the experimental phase delay ϕ_{exp} was assumed to be +/-5%, for the thermal material properties and the wall thickness an uncertainty of 10% and for the density of 5% was assumed, the outside heat transfer coefficient h_d had an uncertainty of 80%. The final relative error Dh/h_0 is 16.8%.

Table 6.1: Uncertainty propagation.

Variable±Uncertainty	Partial derivative	% of uncertainty
h_0 = 5000±842.7 [W/m^2·K]		
c = 500±50 [J/kg-K]	$\partial h_0/\partial c$ = 10.3	37.35 %
d = 0.001±0.0001 [m]	$\partial h_0/\partial d$ = 5.293E+06	39.45 %
h_d = 5±4 [W/m^2·K]	$\partial h_0/\partial h_d$ = -1.408	0.00 %
k = 15±1.5 [W/m-K]	$\partial h_0/\partial k$ = -9.521	0.03 %
ϕ_{exp} = -0.4658±-0.02329	$\partial h_0/\partial \phi_{exp}$ = 13462	13.84 %
ρ = 7980±399 [kg/m^3]	$\partial h_0/\partial \rho$ = 0.6454	9.34 %

Table 6.1 shows the expected local errors at single measurement pixel, area-average errors are lower if the area-averaged phase error is lower. However, due to the inverse nature of the 3-D heat conduction problem, at certain areas with high lateral gradients, systematically larger local errors than predicted in the 1-D analysis might occur, compare to chapter 5 Validation.

7 Fluid Temperature Oscillation Effects

One of the conditions on which the temperature oscillation method is based, is that the local mean fluid temperature is constant in the time domain. This temperature, to which the convection coefficient is related, must not be oscillating, because it is set to zero in the frequency domain of the FDM wall model. This is strictly not always the case in reality, since an oscillating heat flux causes a temperature oscillation in a streaming fluid. For most cases, the fluid temperature oscillation is negligible and does not affect the phase delay of the wall surface temperature since the fluid capacity rate is high. In addition, the length of the heated area in flow direction is often sufficiently short, so that the oscillation amplitude does not become large enough to be effective. However, under certain conditions, such as a low fluid capacity rate or a pronounced boundary layer with low mixing as encountered in laminar flow, as well as for long heated areas, this effect significantly increases the measured phase delay. Although the additional phase delay is dependent on the frequency and becomes smaller with long period lengths, the measurement error of the computed convection coefficients attributed to the fluid temperature oscillation is nearly constant and frequency independent, as is the relative phase delay error caused by this effect. Thus, the convection coefficient cannot directly be calculated from the measured phase delay immediately even when using several measurement frequencies to deduce the unknown error.

A clear distinction must be made between the effects caused by thermal entrance flow, i.e. undeveloped thermal boundary layer and by the fluid temperature oscillation. Both can lead to a similar phenomenon, the heat transfer coefficient appears to decrease in flow direction. However, in the first case the convection coefficient actually varies influenced by the thermal boundary condition and the entrance length, while the second case is a systematic and intrinsic measurement error; the true convection coefficient is only measured in the beginning of the heated zone, where the fluid oscillation is negligible. Both effects may well occur together, further complicating the measurement conditions.

The following equations describe the temperature of a fluid particle at a position *x* along its path under an oscillating heat flux *q*:

$$\dot{q}(x,t) = q_0 \left[1 + \sin\left(wt + \frac{wx}{\mathrm{v}} \right) \right] \tag{7.1}$$

The parameter *t* is the time when the fluid particle passes *x* = 0: $t = t_{x=0} = t(x) - \frac{x}{\mathrm{v}}$. The fluid temperature becomes

$$T(x,t) = T_0 + \frac{1}{d\, r\, c_p} \int_0^x \dot{q}(x,t)\, dx\,, \tag{7.2}$$

and with the integrated heat flux (7.1) evolves into:

$$T(x,t) = T_0 + \frac{q_0}{d\, r\, c_p} \left(\frac{x}{\mathrm{v}} + \frac{1}{w} \left[\cos(wt) - \cos\left(wt + \frac{wx}{\mathrm{v}} \right) \right] \right). \tag{7.3}$$

From this equation can be concluded that the phase delay of the fluid temperature oscillation at position x is

$$Df = -px/p\text{v} \ . \tag{7.4}$$

This consideration neglects the influence of the wall and the convection coefficient. In the real application, the heat flux is specified on the outer wall surface; the actual heat flux on the fluid-wall boundary already has a phase delay compared to the specified outer heat flux and couples the fluid and the wall temperature oscillations via the convection coefficient. The situation cannot easily be described analytically and must be solved numerically. Henceforth the equations above are of limited use, although they illustrate an increasing phase delay resulting from the oscillating fluid temperature. To study the phenomenon numerically, the FDM wall model is extended to incorporate the fluid. Another node is connected to the wall nodes with the lumped fluid properties. The resistance between the wall node and the fluid is the inverse convection coefficient; the fluid nodes are interconnected with the additional phase lag of w/v times the grid spacing (from Equation (7.1)) and have a heat capacity corresponding to the fluid capacity flow per unit width of $\text{v}d_h r c_p$. In Figure 7.1, the phase delay over the length calculated with the harmonic FDM model and a transient FEM model written in Femlab 3.1 is shown. Both methods show good agreement. The parameters are set considering as example a plate heat exchanger channel with a 0.6 mm wall of stainless steel, a hydraulic diameter of 3.4 mm, a velocity of 0.34 m/s and a constant convection coefficient of 10000 W/m^{2}K, the heat flux is modulated with a frequency of 0.1 Hz and 0.2 Hz, respectively.

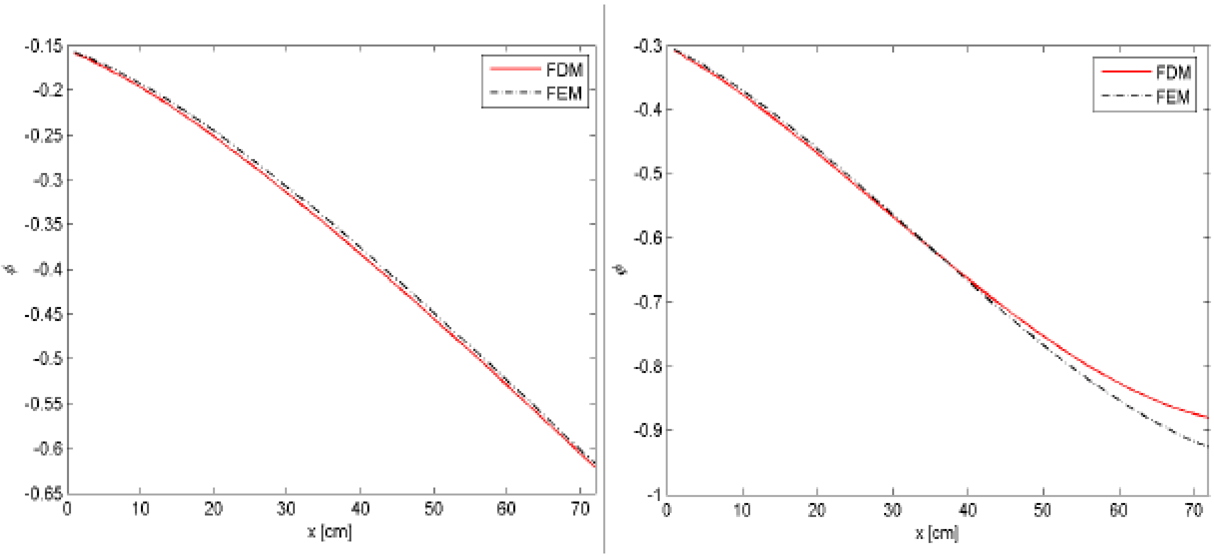

Figure 7.1: Phase delay f versus path length x calculated with a harmonic FDM and a transient FEM model of a PHE channel with water of a velocity v = 0.343 m/s and with h = 10000 W/m^{2}K. The heat flux oscillation period length is p = 10 s (left) and p = 5 s (right).

The numerical results also show an approximately linear increase of the fluid temperature amplitude and phase delay, as suggested by the analytic solution equation (7.4). These results apply to longitudinally constant heat flux only. For a heat flux distribution that varies over the length, the matter becomes more complex; generally, the additional phase delay is higher when the heat flux decreases and lower when it increases over the length.

7.1 Conditions for the Fluid Temperature to Oscillate and Compensation Measures

The effect of an oscillating fluid temperature on the measured phase delay can introduce significant errors in the calculated heat transfer coefficients. To facilitate an a-priori guess whether or not this effect has to be taken into account, a simple rule of thumb was derived from a large number of simulations for water flowing through a channel with varied parameters h, v, and d carried out with the FEM software Femlab 3.1. According to the simulation results, the effect causes a relative phase delay error Df/f that is in the order of an dimensionless group including the length of the periodically heated area in fluid flow direction x times the convection coefficient h divided by the thermal boundary layer thickness d (for internal flow the hydraulic diameter d_h) and the fluid heat capacity flux $\mathrm{v} r c_p$:

$$\frac{\Delta f}{f} \approx \frac{xh}{d \mathrm{v} r c_p} \tag{7.5}$$

This is only a rough estimation; for very short distances x, Df may be less, while for larger x Df behaves nonlinear as shown later in Figure 7.3. The wall thickness may decrease the relative error. The relative phase delay error is almost frequency invariant; it tends to be somewhat less at lower frequencies, however, a multi-frequency differential measurement approach as mentioned earlier seems not to be feasible.

One of the advantages of the TOIRT method is that it is supposed to be completely fluid independent. The fluid temperature oscillation compromises this supposition in that aspect, that the fluid velocity must be high, the hydraulic diameter large and the length of the heated area sufficiently short to keep the error low. If these criteria cannot be satisfied under a given set of measurement conditions, the measured phase delay cannot directly be used for the computation of the convection coefficient. The phase delay data has to be compensated for the additional phase lag caused by the fluid temperature oscillation.

7.1.1 Fluid Temperature Oscillation Phase Delay Compensation

Resulting from the fluid temperature oscillations, the phase delay is not only depending on the wall parameters and the convection coefficient, but also on the heat flux distribution, fluid properties, velocity and channel geometry. A forward calculation of the phase delay for a given set of boundary conditions requires a complete numerical system model. However, when conducting experiments, the surface heat flux is not known exactly, neither is the fluid velocity known and perhaps not even the fluid properties. Moreover, even with a comprehensive system model, the solution of the ill-posed inverse problem now is virtually impossible. A complete system model would also render irrelevant the unique advantages of the TOIRT method, simplicity, fluid independency and speed.

The measurement error after the computation of the convection coefficient due to the additional phase delay is independent of the oscillation frequency, i.e. starting from the phase delay only, no distinction can be made between the phase delay caused by heat transfer coefficient variation or fluid temperature oscillation. Especially entrance effects have to be considered as they cause a similar phenomenon. In order to compensate for the additional phase lag resulting from the fluid temperature oscillation, the effect has to be recognized and certain suppositions applied to find a curve to expressing the additional phase delay over the length and separate it from the convection caused phase lag sought after. Assuming the convection coefficient is either fairly constant over the length, or at least fluctuating around some mean value, a low-order curve fit of the measured phase delay data describes the slope induced by the fluid temperature oscillation along the stream. It is important to distinct between small, local features of the phase delay caused by a varying convection coefficient e.g. on repeating surface structures, such as in plate heat exchangers, and the overlaying additional phase delay caused by the fluid temperature oscillation that is to be matched by the curve. For a sufficient short evaluated length, the curve of the additional phase delay has a monotonic slope with a maximum at the entrance. A curve fit with an exponential sum function with four coefficients has shown to fit perfectly and unlike a polynomial function does not behave vastly unphysical even outside the considered range. This function can be fitted to the general shape of the phase lag over the path length with a nonlinear least square approach.

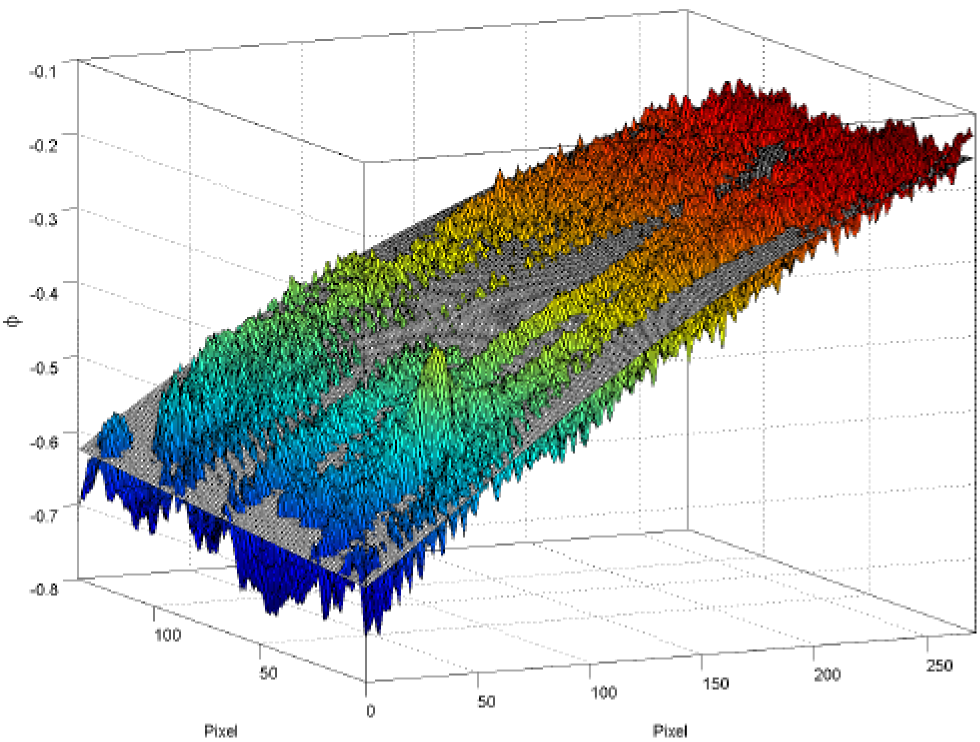

Figure 7.2: Phase delay data from a PHE measurement with a fitted surface for compensation.

For a 2-D data array, both dimensions are fitted with curves to yield a surface in the Cartesian plane that matches the fluid temperature oscillation induced gradients of the phase delay as shown in Figure 7.2. Since this fitted surface neglects all local features of the phase delay caused by convection only, its value can be subtracted from the measured phase delay array $f(x,y)$. Now the maximum value of the surface is added to that difference and this sum is the compensated phase delay data.

7.1.2 Velocity Determination

The effect of the oscillating fluid temperature can in principle be used to determine the fluid velocity. If the fluid path within the evaluated area is sufficiently long, a phase lag maximum occurs shortly before the location x_{Max} = v$p/2$, leading to the estimated velocity

$$\mathrm{v} = \frac{2}{p} x_{Max} . \tag{7.6}$$

Figure 7.3 below shows the FEM-simulated phase delay of the wall temperature along a duct with a fluid moving with a velocity of v = 0.2 m/s, convection h = 5000 W/m^{2}K, measured with an oscillation period of p = 10 s. The phase lag maximum is located near x = 1 m, resulting in the given velocity according to above formula. A precondition for the application of this velocity estimation method are a constant heat flux and convection along the fluid path, otherwise the phase delay becomes very hard to predict and above simple equation is invalid.

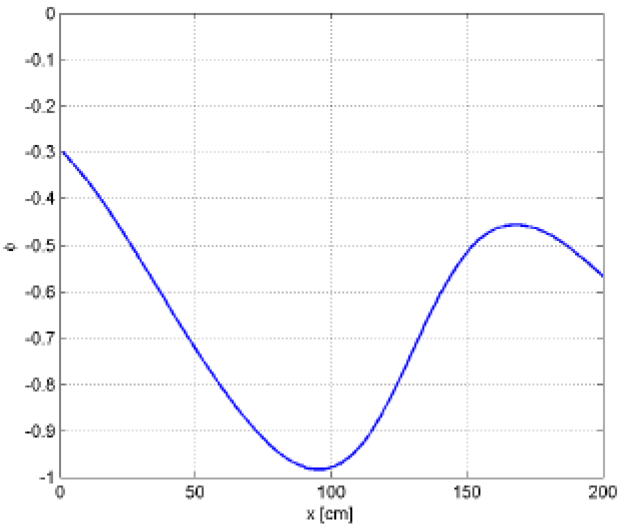

Figure 7.3: Phase delay over the fluid path length at a PHE channel with a velocity of 0.2 m/s and 0.1 Hz.

8 Experiments on Pipe Flow

The first applications of the TOIRT were experiments on pipe flow for testing and validating the measurement technique. The heat transfer coefficients to be expected in pipe flow are well known from various Nusselt number correlations and confirmed by a large number of experimental data available in literature. For the Nusselt number in single-phase turbulent pipe flow, the correlation developed by Gnielinski [1975] is widely regarded as the most accurate. A comparison of the measured experimental values with the numbers from a reliable correlation allows validating the measurement technique.

The local heat transfer coefficient in turbulent pipe flow for constant wall heat flux depends on the Reynolds and Prandtl numbers as well as on the state of the hydraulic boundary layer that develops along the tube between the entrance and a point where its thickness reaches the tube's centerline and the flow becomes fully developed. The Nusselt number decreases from the entrance asymptotically with the length to reach a final value at the point where the boundary layers merge in the center of the tube. Gnielinski's common correlation provides the arithmetic area-average Nusselt number for developing flow within certain tube length. The local Nusselt number Nu_X can be derived from the mean Nusselt number equation by multiplication with the length l and subsequent differentiation with respect to l:

$$Nu_{X,Gni} = \frac{\frac{f}{8}\left(Re - 1000\right)Pr}{1 + 12.7\sqrt{\frac{f}{8}}\left(Pr^{2/3} - 1\right)}\left[1 + \frac{1}{3}\left(\frac{d_h}{l}\right)^{2/3}\right] \tag{8.1}$$

Here f is the Darcy-Weisbach friction factor, also known as the pressure loss coefficient, which is proposed by Filonenko [1954] for isothermal flow in smooth tubes as:

$$f = \left(1.82\log_{10} Re - 1.64\right)^{-2} \tag{8.2}$$

The applicable range of these equations is $2300 < Re < 10^6$ and $0.6 < Pr < 10^5$. The correction term for radial temperature variation dependent properties is left out. This local Nusselt number $Nu_{X,Gni}$ will be used as the reference value for pipe flow. The first term in (8.1) is the fully developed Nusselt number and the second term is the length dependency according to Hausen [1976]. Integration and division by l yields a mean Nusselt number; Hausen as well as Gnielinski did not consider any difference in the mean Nusselt number for constant wall temperature or heat flux. In chapter 1 was outlined that the mean heat transfer coefficient of an area based on the local heat transfer coefficients is different for a constant temperature and a constant heat flux boundary condition, the formulas for the respective calculations are given in equations (1.4) and (1.5). The mean Nusselt number according to Hausen that is formed as an arithmetic area-average is mathematically exact only for constant temperature difference.

8.1 Preliminary Experiments

Preliminary experiments were carried out to investigate the convection coefficients of water flowing through the entrance region of a copper tube (OD 20 mm, 1 mm wall thickness). The convection coefficients in the entrance region are affected by the development of the hydraulic boundary layer and therefore dependent on the entrance length. The flow was slowed down to obtain uniform conditions before entering the right angle edge entrance; measurements were taken on various distances from the tube entrance. The evaluated area is 20 x 40 mm^2, heated with a laser with an approximately Gaussian intensity profile. The convection coefficient on this area was calculated with the 3-D FDM numerical model of a tube wall section by minimizing the phase delay error between the computed and the experimental values through adaptation of *h*, which is not a function of the local plane coordinates *x* and *y* here but an average value within the small evaluated area. The experimental set-up includes the following components:

- A fiber-coupled laser diode array with a wavelength of 685 nm providing 15 W optical power with a Lambda 50A programmable power supply
- An Agema 900 LWB IR scanner that records the surface temperatures with a spatial resolution of 272 x 68 pixels and 30 frames/s.
- IRLockIn® Software, IR frame grabber and function generator heat source control PCI-card [AT, 2002]

A photograph of the setup is shown in Figure 8.1. The laser optic is connected with the red fiber to the diode array and positioned in about 100 mm distance from the tube, next to the camera’s lens.

Figure 8.1 Photograph of the setup: Camera, laser fiber (red, in front of the lens) and tube.

The results of the experiment are shown in Figure 8.2 as the measured local Nusselt number $Nu_{X,Exp}$ versus the dimensionless length *l/d* for two Reynolds numbers in the developing and fully turbulent range and the reference values according to (8.1). A reason for the scatter of the experimental data points are errors in the time-frame synchronization used in these measurements, which can cause errors of the phase delay as the real frame timing with respect to the heat flux is uncertain by +/- 1 frame. These deviations notwithstanding, the mean experimental values appear to be higher than the values calculated in accordance to Gnielinskis's correlation. This is attributed to a very thin, undeveloped thermal boundary layer around the evaluated area in these experiments that is different from Gnielinski's experimental conditions of a fully developed thermal boundary layer with constant heat flux or temperature. Based on these results, a more detailed investigation was launched to answer the question of how the thermal boundary layer caused by the measurement itself affects the measured values. In the following section, some theoretical considerations are outlined that are subsequently tested by improved experiments.

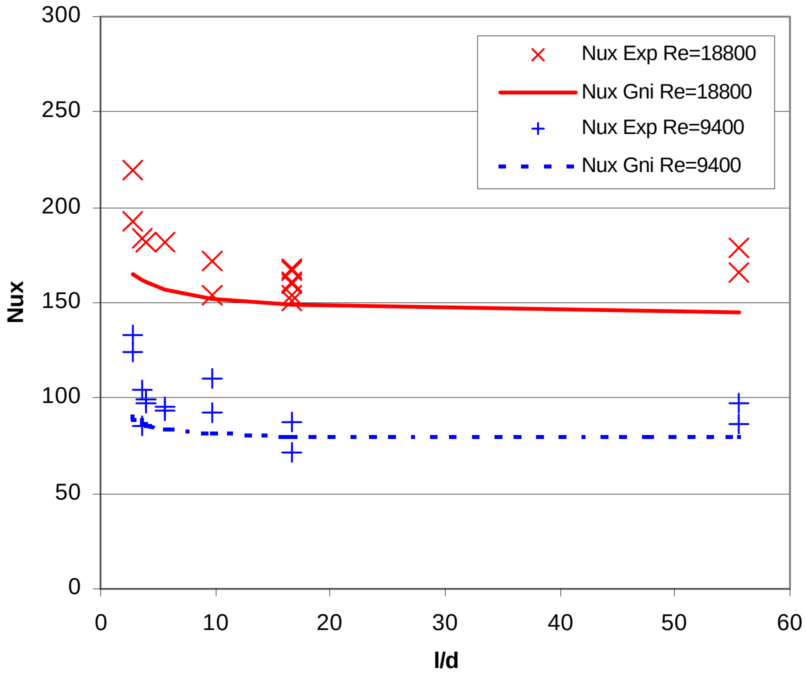

Figure 8.2: Preliminary experimental results showing a comparison of the measured local Nusselt number and Gnielinski's correlation for the entrance of a tube.

The deviations between the measured and the predicted local Nusselt numbers are specifically apparent in the entrance of the tube at low values *l/d*. This is an entrance effect caused by the right angle edge entry of the tube and is further discussed in section 8.3.

A validation of the experiments against values from a CFD simulation of heat transfer in the entrance section of a pipe is arguably doomed to failure, as even elaborate CFD simulations with advanced turbulence models, as well as LES or DNS calculations of the turbulent heat flux are too uncertain to be used for verification. A comparison of CFD simulation of fully developed pipe flow using various turbulence models with the Dittus-

Boelter equation by Benim, Cagan and Gunes [2004] showed deviations up to 11% for low Reynolds numbers and up to 6% for higher *Re*. Using explicit algebraic stress models, however, Rockni and Gaski [2001] obtained a Nusselt number as close as 2% to the same reference correlation for fully developed flow in a rectangular duct at *Re* = 12000. Developing flow is still harder to compute and the results of the CFD simulations that will be shown in chapter 12 Plate Heat Exchangers for rather complex flows also lead to the conclusion that CFD is not an appropriate tool for validating experiments.

8.1.1 Review of Convection and Boundary Layer Theory

Boundary layers exist along the wall in moving fluids. The boundary layer is defined as the region of the fluid next to the wall where properties are affected by the wall and distinct from those of the free streaming fluid. Conventionally, the boundary layer ends where the properties reach 99% of their values in the free stream. The concept of the boundary layer is historically due to Prandtl [1904], for the sake of brevity, no general review of boundary layer theory (see e.g. Schlichting [1979] or Kays, Crawford, Weigand [2005]) will be provided here, but an attempt to explain certain phenomena of relevance to the measurement method. There are two kinds of boundary layers that affect the convective heat transfer, the thermal and the hydraulic boundary layer. Starting at the edge of the pipe entrance with zero thickness, the hydraulic and, from the point on where heat transfer is present, also the thermal boundary layer develop along the pipe until finally reaching a thickness of half the pipe diameter, from where the flow conditions start to be considered fully developed. The hydraulic respectively the thermal entrance region in tubes is specified as the region where the conditions are not fully developed. The Prandtl number as the ratio of momentum to thermal diffusivity determines which boundary layer develops faster, the thermal for $Pr < 1$ or the hydraulic boundary layer for $Pr > 1$. The hydraulic boundary layer describes the layer of fluid where the velocity is influenced by the wall and differs from the flow in the center, with a velocity profile decreasing to zero at the wall in the viscous sublayer, where any turbulences approach zero as well. The total thickness of the boundary layer and the turbulences within the boundary layer determine the transport of heat between the bulk fluid and the wall. Thus, the convection coefficient heavily depends on the hydraulic boundary layer. The thermal boundary layer comprises a wall-neighboring layer of fluid, in which the temperature is affected by the wall temperature and differs from the bulk temperature of the free streaming fluid. Under isothermal conditions and without internal heat generation due to viscous dissipation, no thermal boundary layer will develop; this is approximately the case under the experimental conditions up to the point where measurements are taken and the oscillating heat flux is applied. The thickness of the thermal boundary layer strongly influences the convection coefficient as it poses a thermal resistance to the heat flux. In these experiments, a thermal boundary layer develops along the evaluated area under the influence of the oscillating heat flux on the tube surface. Here the question arises how far the measurement itself affects the measured parameters. Henceforth emphasis will be laid on the thermal boundary layer caused by the local heat flux.

Ideally, an analytical equation for the Nusselt number for turbulent internal flow with axially and circumferentially varying heat flux would be found to describe the convection coefficient under the experimental conditions and possible deviations from Equation (8.1).

However, unlike convection under laminar conditions, which lent themselves more readily to analysis, efforts to mathematically describe turbulent convection are extremely difficult and (semi-) empirical correlations are used where available. An analytical approach to the temperature profile in turbulent pipe flow under an arbitrarily specified heat flux profile is described by Siegel and Sparrow [1959]. This approach, however, could not be successfully implemented by the present author for the analysis of the turbulent thermal boundary layer and the heat transfer coefficient expected under the experimental conditions. The issue is similar to the turbulent Graetz problem though more difficult to solve. The Graetz problem is to find an analytical solution for a Nusselt number under thermally developing flow with constant wall temperature. It is solved with infinite series eigenvalue solutions, for which coefficients can be found tabulated for many Reynolds and Prandtl numbers [e.g. Kakac, Shah and Aung, 1987].

For laminar flow, the convection coefficient is directly related to the thermal boundary layer and the heat flux profile. Analytical and FEM computations of the boundary layer and the convection coefficient have been obtained. A step change in the wall heat flux profile leads to a peak in local Nusselt number; for a constant heat flux profile, the Nusselt number asymptotically approaches the well-known value of 4.36 after a rather long thermal entrance section. For turbulent flow of fluids with higher Prandtl numbers, the thermal boundary layer has a much smaller effect on the convection coefficient and develops much faster. This is observed as the thermal entrance length, defined as the range where $Nu_X > 1.05\ Nu_{X,Inf}$, is very short, ca. < 5 d_h, with the maximum Nu_X at the beginning ca. 40 % higher (for air, $Pr = 0.7$, at $Re = 100000$ [Boelter et al, 1948]). Less heat transfer resistance due to a thinner boundary layer causes the entrance effect. Generally, entrance effects are more pronounced for low Prandtl number fluids, which may even in turbulent flows behave like under laminar conditions due to high ratio of molecular diffusion to turbulent diffusion. The reason for the strong Pr dependence of entrance effects is that the turbulent flow temperature profile for $Pr > 1$ is mainly shaped within the viscous sublayer and develops rapidly [Lienhard and Lienhard, 2001], in stark contrast to liquid metals with $Pr \ll 1$. For high Prandtl number fluids, the principal mechanism of turbulent heat transfer is turbulent diffusion, whereas the heat transfer in the viscous sublayer takes place mostly due to molecular diffusion, as turbulences decrease to zero closer to the wall. At the outer border of the sublayer, small fluid volumes are exchanged in turbulent bursts with the fully turbulent region of the boundary layer and provide high heat and mass transfer rates. Because the heat transfer resistance is concentrated in this very thin near-wall region of the hydraulic boundary layer, the upstream history of the fluid should not influence the heat transfer; constant temperature or constant heat flux conditions are indifferent, changes in the heat flux profile should not drastically affect the convection coefficient. Thus, it is commonly assumed in literature that the turbulent heat transfer coefficient for a fluid with a high Prandtl number ($Pr > 1$) is mainly dependent on the Reynolds number and largely independent of the heat flux profile [Kays, Crawford, Weigand, 2005; Kakac, Shah, Aung, 1987; Lienhard and Lienhard, 2001]. Contrary to this belief, the experiments found heat transfer coefficients higher than suggested by Nusselt number correlations. If the measured heat transfer coefficient is influenced by the thermal boundary layer even in fully turbulent flow, two consequences should be observable: First, the influence should decrease with increasing turbulence, i.e. at higher Reynolds numbers. Second, the influence should decrease with the boundary conditions approaching constant heat flux, i.e. when the heated area becomes axially longer and the heat flux gradients smaller.

Both have been investigated in improved experiments.

From these thermal boundary layer considerations also follows, that for axially increasing heat flux, the convection coefficients should also increase as compared to a constant heat flux, with the opposite for decreasing heat flux. This has been experimentally observed over the length of 40 mm of the evaluation area and the bell curve intensity profile of the laser induced heat flux. It turned out in the experiments that the amplitude, the phase delay and the mean wall temperature increase in fluid stream direction. Both can be explained with the development of the thermal boundary layer within the evaluated zone. Similar observations can be found at Prinzen [1991]. Prinzen also pointed out, that the time averaging during measurements over multiple oscillations yields the same convection coefficients as for steady state, although strictly speaking boundary layer effects result in increased convection coefficients during the increasing half of a period and decreased values for the other half. Time averaging and spatial averaging over the evaluation area led to the reported numbers, which should equal the steady state value for the respective heat flux profile.

For studying the heat flux profile effects, an improved experiment was set up with a tube with lower thermal conductivity and larger diameter.

8.2 Improved Experiments

These experiments were conducted on the entrance section of a tube made of 1.4301 / ANSI 304 stainless steel (25 mm OD, 1 mm wall thickness). Like before, water was pumped through the pipe with a temperature of 25°C and the measurements were taken at various distances from the entrance to capture the effects of hydraulic boundary layer development. The effects of the heat flux profile applied with the laser were studied by variation of the laser-to-surface distance, also the Reynolds number was varied. With a laser spot with a Gaussian mean radius of 7 mm and a Reynolds number of 8700, which is considered to be at the upper end of the transitional range between laminar and turbulent flow, the measured values were on average 73% higher than the reference convection coefficient according to Gnielinski’s correlation for constant boundary conditions. At a Reynolds number of 17500, which is well within the fully developed turbulent region, the difference between the reference and the measured value was about 44%. Next the heated area was extended and the heat flux gradients smoothed out by increasing the Gaussian mean radius of the laser spot to 20 mm. At the same Reynolds number the difference of the measured to the reference values from Gnielinski’s correlation was reduced from 44% to 27%. For Re = 49000, the measured values finally coincided with the predicted numbers for constant heat flux as shown in Figure 8.3. This shows, as theorized in the boundary layer consideration, that the heat flux profile effect on the measured Nusselt numbers is more pronounced at smaller Reynolds numbers with lower turbulence.

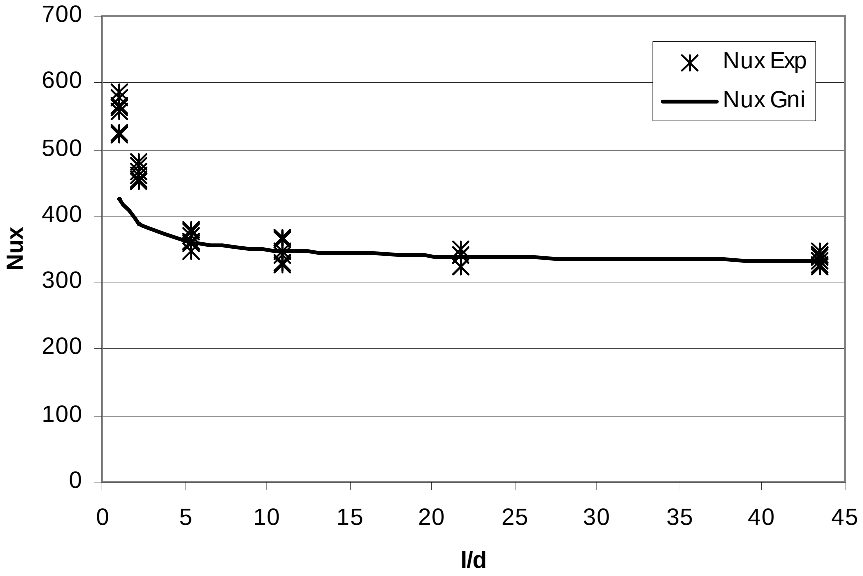

Figure 8.3: Local Nusselt number in turbulent pipe flow for water with Re = 50000

8.2.1 Laminar Flow and the TOIRT

As discussed above, measuring convection coefficients becomes increasingly difficult with decreasing turbulence. Laminar flows can generally not be measured with the TOIRT for two reasons: First, even at comparatively short lengths of the evaluated area, the laminar boundary layer will lead to downstream fluid temperature oscillations due to a lack of mixing with the bulk fluid at the temperature to which the convection coefficient is related. Second, the heat transfer coefficient in laminar flow is, much more so than in low turbulent flow, dependent on the heat flux and the wall temperature profile. Consequently, convective heat transfer in laminar flow can only be measured by a steady state technique applying the exact heat flux profile of the application in question, with all the resulting experimental complexities. However, it may be possible to estimate laminar flow convection with the TOIRT when the oscillation frequency is very low, reducing the temperature oscillation effect, and the profile of the applied heat flux is smooth and similar to the actual application for which the heat transfer coefficient is to be evaluated.

Fluids with very low Prandtl numbers, e.g. liquid metals, have, even in fully turbulent flow, similar heat transfer characteristics as for laminar flow, since the high thermal conductivity dominates over turbulent heat diffusion. For that reason the TOIRT is also limited by the fluid’s Prandtl number, measuring convection with liquid metals may pose considerable difficulties.

8.3 Pipe Flow Conclusions

The experimental results strongly support the outlined theory that the thermal boundary layer significantly affects the heat transfer coefficients even in turbulent pipe flow at Reynolds numbers smaller than 50000. The experiments showed that this effect, as theorized, decreases with increasing Reynolds numbers as well as decreasing axial heat flux gradients. Future work may be aimed at a number that relates the Reynolds number to the axial gradient of the heat flux and establishes a limit above that the thermal boundary conditions of turbulent pipe flow do not affect the convection coefficients.

For measurements at lower Reynolds numbers, effects of the thermal boundary layer caused by the measurement itself must be taken into account. The measured results in these cases are valid only for the heat flux conditions of the measurement, predictions of convection coefficients for heat flux profiles other than measured are to be made with great caution. Consequently, convection coefficients in a certain application are measured best with the same heat flux profile as expected in the real application, the profile may nonetheless have a much lower magnitude.

In spite of the difficulties with the convection coefficient's dependence on the applied heat flux profile itself, the experiments proved that the TOIRT method could measure heat transfer coefficients in a pipe entrance very well. Under certain conditions, the values from a well-established correlation were reproduced. The results show a larger increase towards the entrance than Gnielinski's correlation suggests. Thus, the factor with dimensionless length $1+(l/dh)^{-2/3}$ underestimates the entrance effect of a right angle edge entry for pipe flow for water. A comparison of the measured Nusselt numbers $Nu_X/Nu_{X,Inf}$ normalized for the fully developed Nusselt number with Gnielinski's correlation and data from measurements with air from Boelter et al. [1948] is shown in Figure 8.4.

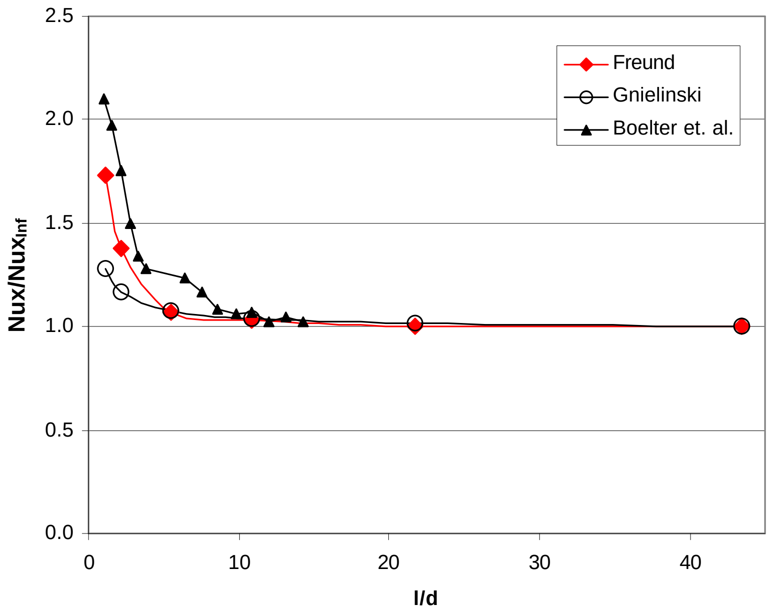

Figure 8.4: Comparison of normalized local Nusselt numbers in the entrance region of a pipe.

The numbers from Boelter are even higher, which is likely due to the lower Prandtl number of air. From the current measurement data, Equation (8.3) has been derived to fit the normalized Nusselt number in a right angle edge entrance (with a regression coefficient of 0.99 and an RMS error of < 4%):

$$\frac{Nux}{Nux_{Inf}} = 1 + 0.822\left(\frac{l}{d_h}\right)^{-1.183} \tag{8.3}$$

Equation (8.3) is suggested to be used as an entrance length depending factor for the increase of the local Nusselt number. The range of applicability for Equation (8.3) is turbulent flow with a Prandtl number on the order of 7 in a sharp edge entrance pipe for $l/d_h > 1$.

The mean Nusselt number for a tube with constant boundary condition at length l from the entrance is larger than the local Nusselt number but asymptotically approaches $Nu_{X,Inf}$ at a sufficiently long distance from the entrance. The integral of the local Nusselt number with respect to the entrance length l/d_h, and subsequent division by l/d_h would give a factor reflecting the influence of the tube length for the arithmetic area-average Nusselt number Nu. However, the function is indefinite at zero and the actual values near the entrance are not known. Any such integral equation with an exponent approaching -1 will have a pole at zero and produce unphysical large numbers at the very entrance. Henceforth Gnielinski's equation that matches the experimental values for $l/d_h > 5$ very well should be used for the mean Nusselt number Nu at $l/d_h > 5$:

$$\frac{Nu}{Nu_{X,Inf}} = \frac{d_h}{l}\int_0^{\frac{l}{d_h}} 1+\frac{1}{3}\left(\frac{l}{d_h}\right)^{-\frac{2}{3}} \mathrm{d}\left(\frac{l}{d_h}\right) = 1+\left(\frac{l}{d_h}\right)^{-\frac{2}{3}} \tag{8.4}$$

This area-average Nusselt number is in accordance with equation (1.4) applicable to constant wall temperature. The equivalent Nu for constant heat flux conditions as formed with equation (1.5) becomes

$$\frac{Nu}{Nu_{X,Inf}} = \frac{\frac{l}{d_h}}{\int_0^{\frac{l}{d_h}} \frac{1}{1+\frac{1}{3}\left(\frac{l}{d_h}\right)^{-\frac{2}{3}}} \mathrm{d}\left(\frac{l}{d_h}\right)} = \frac{1}{1-\left(\frac{l}{d_h}\right)^{-\frac{2}{3}} + \frac{1}{3}\sqrt{3}\,\frac{d_h}{l}\,\mathrm{atan}\left(\sqrt{3}\left(\frac{l}{d_h}\right)^{\frac{1}{3}}\right)} . \tag{8.5}$$

Both length-dependency factors for the mean Nusselt number are plotted in Figure 8.5. While the constant heat flux (q) case has always a lower mean Nusselt number, the difference of both values decreases with the entrance length; at $l/d_h = 10$, the difference between both mean Nusselt numbers is only 4.3%. When considering that the length-dependency factor in (8.1) as well as in (8.4) is not an analytical exact number for the developing pipe flow but rather a simple approximation for the effect of common entrance configurations on the local respectively the average Nusselt number, there likely remains little incentive for the use of the rather cumbersome equation (8.5).

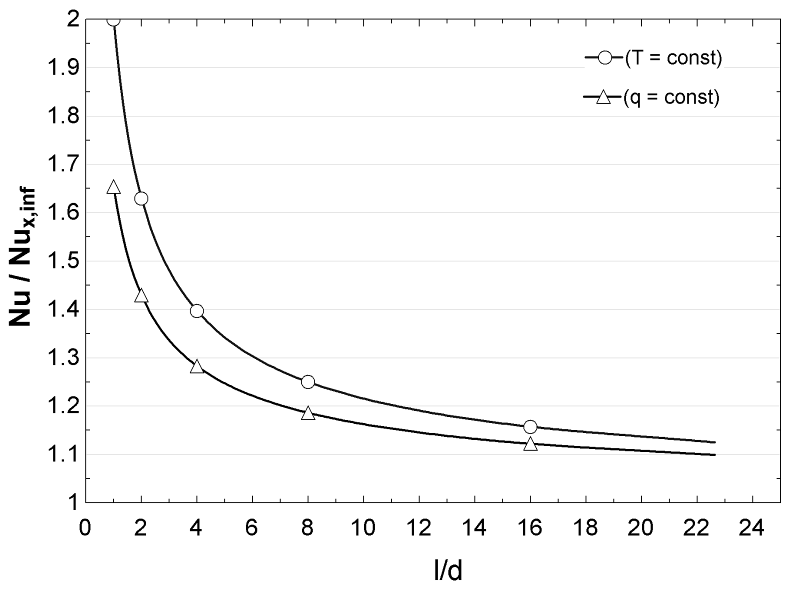

Figure 8.5: Length dependency of the mean Nusselt number for the (T) and (q) boundary condition.

9 Vortex Generators in a Wind Tunnel

9.1 Heat Transfer Enhancement from a Single Vortex Generator

The Temperature Oscillation IR Thermography Method was applied to study the influence of aerodynamic vortex generators on the wall heat transfer in airflow. This study was motivated to compare different experimental methods from three project partner groups on a well-defined setup. The vortex generators (Figure 9.1) are suggested for heat transfer enhancement for example for the cooling of turbine blades. In real applications, the vortex generators (VG's) are small surface structures of tetrahedral geometry that are arranged in arrays on the cooling area [Henze et al, 2005]. Such a vortex generator induces turbulent longitudinal vortices in its wake, thus increasing the heat transfer on the wall in the downstream area. The TOIRT method is particularly well suited for this application, since a large heat transfer area can be evaluated at once and the measurements can be taken conveniently from the outside of the channel.

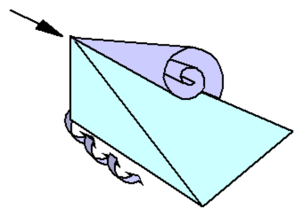

Figure 9.1: Vortex generator with initial vortices

The model vortex generator used in this study is 52 mm high, 65 mm long and 65 mm wide. It is mounted onto the inside of the wind tunnel wall (Figure 9.2). The wind tunnel is rectangular with a cross section of 400 x 200 mm^2. The radial blower allows Reynolds numbers Re = vD_h/ν up to 450,000 based on the mean velocity v and the hydraulic diameter D_h = 0.2667 m. The blower speed is controlled with a variable frequency drive. The airflow velocities are calculated based on the pressure reading from a Venturi tube and were validated by means of a hot wire anemometer, the airflow temperature is always kept near 20°C. The side wall of the wind tunnel is made of 0.5 mm stainless steel and coated with black spray paint (ε = 0.95). The evaluated area is 600 x 300 mm^2. Even though the area is large, artifacts in the measured data associated with temperature oscillations of the boundary layer are insignificant as the velocity, capacitance rate and turbulence of the fluid are high. An array of eight 150 W halogen floodlights is used as a heat source. A photograph of the setup is shown in Figure 9.2. The measurements were taken with an AGEMA THV 900 scanner with a resolution of 272 x 136 pixels and 15 frames per second; the period length of the sinusoidal oscillations was 20 s. Three periods per measurement with a total of 900 frames were recorded. The temperature data processing includes the drift compensation procedure to eliminate a considerable temperature drift. The convection coefficients were computed with the FDM model with a resolution of 5 mm in the x-y plane and four nodes for the wall thickness. The results for three turbulent Reynolds numbers shown in Figure 9.3 are averaged from four measurements each to reduce noise and improve the accuracy.

The results clearly show the characteristic double longitudinal vortices, their intensity is increasing with the Reynolds number. The maximum heat transfer occurs right behind the vortex generator in the downwash region where the two main vortices merge. Also small horseshoe vortices form around the leading edge of the vortex generator. The maximum convection coefficient in the wake of the vortex generator is ca. 220 W/m^2K at Re = 450,000, 150 W/m^2K at Re = 300,000 and 70 W/m^2K at Re = 80,000.

Figure 9.2: Wind tunnel and steel wall segment with vortex generator mounted inside (at the triangle), camera and halogen floodlight array in the front.

This study on vortex generators was conducted in collaboration with two project partner groups who performed convection measurements on the same geometry. So we had the unique opportunity to directly compare three different measurement methods for local convection coefficients. The group at the Institute for Aerospace Thermodynamics at the University of Stuttgart did measurements on the same vortex generator in a similar wind tunnel with TLC method, as well as numerical investigations [Henze et al. 2005]. Shown in Figure 9.4 is a comparison of the convection coefficients for three Reynolds numbers derived with both methods. The data shown is measured on the centerline behind the vortex generator. We found very good agreement.

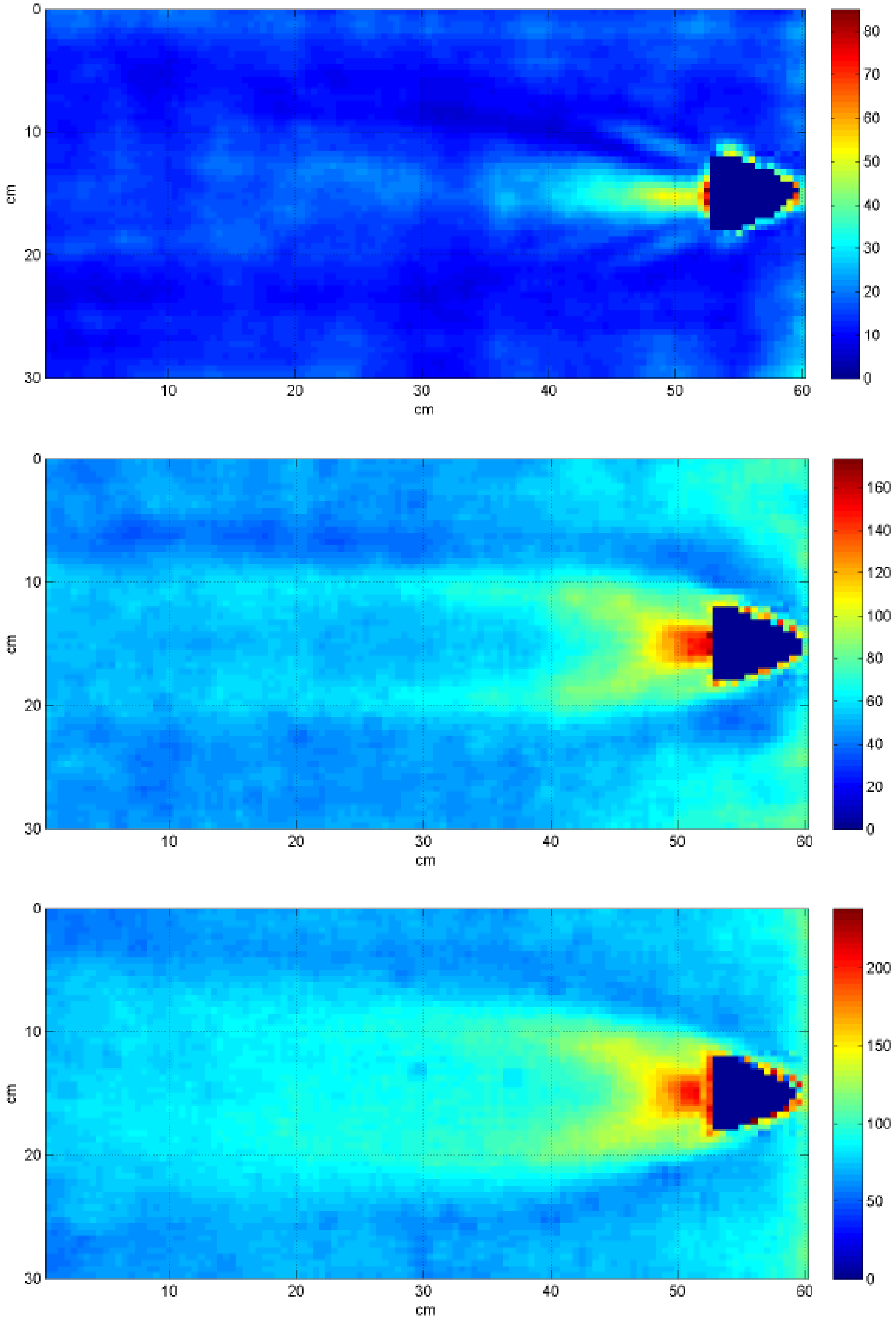

Figure 9.3: Heat transfer coefficients on the wind tunnel wall in the wake of the vortex generator for Reynolds numbers of 80,000 (upper), 300,000 (middle) and 450,000 (lower)

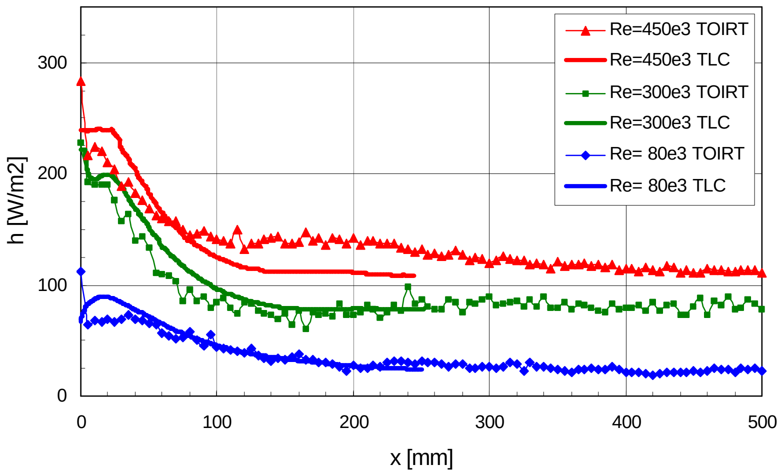

Figure 9.4: Comparison convection coefficients in the wake of a vortex generator measured with the TLC and TOIRT method

The second partner group at the Thermodynamics Institute of the Technical University of Braunschweig develops the Ammonia-Absorption-Method (AAM). This method gave relative values that are normed as unity for the convection coefficient in the unaffected air stream far behind the vortex generator. Figure 9.5 shows the data measured on the centerline with both methods for Re = 142000. Again very good agreement has been found.

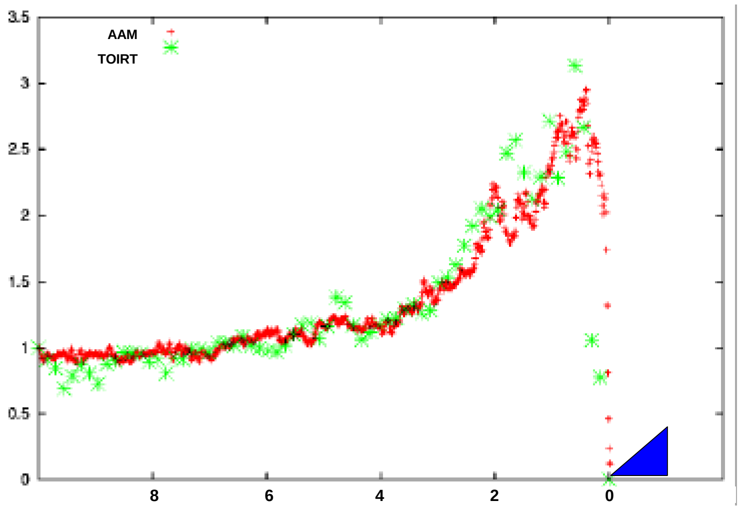

Figure 9.5: Comparison of relative convection coefficients in the wake of a vortex generator measured with the AAM and TOIRT method

The noise, the resolution and the deviation of the TOIRT data was much improved later after these first experiments due to better phase synchronization with square waves, enhanced convergence of the FDM algorithm and increased computing power, enabling to handle larger amounts of data.

The study on the vortex generator has proved the TOIRT well suited for the measurement of sizeable areas with low convection coefficients. The TOIRT gives the same results, but is much easier to employ than the two competing techniques. The TLC method requires surface heating with film heaters, exact knowledge of the actual surface heat flux and very time consuming temperature measurements with a camera viewing the inside surface of the channel. The image analysis system needs precise calibration to deduce the temperature from the color range. The AAM method relies on a chemical reaction between ammonia vapor in the air stream and an absorbent on the wall surface that changes the color depending on the level of absorbed ammonia. The determination of the heat transfer coefficients requires again an image analysis system that, to obtain absolute numbers, needs extensive calibration; exact chemical proportioning and reaction timing are also considerable experimental issues.

9.2 Vortex Generator Arrays

After the successful demonstration of the TOIRT measurements in the wind tunnel on the single vortex generator, two arrays of vortex generators were studied to investigate the interaction of multiple vortex generators in an arrangement that could be used in actual applications. The project was carried out again in close collaboration with the Institute for Aerospace Thermodynamics of the University of Stuttgart, who designed the vortex generator geometry and the array. The vortex generator used here is triangular with a length and width of 65 mm and a height of 26 mm, half as in the previous experiment. The first array is square with a grid spacing of 2.5 times the vortex generator's length; in the staggered array the spacing is the same but every other row is offset to the side by 1.25 times the length. The setup was similar as before but included some major improvements. To obtain uniform flow conditions in the test section, the airflow is drawn through a 50% open area grating 0.5 m before it, after passing a section split into multiple channels. Thus, we have hydrodynamic and thermal undeveloped flow within the test section, with higher heat transfer rates than found in fully developed internal flow; conditions similar to flow over the beginning of a flat plate. Progress in data processing allowed for a longer oscillation period of 40 s rather than the previously used 20 s, thus doubling the dimensionless heat transfer coefficient y (6.1). This reduces the sensitivity coefficient X from ca. 5 down to ca. 2.5 and thus significantly reduces the error due to phase delay uncertainties as the exponent is cut in half. Furthermore, these measurements were conducted using a Flir Phoenix camera with lower noise and higher temperature resolution. Rather than using halogen spotlights as a heat source, the wind tunnel wall was heated direct electrically, unlike any prior instances of TOIRT measurements. The direct electric heating eliminates problems associated with reflections from the hot halogen lights in the IR images, which can introduce errors in the phase delay data at long oscillation periods. Given a very large power supply able to deliver over 300 A, electric heating also provides a high amplitude of up to 4 K, reducing noise, and, because of a high slew rate, there is no need to account for an uncertain extra phase delay like for halogen lamps. These efforts reduced the standard deviation of the area-averaged convection coefficients of three consecutive measurements to ca. 2% (Re = 150000), 4% (Re = 300000) and 6% (Re = 450000). The spatial resolution could be reduced to 2.5 mm over an area of 680 x 340 mm^2, limited only by the camera's resolution.

The results for the square array are shown in Figure 9.7 for three Reynolds Numbers of 150000, 300000 and 450000. Similar features as those apparent from the previous experiment can be found: a heat transfer maximum in the downwash zone directly behind the vortex generator, although smaller due to the lesser height, a horseshoe vortex around the leading edge, and two distinct pairs of longitudinal vortices. Unlike before, an area of lower convection that follows the downwash zone can also be seen. The mentioned features persist through all studied Reynolds numbers, with their intensity increasing and the longitudinal vortices on each side merging. Stretched regions with low heat transfer coefficients in flow direction between the lines of vortex generators, apparently unaffected by the vortices, gave rise to the assumption that a staggered array may offer higher heat transfer. The results from the measurements on the staggered array are shown in Figure 9.8 for the same three Reynolds numbers. The long low heat transfer regions are now interrupted by vortex generators, but the minimum heat transfer area between the vortices that follows the downwash zone is more pronounced. Arithmetically area-averaged heat transfer coefficients are calculated for a “periodic”, i.e. presumably fully developed area of 325 x 325 mm^2 including four vortex generators from the 3rd and 4th row to provide a basis of comparison for the different arrangements. In Figure 9.6 these concluding numbers for the square inline array, the staggered array and a comparable plain wall section without the influence of vortex generators are compared. It is shown that an array of vortex generators enhances the heat transfer by a factor of ca. 1.5, with the square inline array surprisingly outperforming the staggered array by 3 – 5 %. Assuming further that a staggered array leads to higher pressure losses than an inline array, the arrangement of choice for such vortex generators is a square array, improving the heat transfer performance by about 50 % over a plain wall.

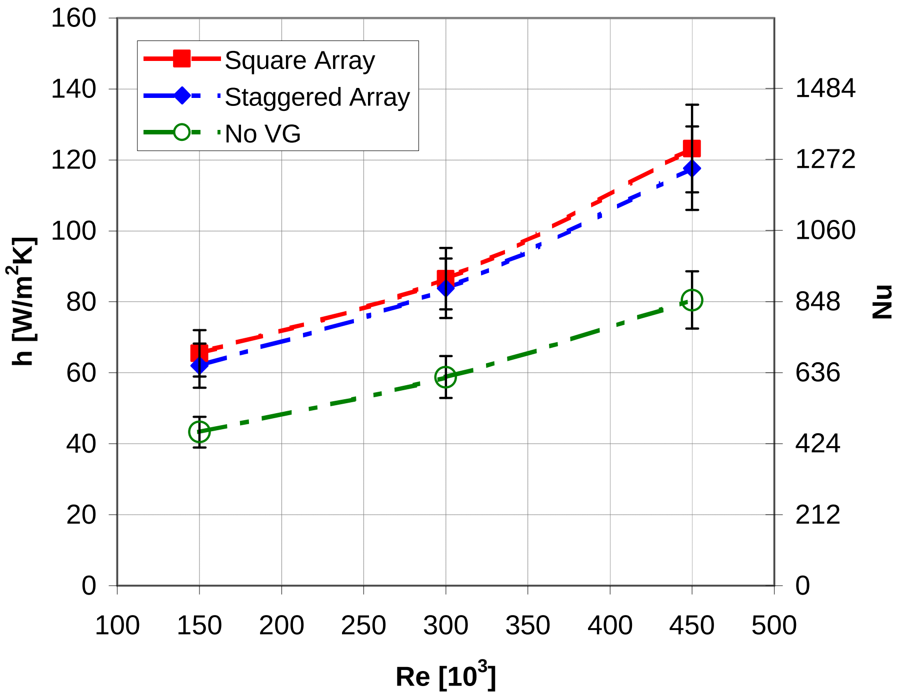

Figure 9.6: Comparison of the arithmetically averaged convection coefficients on an area comprising the last four VG’s and the plain channel without VG influence, respectively.

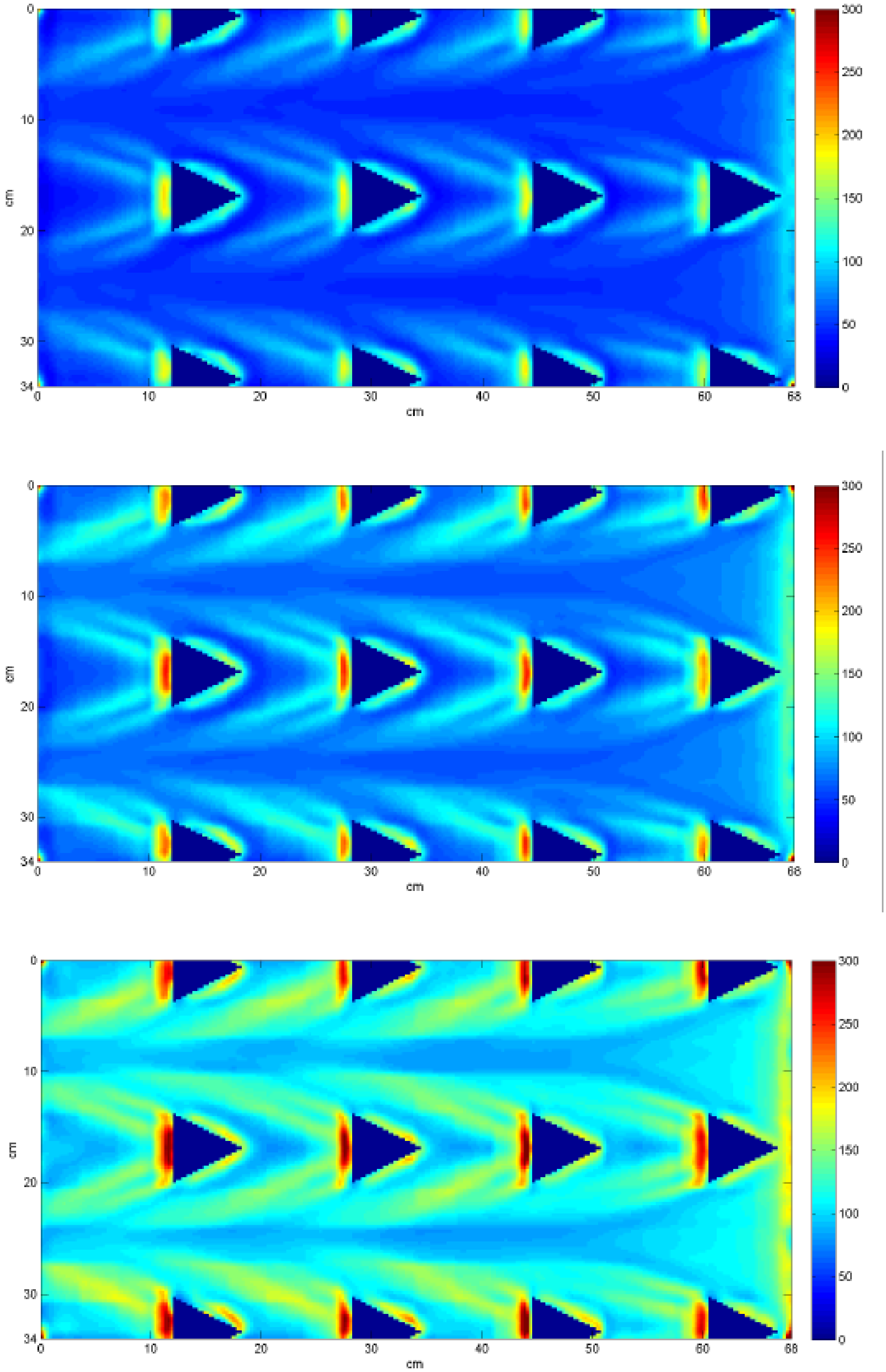

Figure 9.7: Heat transfer coefficients around a square array of VG's for Re = 150000 (upper), Re = 300000 (middle) and Re = 450000 (lower).

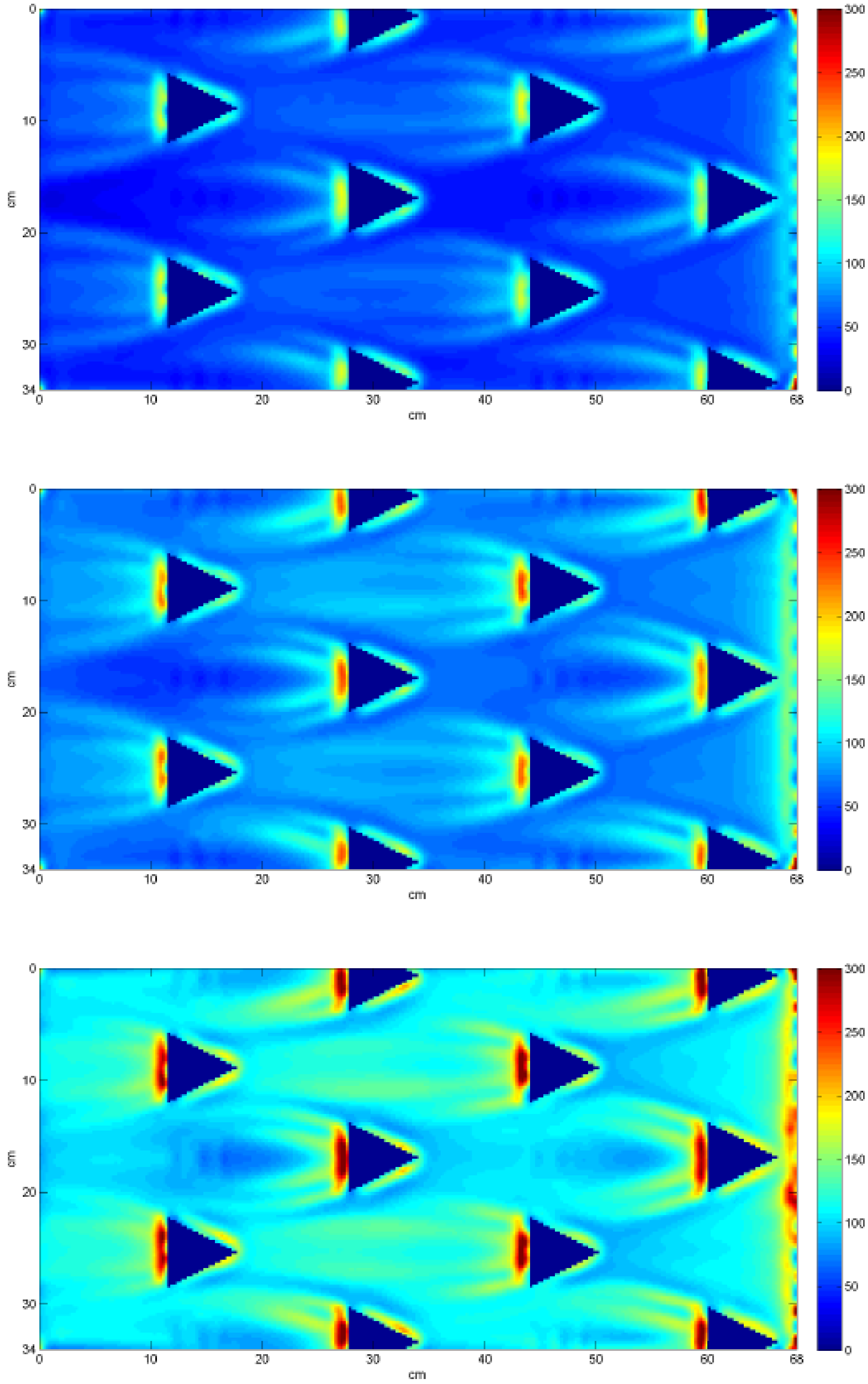

Figure 9.8: Heat transfer coefficients around a staggered array of VG’s for Re = 150000 (upper), Re = 300000 (middle) and Re = 450000 (lower).

In Figure 9.10 and Figure 9.11, the arithmetically averaged heat transfer coefficients over the width of a “periodic” section including two vortex generators are plotted as a function of the length in flow direction, for the square inline and the staggered array, respectively. The present results from the TOIRT method are compared here to the results from Henze et al. [2007] at the University of Stuttgart, who used a transient TLC technique in which step changes of the fluid temperature were imposed to find the heat transfer coefficients on equal arrays at the same Reynolds numbers. The respective curves for both arrays show the same characteristics, a peak right behind the vortex generator from the downwash zone followed by a decline and a hump caused by the horseshoe vortices at the second vortex generator. However, the data sets from the different experiments and measurement methods seem to be somewhat offset, with the present data up to 20% higher than the TLC data for the lower Reynolds number. The differences in the data for the inline array are somewhat less than for the staggered array; the decline of the TOIRT curves in flow direction, especially for the staggered array data, indicates that fully developed conditions are not attained. The wind tunnel used for the measurements with the TLC method had a test section with a hydraulic entrance length of 2 m and an array with nearly twice the number of rows, resulting in a further developed boundary layer with lower near-wall velocities. This explanation is backed by the fact that the differences of both experiments are larger at lower Reynolds numbers, where the boundary layer is thicker and entrance effects are stronger, and by the decrease of the differences with the flow development in flow direction.

A subset of the data from Henze et al. [2007] for the inline array at *Re* = 450000 is shown in Figure 9.9 in comparison to the same area measured with the TOIRT and a CFD simulation from Dietz et al. [2007] using a Reynolds Stress turbulence model. This image (courtesy: Dietz) illustrates how well both measurement methods resolve the characteristic flow features and arrive at very similar results. The CFD values, however, do not show the same distribution of the convection coefficients enhanced by the double vortex, but a smoother distribution. The averaged CFD values are nonetheless similar to the measurements. CFD modeling with these advanced Reynolds Stress models will be further elucidated in chapter 12 on plate heat exchangers.

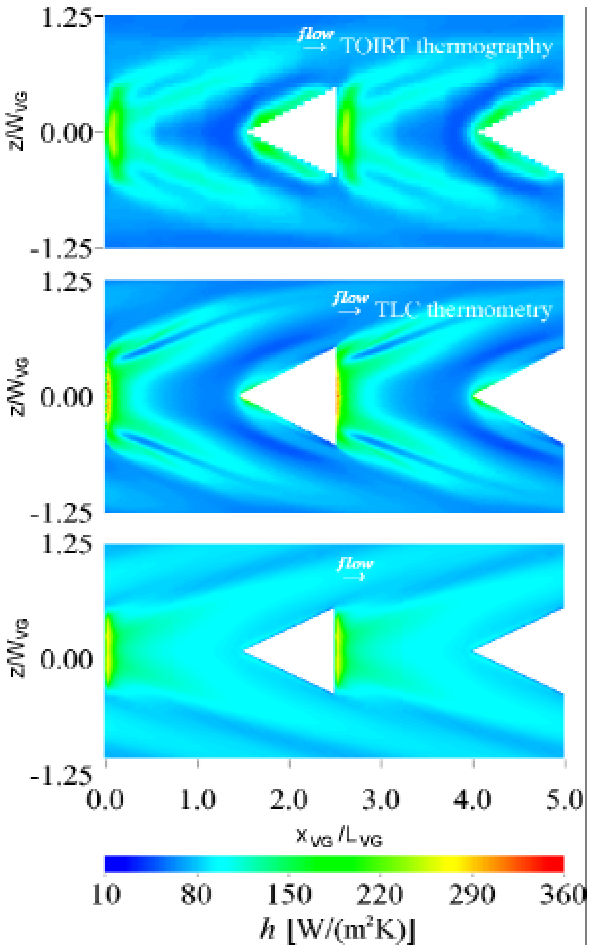

Figure 9.9: Comparison of *h* measured with TOIRT (upper), TLC (middle) and simulated with CFD – RSM (lower) at *Re* = 450000.

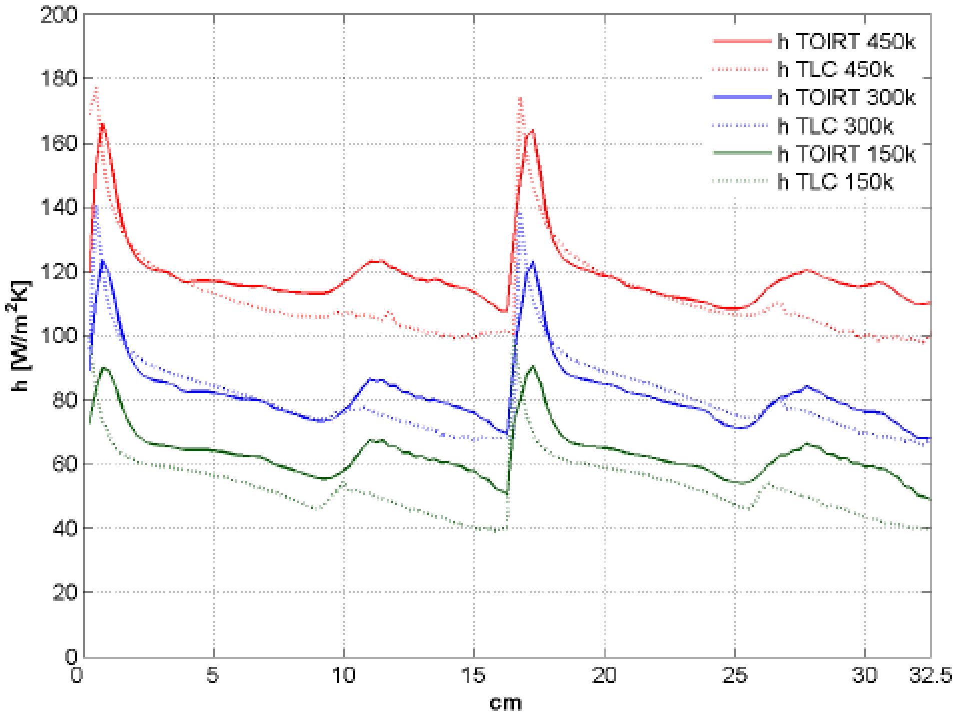

Figure 9.10: Channel width averaged heat transfer coefficients in flow direction over the length of two vortex generators in a square array, measured with TOIRT and a TLC method at three Reynolds numbers.

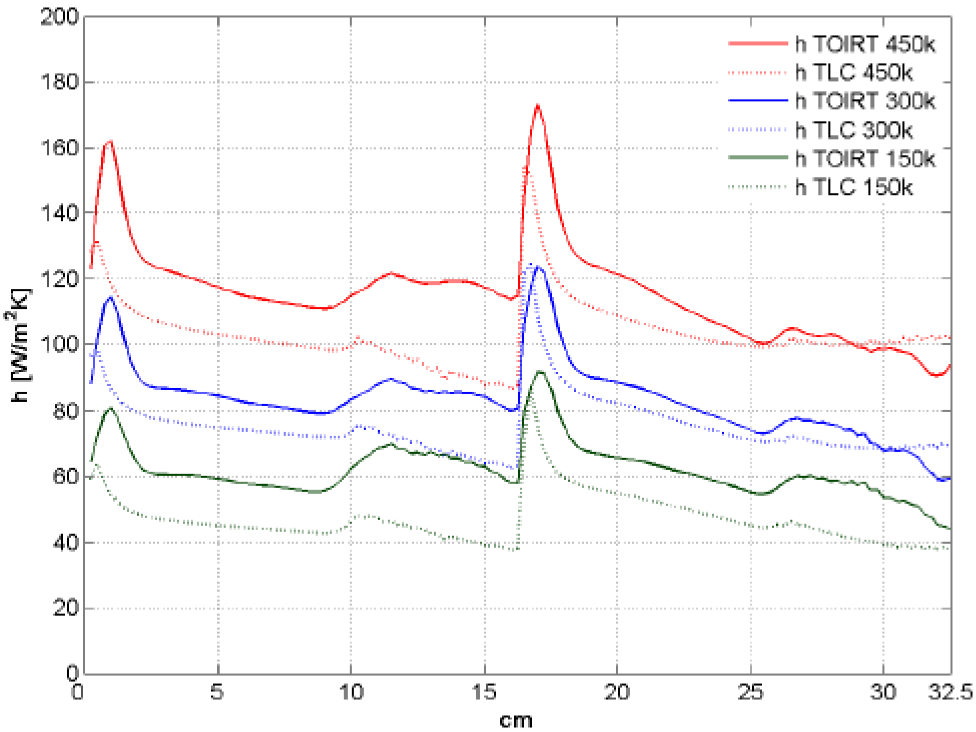

Figure 9.11: Channel width averaged heat transfer coefficients in flow direction over the length of two vortex generators in a staggered array, measured with TOIRT and a TLC method at three Reynolds numbers.

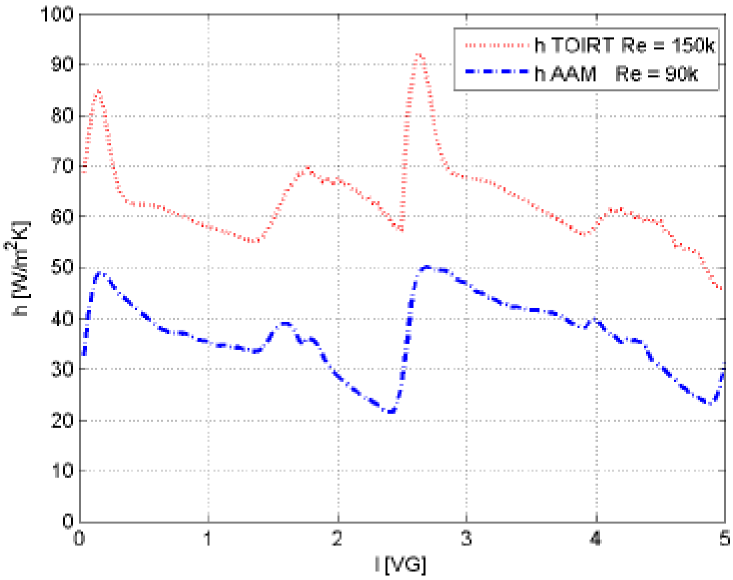

Figure 9.12: Laterally averaged heat transfer coefficients in flow direction over the length of two vortex generators in a staggered array, measured with TOIRT and AAM method at two different Reynolds numbers.

The collaborating researchers Ahrend et al. [2007] at the Technical University of Braunschweig use the AAM in a smaller channel with much smaller vortex generators, although with the same geometry. A comparison of their data from a periodic area with the TOIRT results is shown in Figure 9.12 as a function of the length in flow direction normalized by the length of the vortex generator. Extrapolating the TOIRT values down to the Reynolds number of the AAM gives approximately the same average values. The profile has a very similar shape, however, the peak in the downwash region is disproportional less significant, probably due to the smaller size of the vortex generators and lower Reynolds number.

The collaborative study of the heat transfer enhancement of vortex generators has shown details of the distribution of the convection coefficients and the flow field. Furthermore, this study has shown through direct comparison of the three different measurement techniques, that these give equivalent and therefore valid and reliable results.

10 Impinging Jets

Impinging Jets are free fluid streams that impinge onto a solid surface. Such jets provide very high local heat and mass transfer rates and are used in a wide range of applications for industrial processes such as cooling or heating, drying or moisturizing. Examples include cooling of products during manufacturing from plastic to food, steel annealing, drying of textiles or paper and spray cooling of machine tools. Recently developed applications of impinging jets include cooling of turbine engine components and power electronics.

As a demonstration of the TOIRT capabilities, the local convective heat transfer coefficients surrounding an impinging jet of air were investigated. The temperature oscillation IR thermography turned out to be very well suited for this application because of its specific advantages of high spatial resolution, and that only optical access on the backside is needed and no flow interaction with the jet occurs. The air jet impinges perpendicular onto a 0.5 mm sheet of stainless steel. The backside of the steel plate is coated with black spray paint and is heated with a 15 W diode laser, modulated with a frequency of 0.1 Hz; an Agema 900 scanner records the surface temperatures. The nozzle diameter is 2 mm and nozzle outlet velocity is the speed of sound, ca. 336 m/s. The Reynolds number based on the nozzle diameter *d* is ca. 47000. The distance z from the nozzle to the surface is varied from 5 to 20 mm. The following Figure 10.2 to Figure 10.7 map the heat transfer coefficients over the evaluated area and plot the circumferentially averaged convection coefficients over the radius from the center of the jet.

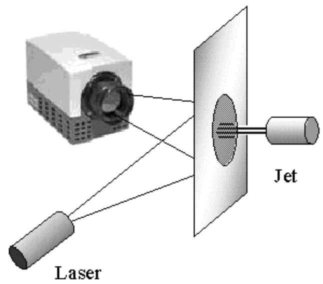

Figure 10.1: Schematic of the experimental setup.

Although experimental data is available form literature, it proved difficult to directly compare the numbers due to very different experimental approaches. Martin [1977] measured the heat transfer coefficient using the mass transfer analogy. The amount of water evaporated per time in a section of the area under the jet is related to the convection coefficient. The results of Martin are also illustrated in the plots of the heat transfer coefficients as a function of the radius; they appear to be lower than the present measurements. Carlomagno, Astarita and Cardano [2002] investigated the heat transfer surrounding an impinging jet of air with the heated thin foil technique and IR thermography. The convection coefficients are calculated from the known heat flux of the heating foils glued to the surface, the previously measured adiabatic wall temperature and the surface temperatures of the steadily heated foils. They also used an Agema 900 IR scanner. Their results show that two radial maxima and minima appear around the stagnation point for high Reynolds numbers and small ratios of the impingement distance to the nozzle diameter. One minimum is at the stagnation point, the other at r/d = 1.4. The maxima are located at r/d = 0.8 and 2.4. For lower Reynolds numbers, these extrema flatten out and for larger distances they move outwards, decrease and give way to a single maximum at the stagnation point. PIV measurements reveal the streamline field with concentric vortex rings. Separation and reattachment of the flow in the shear layer caused by the vortices explains the second minimum and maximum. The qualitative observations from Carlomagno et al. coincide with the current experimental results. However, absolute values could not be compared accurately since the experimental conditions are different and certain properties remain unknown.

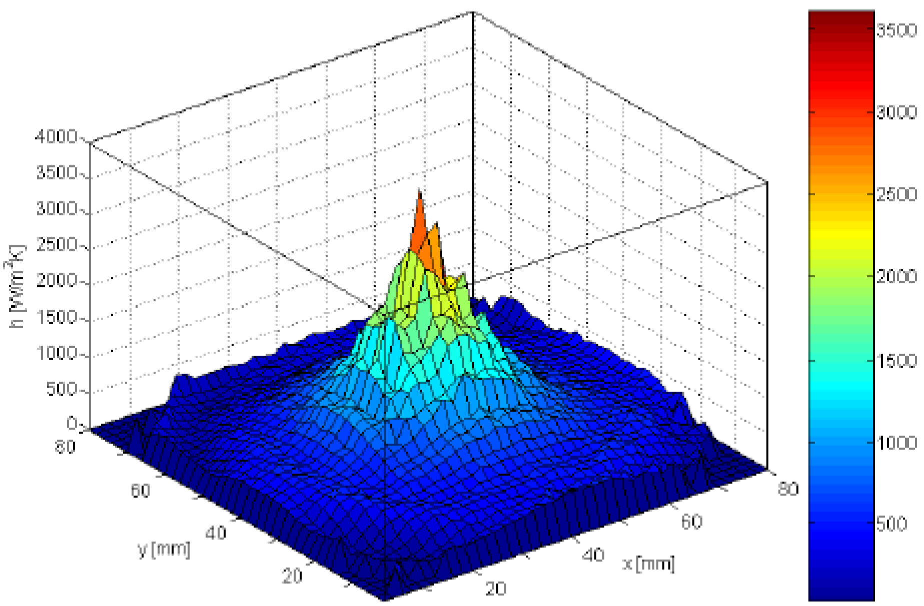

Figure 10.2: Heat transfer coefficients around an impinging jet of sonic speed air with 2 mm round nozzle at 20 mm distance.

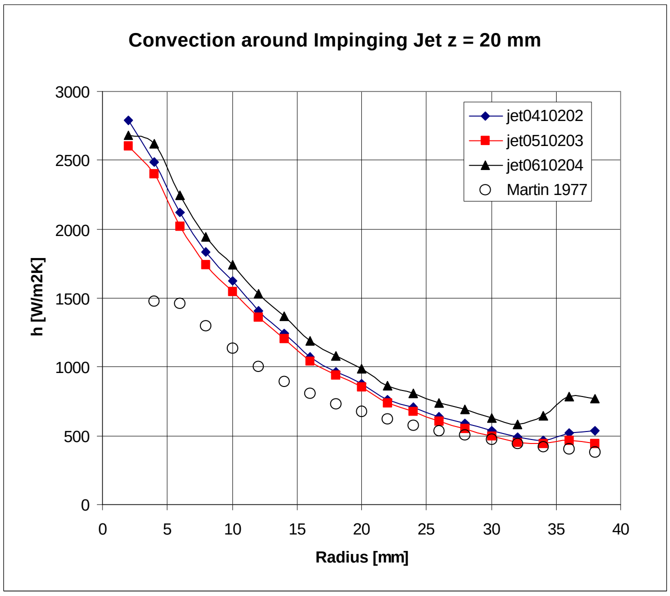

Figure 10.3: Circumferentially averaged heat transfer coefficients compared for the three measurement runs and literature values.

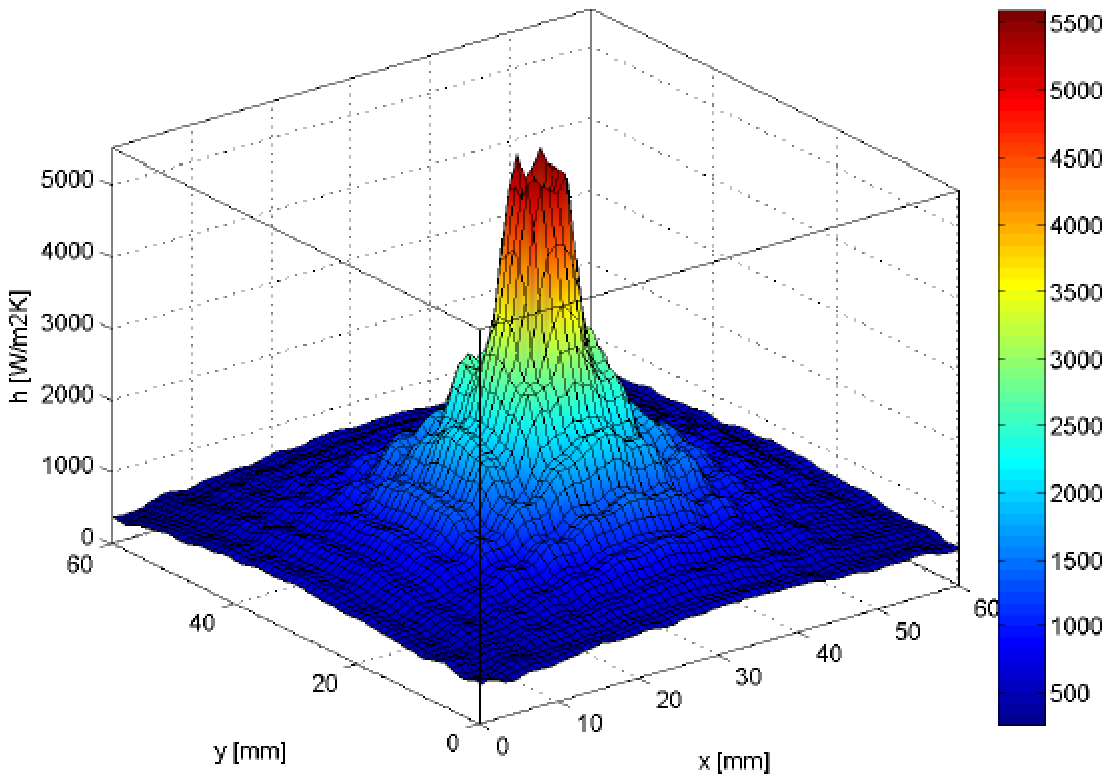

Figure 10.4: Heat transfer coefficients around an impinging jet of sonic speed air with 2 mm round nozzle at 10 mm distance.

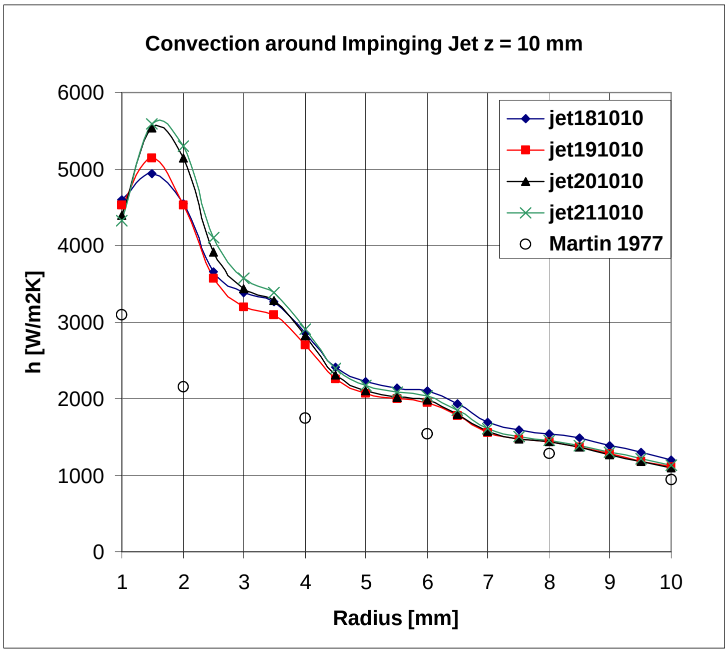

Figure 10.5: Circumferentially averaged heat transfer coefficients compared for the three measurement runs and literature values.

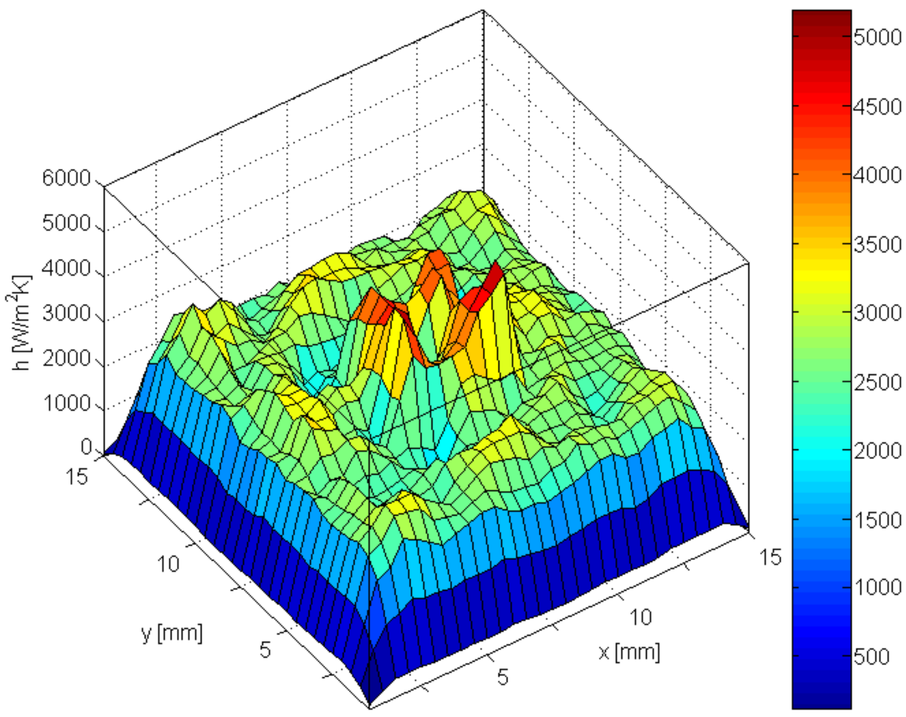

Figure 10.6: Heat transfer coefficients around an impinging jet of sonic speed air with 2 mm round nozzle at 5 mm distance.

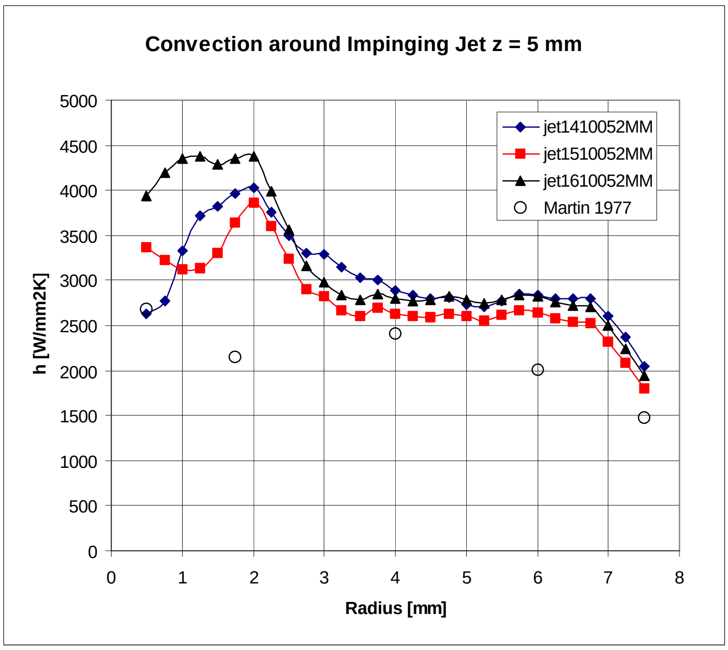

Figure 10.7: Circumferentially averaged heat transfer coefficients compared for the three measurement runs and literature values.

11 Spray Cooling

This project to measure the performance of spray cooling systems with the TOIRT method has been carried out in collaboration with the Multi-Phase Flow Visualization and Analysis Lab of the University of Wisconsin – Madison, namely Prof. Tim Shedd and Adam Pautsch, who have considerable experience in spray cooling systems. The results presented in this chapter have been published by Freund, Pautsch, Shedd and Kabelac [2006].

11.1 Introduction

As technology progresses, the power densities of electronic packages have continued to rise beyond the limits of conventional cooling. More sophisticated techniques to remove heat from the devices have been implemented, but many of these require a thermal interface material that adds a substantial amount of thermal resistance at high heat loads. Spray cooling is one method of direct liquid cooling that eliminates the need for a thermal interface material. When an inert fluid such as perfluorohexane (Fluorinert™ FC-72) like in this study is used, there is no risk to the electronic device from electrical arc or hydrogen diffusion. This direct cooling approach reduces the thermal resistance and leads to lower surface temperatures compared to any indirect system such as cold plates. Other benefits of spray cooling include improved thermal management, dense system packaging, and reduced weight of high heat flux computer chips, power electronics, and laser diode arrays.

The performance of conical sprays has been characterized by several research groups among them Horacek, Kiger and Kim [2005], Lin and Ponnappan [2004] and Mudawar and Estes [1996]. Cotler et al. [2004] reported a heat flux of up to 162 W/cm^2 using a spray cooling system for an RF power amplifier with water as the working fluid. There have also been numerous numerical simulations designed to model the interactions of droplets on a superheated surface and the corresponding heat transfer coefficients. Croce et al. [2002] have successfully modeled heat extraction from a surface by evaporation of impinging droplets. Lee et al. [2001] have also modeled droplet interaction with a superheated surface and report heat transfer coefficients of between 0.1 and 2.0 W/cm^{2}K in their simulations of an engine cylinder. The two most commonly reported performance metrics for spray cooling systems are the critical heat flux (CHF) and the heat transfer coefficient *h*. The CHF is an upper limit on the power level that can be removed from a system while the heat transfer coefficient dictates the device temperature for a given heat load. Traditionally, the spray cooling heat transfer coefficient has been defined according to

$$h = \frac{q}{T_{surface} - T_{inlet}} \quad , \tag{11.1}$$

where T_{inlet} is the fluid temperature at the inlet of the spray nozzle. The applied heat flux q is typically assumed to be uniform over the surface and $T_{surface}$ is measured at discrete locations on the device. The surface temperature is typically measured in two ways, depending on the heating element. If cartridge heaters in a copper block are used, then multiple thermocouples placed along the conduction path are used to extrapolate the temperature to the surface. This single temperature measurement is typically obtained at the center of the heater, which in most cases is located directly under the center of the spray where the heat transfer coefficient is the largest. This may lead to a reported heat transfer coefficient that is substantially higher than the average surface heat transfer coefficient; further study is needed, however, to support this assertion. When thermal test dies are used, the junction temperature measured at the active layer of the silicon is assumed to equal the surface temperature [Pautsch and Shedd 2005]. Multiple junction temperature measurements allow for the estimation of the heat transfer coefficient at different regions of the spray, but it is not possible to obtain a detailed surface map using this method. Conventional methods are limited when data from the heat transfer surface with higher spatial resolution is desired. Researchers at the University of Maryland use a dense array of individually controlled heaters. Each of the 96 heaters in the array is sized 700 x 700 μm^2 and is controlled by a Wheatstone bridge [Horacek, Kiger and Kim, 2005]. The individual heating elements allow for temperature and power measurements at a fairly high spatial resolution with an uncertainty of 5%. As an added benefit, these heaters may be operated in constant heat flux or constant temperature modes, allowing these researchers to study the behavior of boiling and spray impingement past the peak heat flux temperature difference. Thermochromic liquid crystals (TLC's) have also been used to obtain high resolution measurements of temperatures. Dano et al. [2005] investigated the local heat transfer coefficients under an array of air jets with crossflow on an area of 49 cm^2 using a CCD camera with 640 × 480 pixel resolution and a transparent orifice plate to view the impingement surface. They report local heat transfer coefficients of a center section of the array with peak values of 800 W/m^2K and average Nusselt numbers with an uncertainty of 4%. Schmidt and Boye [2001] derived heat transfer characteristics of high-temperature spray cooling on a thin electrically heated metal sheet with IR thermography. Average heat transfer coefficients are reported for various flow parameters and temperatures with an uncertainty of the calibrated measurement setup of 6%. Thus, some heat transfer coefficients of spray cooling and other high heat flux systems have been measured with high resolution and accuracy. Unfortunately, these methods are challenging to implement since, in order to obtain truly local heat transfer coefficients, the surface heat flux and local fluid temperature must be known exactly. The TOIRT method, as it turns out, is very well suited to measure local heat transfer coefficients at spray cooling systems with high spatial resolution.

Multiple nozzle arrays are required when large surface areas are to be cooled using sprays [G. Pautsch, 2001]. Previously reported visualization of multiple nozzle arrays has shown that the resulting fluid flow behavior is very complex [Shedd and Pautsch, 2005]. When nozzles in close proximity generate a conical spray, droplets will collide and interfere between adjacent nozzles causing a flow stagnation zone. In this zone, the velocity of the liquid is significantly reduced, resulting in lower heat transfer coefficients and higher surface temperatures, even though the rate of fluid delivery is higher. Larger surfaces require more nozzles, which in turn leads to more complex draining and more local stagnation regions. To better design nozzle arrays and draining systems, a full surface map of the local heat transfer coefficients is desired. With this information, systems can be designed to achieve more uniform cooling across the active surface and each device on a multi-chip module (MCM) or other large area can be assured of equal cooling.

In this study, the TOIRT method was used to characterize two spray cooling designs. A 1.5×1.5 cm^2 area was investigated, and local values for the heat transfer coefficient were found with a resolution of 0.4 mm. The results are compared to a previous experiment that used the conventional method to measure the heat transfer coefficients for the same nozzles at the same flow rates with a thermal test die.

11.2 Experimental Setup

The spray cooling system considered in this study is commercially used for spray cooling of multi-chip modules (MCM) in the CRAY X1 (formally known as the SV2) supercomputer, with desired junction temperatures of 70 to 85°C for heat fluxes from 15 to 55 W/cm^2 with a Fluorinert™ coolant. Details of the system are described by G. Pautsch [2001] as well as by Pautsch [2004].

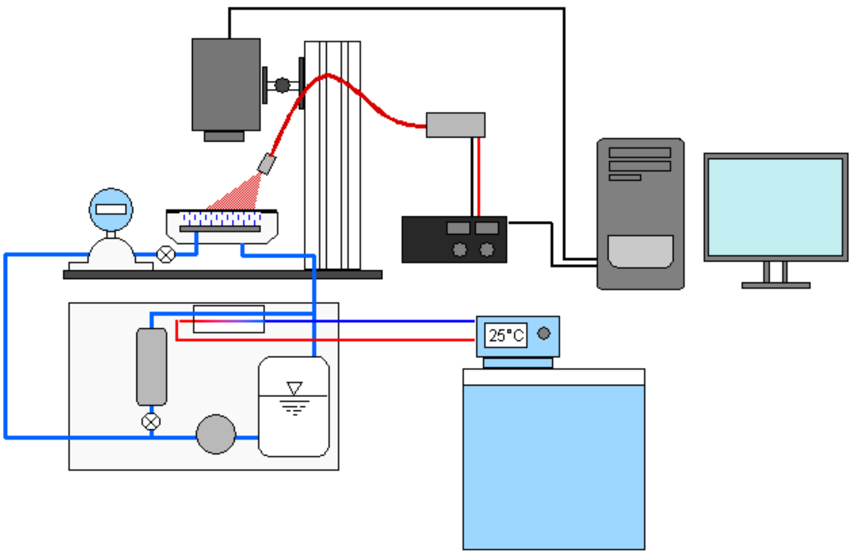

Figure 11.1: Schematic of the experimental setup.

Figure 11.1 displays a schematic of the experimental setup, with the spray cooling module in the center, the heat source and the camera above, and support devices in the periphery. The IR camera used is a FLIR ThermaCAM SC500 that records 30 frames per second with a 320×240 resolution. The heat source is a fiber-coupled diode laser with 12 W peak optical power at 685 nm, square wave modulated at a frequency of 0.25 Hz. The laser spot size on the surface is varied according to the size of the evaluated area; the time averaged heat flux is approximately 1.5 W/cm^2. A PC with an IRFlashLink® PCI card and IRLockIn® software records the frames and controls the laser via a programmable Sorenson DC current source. The heat transfer surface was made of ASTM 316 stainless steel coated with black paint (e = 0.95) on the outside for better absorption (total wall thickness 0.272 mm). A variable speed magnetically coupled Idex Corp. MicroPump gear pump is used to deliver the fluid. A needle valve is used to adjust the amount of flow delivered to the nozzles. The volumetric flow rate and fluid inlet temperature are measured with a Krohne Optimass 3050C coriolis flowmeter. The measurements were taken at three different total flow rates of 0.667, 1.00, and 1.50 l/min, held to within 1%. The fluid inlet temperature was maintained at 25°C by a thermostatic circulating water bath and a FlatPlate liquid-to-liquid heat exchanger. The fluid is subcooled and no boiling or significant evaporation occurs at the level of heat flux that was applied. The spray nozzle plate used for testing contains eight sets of nozzles designed to cool the MCM. As shown in Figure 11.2, there are four four-nozzle arrays (design B) and four single-nozzle arrays (design A) that have been described in detail by Pautsch and Shedd [2005]. The nozzles spray vertically upwards directly onto the stainless steel plate with a spacing of 5 mm between the nozzles and the heated plate. Nozzle design A is an array of four nozzles cooling a single die, while nozzle design B is a single nozzle. The area of coverage for each nozzle set is designed to be 15 × 15 mm^2. The drain of the cap is located beneath the center of the MCM. Figure 11.2 also shows the relative location and size of the nozzles with respect to the area that it is covering.

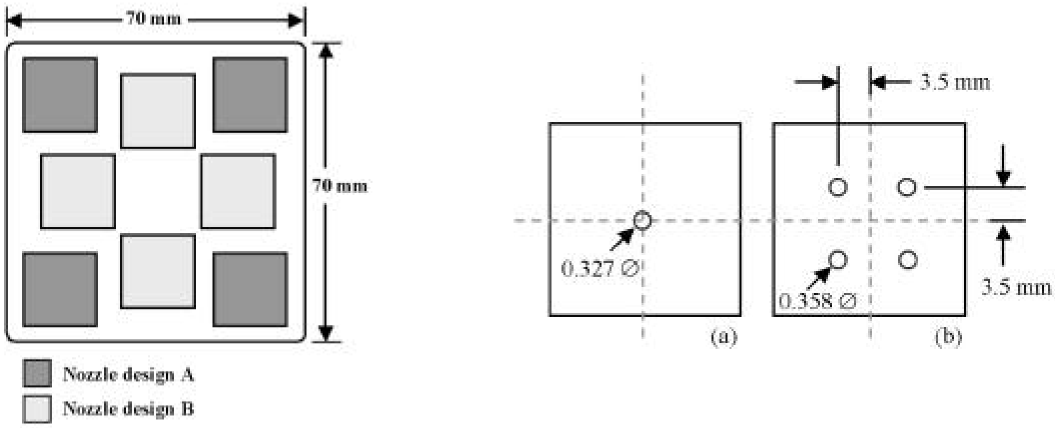

Figure 11.2: Relative locations of the nozzle arrays and nozzle geometry.

Two field of view sizes were chosen for testing: 4.7 × 7.0 cm or 2.1 × 3.2 cm, corresponding to 0.20 W/cm^2 and 1.5 W/cm^2. The magnitude of the temperature oscillation varied because of the local variation in the applied heat and the convection, ranging from 1 - 4 K peak-to-peak. The applied heat fluxes are within the so-called single-phase spray cooling regime, so no heat flux-dependent heat transfer behavior is expected.

Experiments were performed where the entire spray cap was imaged, as well as experiments concentrating on a single nozzle and a four nozzle array. Because a fixed focus optical system was utilized, the field of view was constrained by the available lenses. After the numerical model was run to calculate the local heat transfer coefficients, the resulting data arrays were cropped to rectangular regions representing the areas that the nozzle sets were designed to cool. The cropping also eliminates noise at the edges of the data arrays due to numerical edge effects.

To estimate measurements errors, an uncertainty analysis according to Chapter 6 is carried out, in which the accuracy of the computed heat transfer coefficients based on the uncertainty of the measured phase delay and the wall parameters is considered. For a measurement with a frequency of 0.25 Hz and 30 frames per second over five periods, the

RMS of the phase delay error is 0.0144 at an SNR of 4. The standard deviation of the extrema phase angle is less than half of the time delay between frames. Thus, a maximum phase synchronization error of 1/2 of the frame time step is assumed, which is 0.0262 rad at 30 frames per second. For local phase values $f(x, y)$, the sum of both errors must be considered, while for average values, the synchronization error dominates. Table 11.1 shows the results of an uncertainty propagation of the input errors through the calculation of the heat transfer, further assuming an uncertainty of 5% in the material properties and ± 2.5 μm in the wall thickness. The values summarized in Table 11.1 are the maximum expected errors associated with a single measurement. The results presented here are each an average of four single measurements, effectively reducing the errors by a factor of two; therefore the uncertainties are conservatively stated < 5% for the average values and for local values, depending on the magnitude, between 5% and 10%.

Table 11.1 Uncertainty propagation for single measurements.

Local Dh/h	Average Dh/h	h	SNR
10.8%	6.6%	0.4 $Wcm^{-2} K^{-1}$	4
20.8%	14%	0.8 $Wcm^{-2} K^{-1}$	2

11.3 Results

Measured heat transfer coefficients are presented here for the whole MCM cooling module as well as for the four-nozzle array and the single nozzle individually, enlarged to show measurements that are more detailed. The flow rates through the entire nozzle array (20 nozzles) are 0.67, 1.0 and 1.5 l/min, respectively, with a corresponding pressure drop through the nozzles of 69.0, 138, and 310 kPa. The droplet flux rates of the individual nozzles or nozzle arrays are estimated based on the design conditions from the manufacturer and are divided by the area to be cooled.

11.3.1 Full Nozzle Array

Figure 11.4 a) to c) illustrate maps of the heat transfer coefficients measured on a 60×44 mm^2 section of the plate with a resolution of 0.8 mm^2 for the three flow rates. The entire spray coverage area shown in Figure 11.2 could not be captured in the camera field of view; the upper two single-nozzle arrays are not visible, as well as half of the upper four-nozzle array. The figures show areas of high heat removal above the spray nozzles and low heat transfer coefficients between them. The peak values increase from 1.2 to 2.0 W/cm^2K. The heat transfer coefficient surrounding the nozzles is remarkably uneven, with some nozzles performing significantly worse than others. The performance is affected by both, the nozzle spray patterns and the local fluid flow, making uniform draining an important issue. These wide field of view images are intended to show the variation between the nozzle arrays due to spray distribution and liquid interaction on the surface.

11.3.2 Four Nozzle Array

In Figure 11.5 a) to c), the heat transfer coefficients on a 1.5 x 1.5 cm^2 area above a four-nozzle array (nozzle design B) are shown with a resolution of 0.4 mm2 for droplet fluxes of a) 1.00, b) 1.50 and c) 2.25 mls^{-1}cm^{-2}. The peak values increase from 1.3 to 2 W/cm^{2}K as flow increases. The heat transfer coefficients associated with the upper left nozzle were lower than for the other nozzles, apparently due to nozzle imperfections, which will be discussed further below.

11.3.3 Single Nozzle

The heat transfer coefficients on a 1.5 × 1.5 cm^2 area above a single nozzle (nozzle design A) are shown in Figure 11.6 a) to c) for flow rates of a) 0.234, b) 0.352 and c) 0.528 mls^{-1}cm^{-2} with a resolution of 0.4 mm. The peak values directly above the nozzle increase from 1 to 1.5 W/cm^{2}K as flow increases. The heat removal is high directly above the spray, but as the fluid moves out radially along the surface, the momentum of the fluid is lost and the heat transfer coefficient decreases. This pattern matches the results obtained by Pautsch and Shedd [2005], who found the highest performance of this nozzle design to be at the center with the lowest performance at the corners. Circumferentially averaged heat transfer coefficients as a function of the radial distance from the single nozzle are plotted in Figure 11.3. As noted above, Horacek et al. [2005] used an array of 0.7 × 0.7 mm^2 heaters to obtain information on local spray heat transfer behavior. Although they do not present heat transfer coefficient data, they may be inferred from data in Horacek, Kim and Kiger [2003] and their spatial trends correspond closely to those presented here.

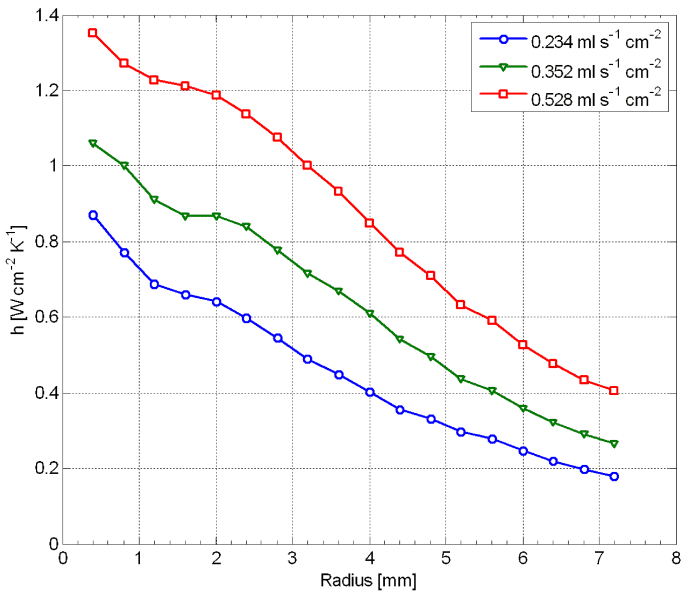

Figure 11.3: Circumferentially averaged convection coefficients over the radial distance from a single spray nozzle.

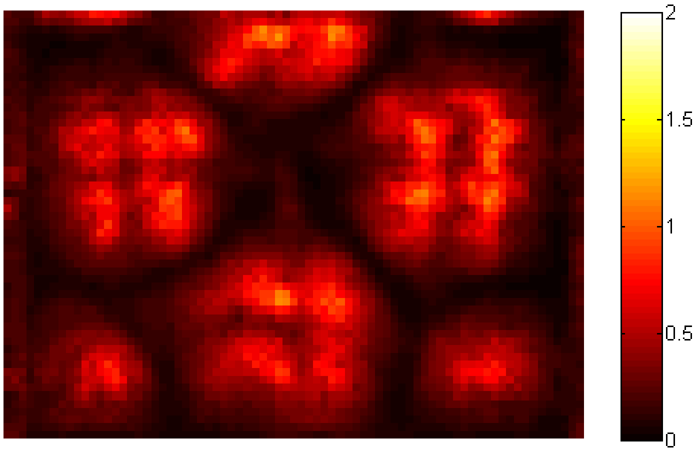

a)

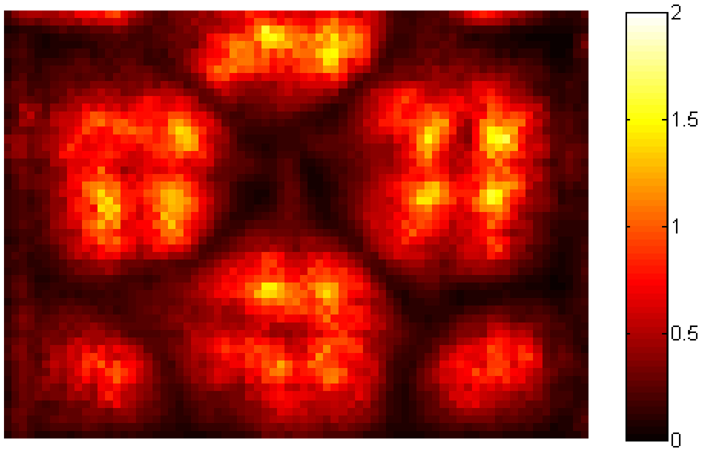

b)

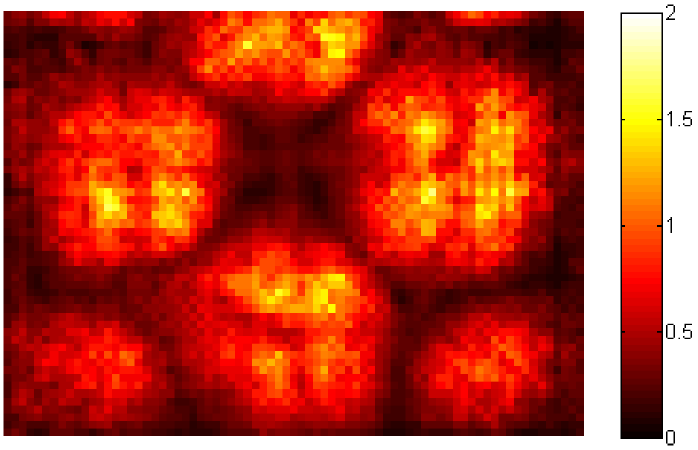

c)

Figure 11.4: Convection coefficients in $Wcm^{-2}K^{-1}$ on MCM for a) 0.67, b) 1.0 and c) 1.5 l/min.

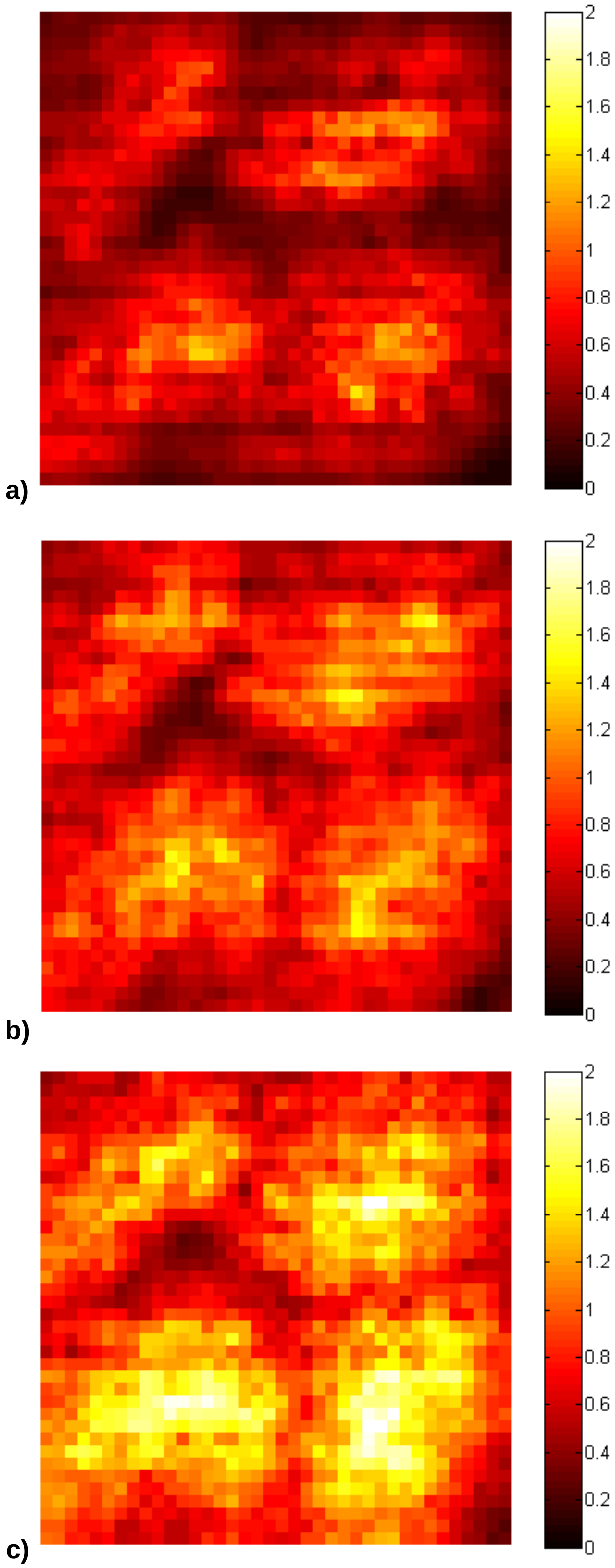

Figure 11.5: Convection coefficients above a four-nozzle array in W/cm^{2}K for a) 1.0, b) 1.5, and c) 1.5 mls^{-1}cm^{-2}.

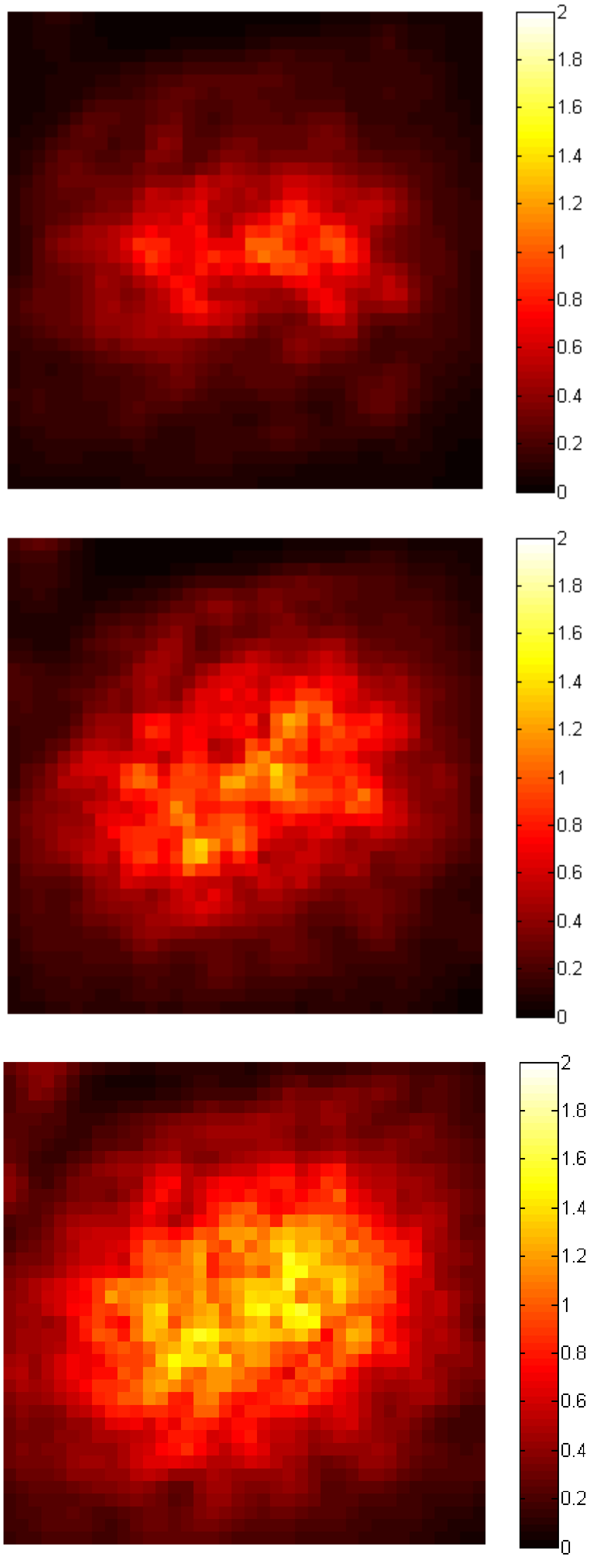

Figure 11.6: Convection coefficients above single nozzle in W/cm2K for a) 0.234, b) 0.352 and c) 0.528 mls1cm2.

11.3.4 Spatially Averaged Results

The arithmetically averaged heat transfer coefficients for the single- and four-nozzle arrays over the cooling area are listed in Table 11.2. These area-averaged values indicate an almost linear increase of the heat transfer coefficients with the flowrate. The comparison of the two arrays shows that the four-nozzle array has about twice the performance of the single nozzle but at four times the flowrate. The current heat transfer coefficient measurements taken with the TOIRT method are in Table 11.2 also compared to measurements taken with the conventional method. In that previous experiment, thermal test dies with eight embedded temperature sensing diodes were used to obtain an average heat transfer coefficient with varying flow rates and heat fluxes [Pautsch and Shedd, 2005]. The coefficients from these data are an estimate based on the lowest applied heat flux, since the heat transfer coefficient becomes heat flux dependent at high heat fluxes and the TOIRT method used a low power heat source.

Table 11.2: Arithmetic area average heat transfer coefficients for a 1.5 x 1.5 cm^2 area for the single- and four-nozzle array and comparison of the TOIRT method with prior data derived with the discrete method for similar flow rates and applied heat fluxes.

Flowrate	h TOIRT	h prior
ml s^{-1}cm^{-2}	W/cm^{2}K	W/cm^{2}K
Single-Nozzle Array		
0.234	0.251	0.20
0.352	0.368	0.30
0.528	0.541	0.45
Four-Nozzle Array		
1.000	0.547	0.60
1.500	0.759	0.80
2.250	1.015	1.10

Table 11.2 shows agreement in the measurements of the heat transfer coefficients between the conventional and the TOIRT method of 25% or better for the single nozzle and within 10% for the four-nozzle array. For the multiple nozzle array, the TOIRT values are always slightly lower than the values from prior measurements. This is likely because the TOIRT method is able to measure the values of heat transfer coefficient in the interference regions of the die, where they are at their lowest. Since there were no thermal diodes located in the spray interference region on the MCM thermal test dies, the conventional method does not include those lower-performing regions in its average. For the single nozzles, the TOIRT method found higher heat transfer values than the prior measurements with the conventional method. An explanation for this is that the previous measurement was more heavily averaged to the outside of the die where most of the thermal diodes were located: only one value was measured at the center, the other values were measured at the edge or outside the spray region, leading to a lower reported heat transfer coefficient.

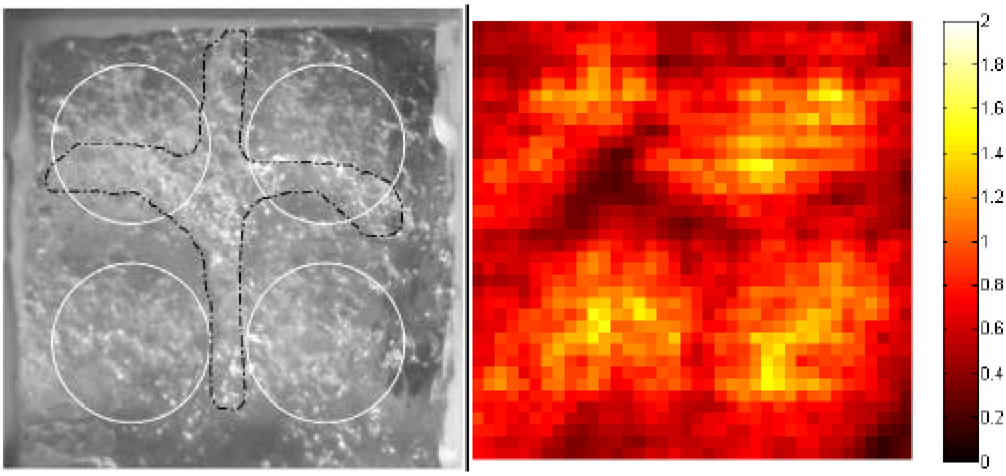

Figure 11.7: Visualization of a typical four-nozzle array and the measured heat transfer coefficients.

In a previous study, it was theorized that the heat transfer performance of multi-nozzle arrays in spray cooling systems can be correlated by three terms: Sensible heating of the liquid beneath the spray impingement area, latent heat of vaporization due to evaporation from the liquid film surface, and sensible heating of liquid draining between nozzles [Pautsch and Shedd 2005, 2006]. Visualization of the nozzles spraying onto a transparent surface gives support for this theory. Two important regions were identified in the tested four nozzle arrays, the spray impact region and the spray interaction/draining region, and it was believed that the heat transfer performance is vastly different between these two regions due to a loss of fluid momentum when droplets from neighboring nozzles collide. The results of the TOIRT experiment further support this theory. The left of Figure 11.7 shows a four-nozzle array spraying onto a transparent surface, while the right is a map of the heat transfer coefficient for a similar nozzle design. On the left, the white circles represent the approximate areas where the spray directly impacts the film. The dark dashed line traces a region of high turbulence and vapor entrainment that is believed to be associated with nozzle interactions and draining. Characterization of the nozzles from the manufacturer has shown a 5% to 10% variation in nozzle flow rates due to manufacturing tolerances. A clear correlation can be seen between the turbulent interaction region and the areas of lower heat transfer coefficients.

11.3.5 Summary

Spray cooling systems offer great potential for high heat flux applications such as next generation computer chips and power electronics, e.g., IGBT’s, due to high heat transfer coefficients. With the TOIRT method locally resolved measurements can be obtained with high accuracy and resolution. The results show local peak values of 2 W/cm^2K and average values of up to 0.54 W/cm^2K for a single nozzle and 1.0 W/cm^2K for a four-nozzle array on an area of 1.5 × 1.5 cm^2. These values match the heat transfer coefficients measured with the same nozzles at equivalent flow rates using a conventional method within 25% and 10%, respectively. Significant maldistribution of the heat transfer performance occurs, with some nozzles performing almost two times lower than others, exacerbated by the influence of the local liquid film flow caused by uneven draining. This uncertainty of performance limits the minimum safety margin for maintaining maximum junction temperatures on chips. This new technique provides a tool for improving the uniformity of heat transfer performance in spray cooling and other high heat flux removal systems, thus improving overall system performance and reliability. At this time, the level of heat that can be delivered to the system was limited by the power of the laser used as the IR radiation source. With the current level of heat, no evaporation of fluid is expected. To be able to measure the heat transfer coefficient in different regimes of spray cooling, heat loads larger than the ones tested in this report are required. For example, an additional source of radiation could be applied continuously while the primary laser is oscillated. Otherwise, the technique described here could be implemented without change.

The authors A. Pautsch, T. Shedd and S. Freund appreciate funding granted by Cray, Inc. to the Multiphase Flow Analysis and Visualization Laboratory at the University of Wisconsin - Madison through the Defense Advance Research Projects Agency High Performance Computing program and by the German Research Council (DFG) for the project “Heat Transfer in Complex Flows” at the University of the Federal Armed Forces in Hamburg. The authors are grateful to the Wisconsin Electric Machines and Power Electronics Consortium for the use of their IR camera.

12 Plate Heat Exchangers

Figure 12.1: Assembled plate and frame heat exchanger (image courtesy: Alfa Laval).

Plate heat exchangers (PHE) are recuperative heat exchangers composed of stacked plates separating the hot and cold fluid streams. The plates are either brazed or welded, or gasketed and hold together by a frame in a classic plate and frame heat exchanger. PHE are commonly used in the chemical and food industry and increasingly also in HVAC&R as well as in many other applications. Compared to competing designs like shell-and-tube heat exchangers, PHE offer high effectiveness at very compact size and are available off-the-shelf in a wide variety. An advantage of gasketed PHE, as shown in Figure 12.1, is the ease of maintenance and the extensibility, since gasketed plates can be dis- and re-assembled in short time for cleaning and plates can be added to adapt to higher loads. Because of their high surface-to-volume ratio, PHE belong to the group of compact heat exchangers.

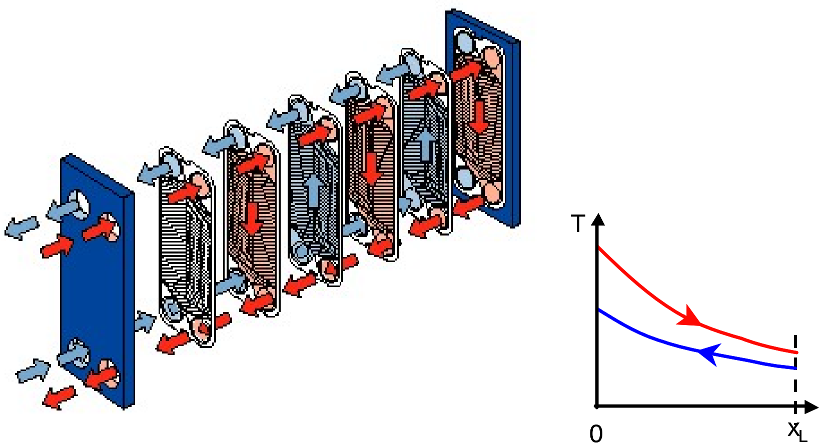

Figure 12.2: Flow principle in a PHE (left image courtesy: Alfa Laval).

PHE owe their high heat transfer effectiveness not only to the large surface area, but also to the specific design of the plates. They feature corrugations, usually sinusoidal wave shaped, commonly arranged in chevron patterns with opposite pitch angles in a plate pair. The surface structures force the flow in the plate channels into certain intersecting flow paths and induce high levels of turbulence. The angle of the chevron pattern is a decisive factor for heat transfer performance and pressure drop. With increasing angle, the longitudinal wavy flow along the furrows gives rise to crossing flow, mixing and heat transfer advances with a sharp gain in pressure drop. The hot and cold side fluids usually stream in counterflow arrangement to minimize the approach temperature, Figure 12.2. The inlet and outlet headers on the plate can be arranged for diagonal flow or, more common, for flow with both headers on the same side across the plate, the latter shown in the figure. PHE are mostly used for liquid fluids with low viscosity in single-phase flow. This type of heat exchanger is also becoming common for evaporators and condensers in HVAC&R applications when liquid secondary fluids are involved, e.g. as chillers or for water-cooled condensers. Quasi-local heat transfer coefficients during condensation and evaporation have been investigated by Kabelac and Freund [2007]. However, this chapter will consider single-phase flow only.

In the first section of this chapter, experimental data of the heat transfer coefficients in a PHE are shown, and in the second section computational fluid dynamics (CFD) simulations of the PHE are presented. The computed results are compared to the experimental data to judge the accuracy of CFD turbulence models. Ultimately, calibrated CFD simulations will allow parameter studies and geometry optimization with the conflicting objectives of heat transfer maximization and pressure drop minimization.

Despite the industrial prevalence of PHE, only limited detail is known from experiments about their fluid dynamics and subsequently the local heat transfer inside. A major contribution is due to Stasiek et al. [1996], who investigated the distributions of local Nusselt numbers on cross-corrugated surfaces. The heat transfer measurements were obtained using the thermocromic liquid crystals (TLC) method on model structures in a wind tunnel. The studied geometries are primarily used for rotary air preheaters, but the geometry is very similar to the structure in common plate heat exchangers. Their results include Nusselt number maps of unitary cells of the cross-corrugated structure for various angles and Reynolds numbers. Their experiments were supplemented with CFD simulations [Ciofalo et al., 1996] that gave insight into the swirling flow regime; the Nusselt numbers calculated with the LES method showed good agreement with their experimental data.

Gaiser and Kottke [1989] used the ammonia absorption method (AAM) to study flow phenomena and local heat transfer coefficients of PHE plates in a wind tunnel for Re = 2000 and plate profiles with various pitch angles and corrugation wavelengths. The AAM is based on the analogy of convective heat and mass transfer. They determined the heat transfer coefficients from the light reflectance of the absorption paper samples and presented a surface map of Nusselt numbers.

Zettler et al. [2001] used the noninvasive Positron Emission Particle Tracking technique for mapping the flow pattern inside a 60° cross-corrugated diagonal flow PHE. The technique relies on radioactive tracer particle (240µm) producing 3D trajectories and velocity profiles observable by Gamma ray detectors. Low flow zones were found in the corners of the inlet and outlet headers and along the side edges, while high flow velocity was discovered diagonally from the inlet to the outlet with an average velocity 0.35 m/s. However, the resolution of their method did not allow finding small-scale flow details like stagnation or recirculation zones.

To study fouling phenomena under various flow conditions, Kho et al. [1997] investigated the flow distribution with transparent plates allowing visual inspection of flow paths with suspended tracer particles. They also report the highest velocity on a diagonal path between the inlet and outlet ports of the plates with slower flow off this main path; however, no detailed flow distribution map is provided.

The experimental results of the present study include high resolution surface maps of local convection coefficients for different Reynolds numbers of water and can be used for the validation of new CFD models of plate heat exchangers, as shown in the section PHE Simulations, following the measurements.

12.1 Measurements on a PHE

A schematic of the experimental set-up for the TOIRT method on a plate heat exchanger is drawn in Figure 12.3:

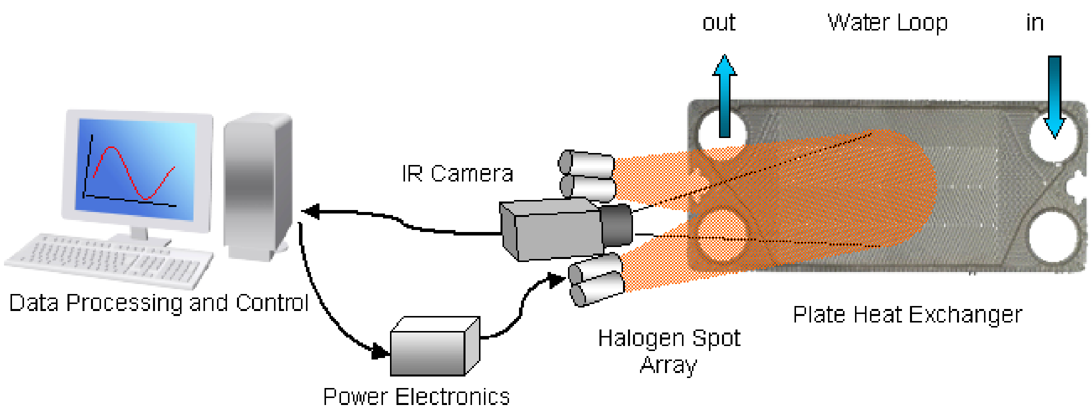

Figure 12.3: Schematic of the experimental setup.

Around the heat exchanger plate a water loop is installed with a 3 kW pump controlled by a variable frequency drive. The flow rate is measured with a turbine flow meter. A bypass circuit with a bath thermostat keeps the inlet water at 25°C. Heat exchanger plates are usually mounted in a frame with endplates to pressurize the assembly and tighten the gaskets; this would not allow viewing the plate surface. For this setup, the plates must be operated in a water loop without the frame and endplates. The plates used in these experiments are actually a laser-welded cassette, an assembly of two plates that do not need a gasket. To ensure sufficient pressurization without the endplates and the frame, the system is maintained under sub-atmospheric pressure at about 90 kPa at the inlet. This is achieved with a vacuum pump and a low-pressure tank in the water loop that also serves as a de-aerator. The geometry of the plates considered in this study is two-column chevron-type cross-corrugated (herringbone) with a pitch angle of q = 63.3°, a corrugation amplitude of a = 1.6 mm (3.2 mm total) and a wavelength of $L = 12$ mm (Table 12.2). The surface enlargement factor f_S according to [Martin, 2002] becomes

$$f_S = \frac{1}{6}\left[1+\sqrt{1+\left(\frac{p\,a}{\Lambda}\right)^2}+4\sqrt{1+\frac{1}{2}\left(\frac{p\,a}{\Lambda}\right)^2}\right]. \tag{12.1}$$

With a surface enlargement factor $f_S = 1.159$ for this geometry, the hydraulic diameter on which the Reynolds number $Re = \mathrm{v}d_h/\nu$ is based becomes $d_h = 2a/f_S = 5.5$ mm [Martin, 2002]. The plates are made of stainless steel 1.4401/ANSI 316 and have a constant thickness of $t_p = 0.6$ mm. The heat source used was either a 15 W diode laser for small areas, or an array of halogen spot lights with a total of 3.2 kW electric power, modulated with a frequency of 0.2 Hz or 0.1 Hz. Although the optimum frequency is close to 0.2 Hz, the largest area was measured with 0.1 Hz to increase the amplitude to a value high enough for the camera's detector and mitigate the objectionable effect of the fluid temperature oscillation. The fluid temperature oscillation appears when the fluid capacitance rate is low compared to the length of the heated area and affects the measurements by increasing the phase delay. Their detrimental effect has to be compensated mathematically to extract the phase lag due to the convection only (see chapter 7 Fluid Temperature Oscillation Effect). The varied parameter in this investigation is the water flow rate, chosen to cover the usual operating conditions of a PHE with three steps corresponding to Reynolds numbers in the fully turbulent range, with mean velocities of v = 0.17, 0.34 and 0.64 m/s.

12.1.1 Measurement Results

In this section, the results of the application of the TOIRT to plate heat exchangers are presented, some of which were published by Freund and Kabelac [2006]. Three sets of measurements are reported on different areas of the plate as shown in Figure 12.4, allowing to study the overall distribution as well as high-resolution local convection coefficients.

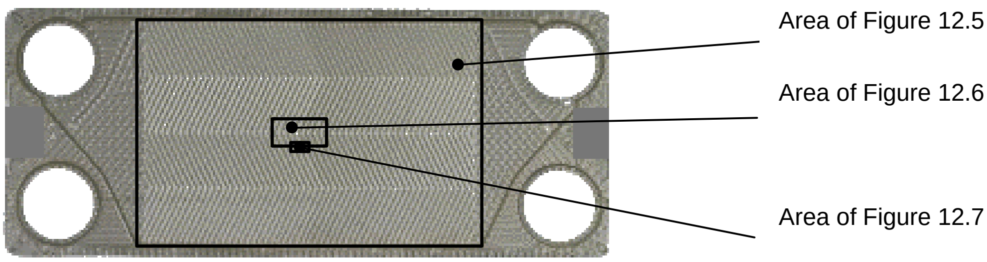

Figure 12.4: Heat exchanger plate with marked area sections for the respective figures.

Figure 12.5 displays an approximate heat transfer coefficient distribution over the entire chevron field with an area of 480 x 720 mm^2. Generally, darker zones contribute less to the heat transfer, whereas lighter zones have high heat transfer rates and are desirable for a plate heat exchanger, any maldistribution reduces the overall heat transfer for a given pressure drop. The inlet header section begins at the immediate right of the area, the entrance is outside the image on the upper right, the exit outside at the upper left, thus the mean flow direction is from right to left. Horizontal flow paths of higher velocity, discernable by higher calculated convection coefficients, appear to be along the arrowheads of the chevron pattern. The higher velocity along the chevron arrows was also observed by IR imaging of the unsteady temperature distribution when changing the flow rate. Contrary to the assumption that the shorter flow path between the headers, which lies in the upper section of the plate, would show generally higher velocity and heat transfer, the lower half of the plate also has areas (right bottom of the image) with high velocity and convection. Unlike the findings from Zettler et al. [2001], who also show a whole plate flow pattern map with comparable average velocity but diagonal flow arrangement, the regions closer to the edge and in the corners of the plate do not receive significantly less flow and have lower convection, only in the lower left corner the fluid moves slower. The deviations of the distribution decrease with increasing Reynolds number, as can be expected because the increased pressure differential forces the fluid distribution to become more uniform.

The accuracy of the heat transfer coefficient data shown in Figure 12.5 is very low and should only be taken to estimate the velocity distribution. The aforementioned effect of the fluid temperature oscillation is very pronounced here due to the stream-wise long area compared to the velocity und capacitance rate. The compensation algorithm does not work very well when the velocity field is slightly uneven, as areas with higher velocity will be overcompensated, leading to an overestimation of the convection coefficients. Likewise, areas with slightly lower velocity will be under-compensated, leading to lower calculated convection coefficients. In effect, the uncertainty strongly increases in flow direction, as becomes evident in the figure towards the left, where the deviations from the mean become very large. In addition, measuring such large areas with high heat transfer coefficients is challenging due to equipment limitations. The heat source power, the spatial resolution and the noise of the camera’s detector limit the accuracy of the measurements. The temperature amplitude is very small, less than 0.2 K, causing a signal-noise ratio of less than one. The measurement frequency of 0.1 Hz is lower than the optimum for the expected heat transfer coefficients, to reduce the temperature oscillation effect. However, this leads to high sensitivity in the calculations. Since the spatial resolution is coarse compared to the size of the characteristic features of the distribution, gradient averaging and aliasing affect the calculated heat transfer coefficients, as outlined in section 4.3. The prominent spot in the upper left clearly is a measurement error, as the amplitude is larger while the phase-lag is smaller, and could be caused e.g. by locally decreased wall thickness. Even though the data in Figure 12.5 is only an estimate for orientation, it can be concluded that the flow distribution within this range of Reynolds numbers does not show any strong maldistribution, significantly preferred flow paths or areas with very low convection. Only along the arrowsheads of the chevron, at low and medium Reynolds numbers, the velocity in mean flow direction is higher. The headers distribute the flow quite effectively, as even the corners show high heat transfer coefficients.

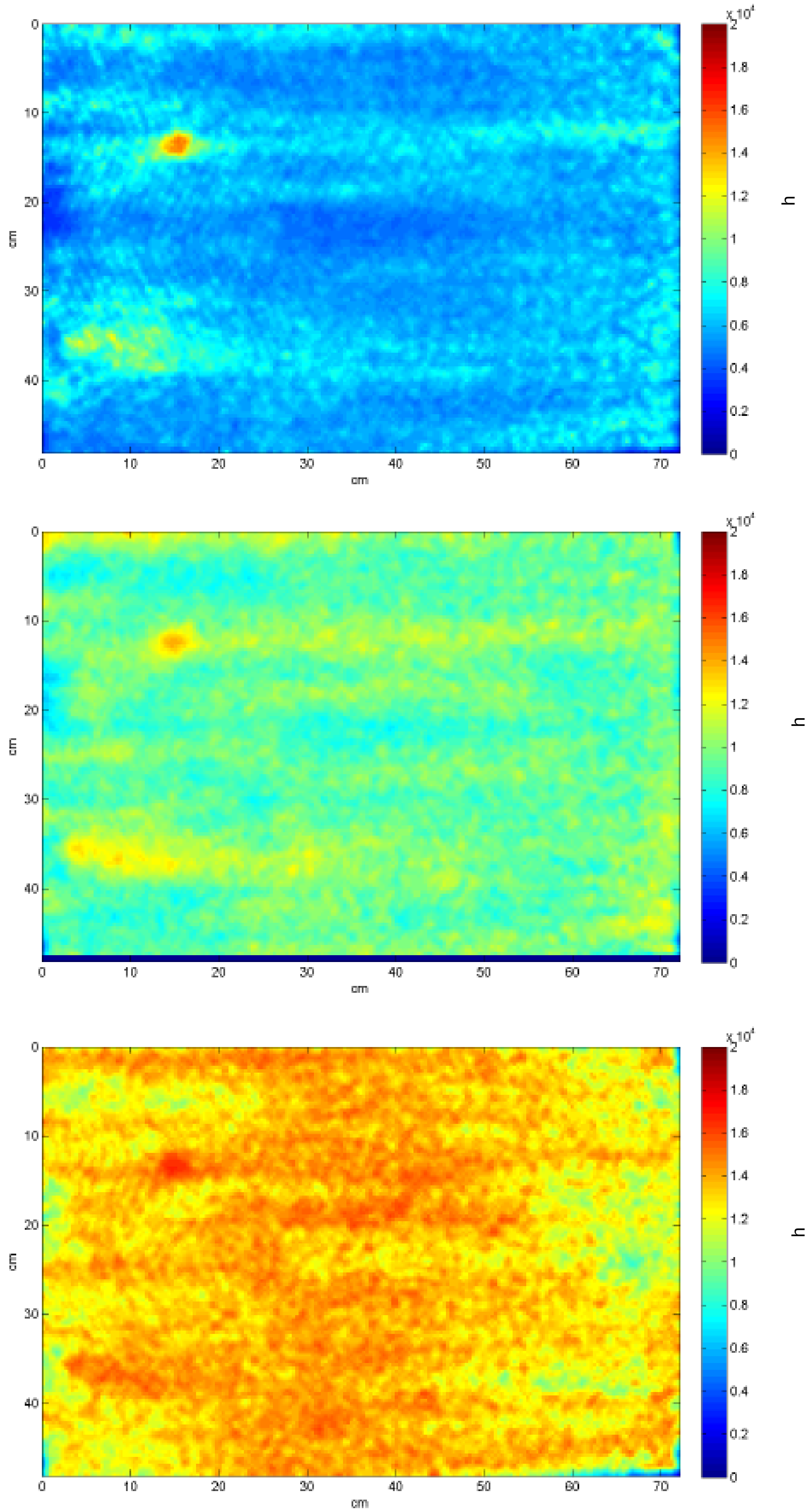

Figure 12.5: Approximate distribution of the heat transfer coefficients over the entire chevron field with a) *Re* = 1060 (upper), b) *Re* = 2120 (middle) and c) *Re* = 3980.

The following results are for smaller areas of the PHE and were measured with a frequency of 0.2 Hz, which allows obtaining more reliable values due to smaller sensitivity X at high heat transfer coefficients. Figure 12.6 a) to c) shows the heat transfer coefficients on a 152 x 76 mm^2 section in the center of the plate with a resolution of 1 mm^2. This center section is assumed to be representative of the whole plate and give a good estimate of an average heat transfer coefficient, independent of local deviations. Each map of heat transfer coefficient comprises the average of at least four measurements. The measurement uncertainty for the average of the data presented in Figure 12.6 a) to c) is about a) ±9.7%, b) ±12% and c) ±17%. The uncertainty was estimated based on an uncertainty of 2.5% for the material properties, 5% for the wall thickness and an average phase delay uncertainty of 0.02 that includes a synchronization variance of 6 ms and allows 10 ms uncertainty for the heat flux delay of the halogen lamps.

In Figure 12.6 a) for Re = 1060 the heat transfer coefficient extrema distinctly follow the ridges, with the maxima on a line in mean flow direction right before the contact points of the front and backside structures and the minimum on a line connecting these points. With increasing velocities, from b) Re = 2120 to c) Re = 3980, defined zones of lower convection appear behind the contact points, with the maxima right before and the ridges less clearly defined. Apparently, stagnant zones with lower convection form behind the contact points. The ratio of the minimum to maximum heat transfer decreases from ca. 4 to 2, while the arithmetic and the harmonic area averaged heat transfer coefficient, $h_{m,T}$ and $h_{m,q}$ (chapter 1, equation (1.4) and (1.5)), increase 2.25 times:

Table 12.1: Measured mean Heat Transfer Coefficients in the PHE.

Re	$h_{m,T}$ [W/m^{2}K]	$h_{m,q}$ [W/m^{2}K]	$(h_{m,T} + h_{m,q})/2$ [W/m^{2}K]
1060	8960	8331	8646
2120	12889	12374	12632
3980	19709	19113	19411

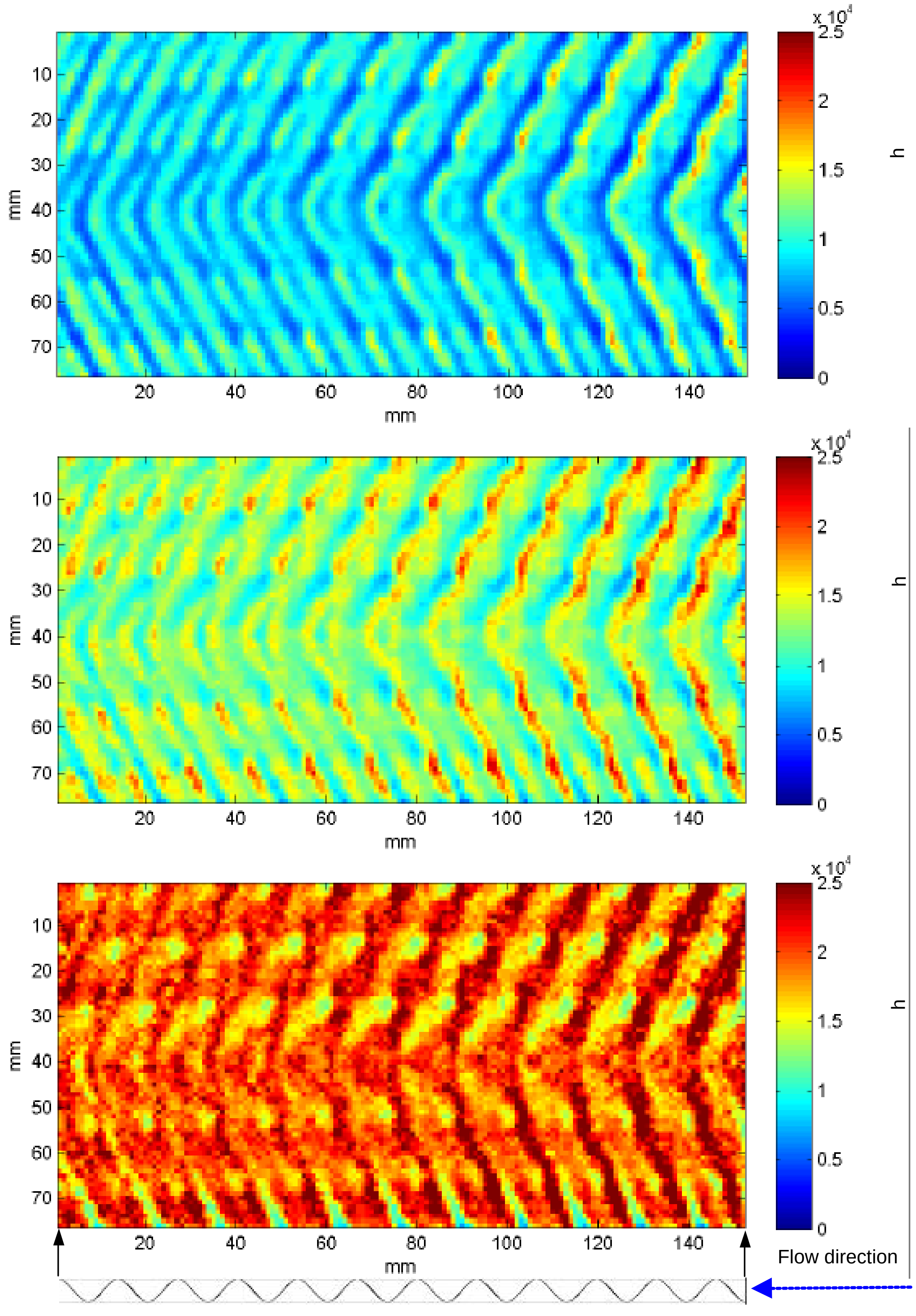

Figure 12.6: Maps of heat transfer coefficients for a) *Re* = 1060 (upper), b) *Re* = 2120 (middle) and c) *Re* = 3980 (lower). Below a cross section cut of the plate profile at the bottom line of the maps is shown.

Figure 12.7 shows a detailed map of the heat transfer coefficients over a length of three wave patterns, the area is 40 x 20 mm^2 with a resolution of 0.5 mm. The Reynolds numbers are again a) 1060, b) 2120 and c) 3980. The general observations from Figure 12.6 can be studied here in detail. The heat transfer maximum occurs in mean flow direction right before the contact points of the front-and backside plates; this heat transfer coefficient appears to be ca. two to three times higher than the average. The minimum convection is found right after the crossing. The maximum heat transfer coefficient is about four times higher than the minimum. The heat transfer coefficient shows a line of local maxima along the decline of the corrugation wave, followed by a line of local minima connecting the contact points at the base and along the up-slope after the base that is ca. 30% lower than average. Near the crest of the wave, the heat transfer is slightly higher than average in certain regions. Stasiek et al. [1996] show local Nusselt numbers on the surface of a unitary cell of a comparable cross-corrugated structure for air with *Re* = 2400. Some of their qualitative findings as well as their ratio of the maximum to the minimum convection, ca. 4, are comparable to the present conclusions from Figure 12.6 and Figure 12.7. However, Stasiek et al. state that the Nusselt numbers in a central region along the crest of the wave were very low and contributed little to overall heat transfer. This conclusion cannot be drawn from the present measurements for any Reynolds number; instead, even local maxima were found in this region. These maxima could be explained by the presence of the vortices calculated with the Large Eddy Simulation method by Ciofalo et al. [1996], and by the flow field from present RANS simulations shown in the next section that also exhibits such vortices, which impinge on the wall. Gaiser and Kottke [1989] showed a surface map of $Nu/Pr^{0.4}$ for a similar geometry for *Re* = 2000. They observed high values up to 80 along the crest of the corrugations and low values down to 20 in between, a similar range as in the current data.

Figure 12.8 shows a comparison of the area-averaged heat transfer coefficients $(h_{m,T} + h_{m,q})/2$ from Table 12.1 with values according to the correlation given by Martin [2002] and interpolated data from Thonon [1995]. The agreement of the present measurements with the data from Thonon seems remarkably good. While the literature values refer to the actual wetted plate surface area including the headers, the present values only refer to the heat transfer area in the middle of the plate where they were measured; that might lead to a slight over-prediction if extrapolated for the entire area. The measurement methods used by Martin and Thonon are very different from the present study, steady state operation of a plate heat exchanger equipped with thermocouples in a cold and a hot fluid, versus the TOIRT method on a plate assembly with a single passage with cold fluid and very low heat flux. However, the results are comparable because the heat transfer coefficient is largely heat flux independent at non-boiling single-phase flow and there is no interference from the convection on either side of the channel as the thermal boundary layer is very thin and periodically rebuilt in the corrugations. Gaiser and Kottke [1989] present an area average value of $Nu/Pr^{0.4}$ = 50 at *Re* = 2000 (63° pitch angle) also corresponding very well to the present data.

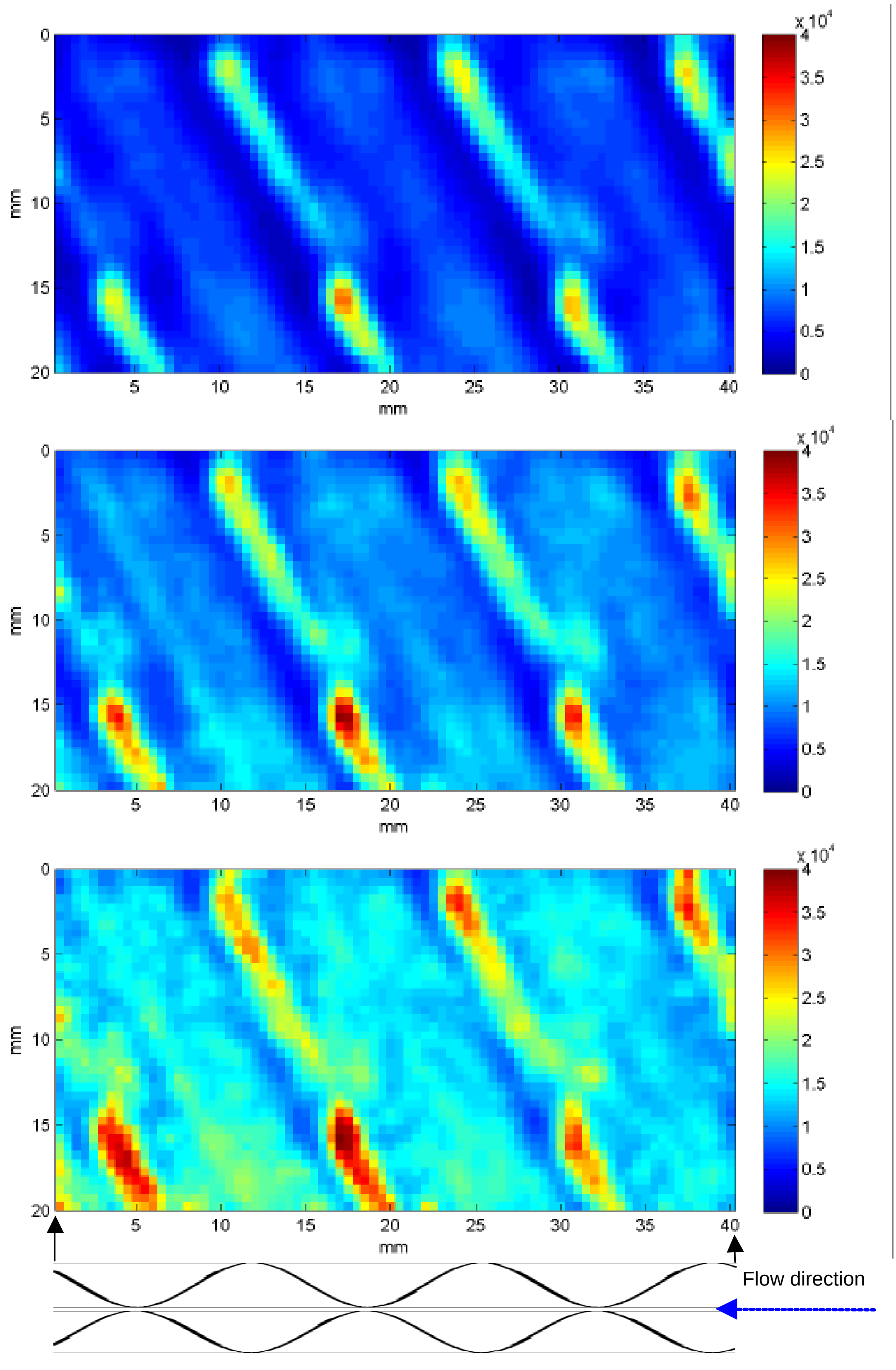

Figure 12.7: Detailed map of heat transfer coefficients for a) *Re* = 1060 (upper), b) *Re* = 2120 (middle) and c) *Re* = 3980 (lower). The lower part shows a cross section cut of the plate assembly at the bottom line of the map.

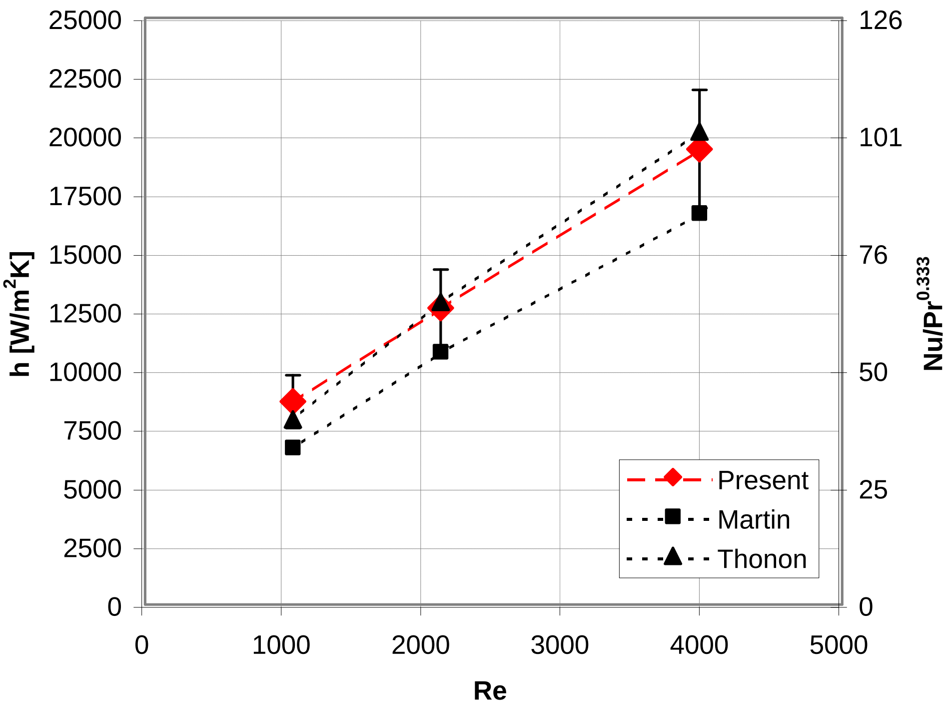

Figure 12.8: Comparison of the average heat transfer coefficients and Nusselt numbers with literature values.

The measurements on different areas of the PHE have shown the local distribution of convection coefficients, which varies in a periodic pattern from a minimum at the contact points of the corrugations to a maximum about 4 times higher. The area-mean heat transfer coefficients agree very well with literature data. The fluid velocity distribution is found to be rather even, with no areas receiving significantly higher flow rates than others.

12.2 PHE Simulations

12.2.1 Review of Numerical Studies of PHE

The considerable industrial interest in PHE and the experimental difficulties of investigating flow details spawned many numerical studies. The results may be useful to gain insight in flow pattern responsible for heat transfer, pressure drop and fouling and can lead to the optimization of plate profiles for various conditions. Some of the studies are briefly reviewed here and consequences drawn for the current investigation.

Shah et al. [2001] shed light on the current challenges in the numerical simulation of compact heat exchanger surfaces. They also provided a good overview over turbulence modeling, concluding that LES and DNS may provide superior models but presently require excessive computing time for all but the simplest geometries at low Reynolds numbers. However, LES and DNS hold promising future prospects with computing power exponentially growing. RANS k-ε models on the other hand had gained industrial-level acceptance as a successful engineering tool for simulating turbulent flows. They found that turbulence develops in cross-corrugated ducts for *Re* > 200.

Patankar et al. [1977] investigated the basics of fully developed flow and heat transfer and describe a concept of studying only a periodic section of a channel, encompassing all flow variations once that are repeated periodically. Thus, the analysis can be limited to a periodic section of the channel and is independent of thermal or hydraulic entrance region effects. Patankar et al. provide equations for the pressure and the temperature in a channel with a periodically recurring profile over the cross section and a term that linearly increases in flow direction. The linear pressure term is essentially the pressure drop over the length of the periodic section, which depends on the mass flux, while the linear temperature rise also depends on the wall heat flux. For a uniform wall heat flux case, the temperature field is fully developed when stays constant at periodic sections after subtracting the linear temperature gradient. To characterize fully developed conditions for a uniform wall temperature case, a non-dimensional temperature is defined that stays constant at periodic sections. This temperature is normalized by the wall temperature and a bulk temperature, which is modified to account for possible re-circulating flow. They discuss periodic boundary conditions for a uniform wall temperature heat exchanger case using this dimensionless temperature methodology and derive the set of partial-differential equations that govern a periodic section of the flow and temperature field. A 2-D finite-difference scheme was applied to solve the flow field and the wall heat transfer in a transverse-plate heat exchanger under laminar flow. Results in form of streamline and Nusselt number plots are presented.

Wang and Vanka [1995] studied the flow pattern and heat transfer in a periodic sinusoidally curved converging-diverging channel using a 2-D transient direct numerical simulation. Periodic inlet/outlet boundary conditions were imposed for the velocity and a non-dimensional temperature profile that must be constant at periodic points. The laminar and transitional flow regime was simulated, with steady oscillatory flow behavior found above Reynolds numbers of 180. Cross section plots show temperature contours and streamlines for various laminar Reynolds numbers as well as time instances of the vortices encountered at Reynolds number up to 520. The vortices and temperature profile again indicates the highest local Nusselt numbers at the converging part of the wall.

Blomerius [1997] did direct numerical simulations in 3-D for various heat transfer channels to study the velocity profiles, pressure drop and heat transfer coefficients. The critical Reynolds number with respect to two times the channel height was found to range from 300 to 400 for a 45° pitch angle cross-corrugated channel. The Nusselt number was found to be a strong function of the pitch angle and less influenced by the corrugation wavelength; compared to a plain channel, the Nusselt number was 2 to 8 times higher. From the simulation results of an periodic unit cell of a sinusoidal cross-corrugated profile with an angle of 45°, a length-amplitude ratio of 12 and Reynolds numbers of 200 (laminar) and 2000 (fully turbulent), different vortices can be identified that promote heat transfer. These vortices lie mainly on the decline of the upper corrugation wave where the channel converges, leading to maximum heat transfer. Minimum heat transfer occurs at the stagnation zone behind the contact points; further downstream eddy vortices are found, followed by longitudinal vortices that lead to low convection coefficients. The simulation results of Nusselt number maps look very similar to the present measurements, although the lines of local maxima and minima along the waves are less distinctive.

Utriainen and Sundén [2001] did a 3-D CFD simulation of the laminar flow and temperature field of air in cross-wavy ducts of various geometries that can be used for air-to-gas recuperators for small gas turbines. Partial periodic conditions are applied in flow direction and periodic conditions perpendicular to the main flow on a unitary cell. Nusselt numbers and pressure drop were shown to increase up to six times compared to straight ducts, influenced by the waviness for the ducts creating strong secondary flows.

Ciofalo and Di Piazza [2002] describe a CFD approach to simulate flow and conjugate heat transfer in a unitary cell of a PHE using the program CFX-4. They considered different geometries and fluids as found in liquid-to-liquid plate heat exchangers or in rotary air preheaters. Periodic respectively incomplete periodic boundary conditions were applied for the velocity and the temperature and pressure, respectively. Incomplete periodic means constant temperature profile minus the main flow large-scale gradient. Regions of the PHE where not fully developed conditions persist are pointed out, including the header sections, the border near the gaskets and central regions where the profile angle changes. A low-Reynolds number k-ε turbulence model was employed and no wall functions used. Simulation results of Nusselt numbers are presented for corrugated-undulated surfaces. These predictions were compared with experimental data from model plates in a wind tunnel measured with a TLC method [Stasiek et al., 1996]. The simulations slightly overpredicted the average Nusselt numbers, underpredicted relative heat transfer minima, and overpredicted local maxima. The qualitative heat transfer distribution was reproduced closely in the simulation while the exact periodicity of the distribution could not be found in the experiments. The simulation underpredicted the friction factor by 25%. Also presented are simulations for water flowing laminar with Re = 200, for cases of three different wall thermal conductivities and again in undulated-corrugated plates. The influence of the wall thermal conduction is discussed, transverse and longitudinal Biot numbers were calculated. Nusselt number maps for upper and lower side of each plate are shown, along with temperature distributions.

Etemad and Sundén [2007] studied the turbulent flow and the heat transfer in a unitary cell of a 60° pitch angle cross-corrugated PHE with air at a Reynolds number of 4930. They used the CFD software Star-CD and employed four different turbulence models, a high- and a low-Re k-ε model, an RSM and the V2F model. With a multi-block structured grid, the boundary layer was finely resolved for the low-Re k-ε and the V2F model, while wall functions were used for the high-Re k-ε model and the RSM with lower grid resolution. Periodic boundary conditions were imposed pair-wise between the inlet and the outlet with a fixed mass flow rate. They reported normalized mean Nusselt numbers and Fanning friction factors for each turbulence model case, as well as velocity fields and the local convection coefficients on the wall for a constant heat flux of 500 W/m^2. They found 20% difference of the mean Nusselt number and 50% difference for the friction factors between the different turbulence models. A secondary flow pattern resulting from the upper and lower flow interaction was identified that transports fluid from the wall to the center and thus enhances heat transfer. Etemad and Sundén conclude that the V2F and the RSM did not converge properly and do not recommend an RSM because it was numerical instable and gave similar results to a simpler high-Re k-ε model. Their scope is similar to the present investigation; however, the geometry is somewhat different and air rather than water at only one Reynolds number is used. Their results from different turbulence models could not be judged against the current experimental data.

The significance of PHE's in the diary industry has sparked several numerical investigations. PHE's were originally developed and used in the dairy industry, where fouling is a particularly delicate issue. Grijspeerdt et al. [2003] did 2-D and 3-D simulations of the flow pattern of milk between corrugated plates to find regions prone to fouling. A 2-D approach is found to be incapable of providing a complete picture. A RANS Baldin-Lomax mixing length turbulence model is used in the simulations at Re = 4482. The inlet flow conditions are found to influence only a very short entrance region including three corrugations. Streamline plots show eddy currents that can intensify heat transfer specifically at the up-slope of the corrugation, consistent with the current results. Fernandes et al. [2005] did 3-D FEM simulations of the middle section of a PHE with 60° pitched chevron corrugations filled with yogurt, a non-Newtonian fluid, being cooled with water in the other channel. The flow is laminar at very low Reynolds numbers $0.3 < Re < 12$. A heat flux profile boundary condition is prescribed based on the assumption of a spatially constant heat transfer coefficient on the cooling water side. Inlet and outlet conditions were known from experiments. They obtained 2-D temperature distributions and flow profiles as well as shear rates and viscosities of the stirred yogurt that were said to be in agreement with experimental data.

From the review can be concluded that CFD simulations, usually based on the finite-volume method including conjugate heat transfer between the wall the fluid, are suitable to study flow phenomena and the associated convective heat transfer in plate heat exchangers. Only 3-D simulations can capture the characteristics of the intrinsically 3-D turbulent flow in the plate furrows. DNS and LES, as used e.g. by Blomerius [1977], although possibly providing superior results, are computationally too expensive with sufficiently high spatial resolution for turbulent heat transfer at high Reynolds numbers. Turbulence models such as RANS k-ε can simulate the flow field quite well. The calculated heat transfer coefficients, however, are generally matching the experimental data not very well. Turbulence models that better approximate the decisive near-wall phenomena are desirable.

Simulating an entire plate is difficult because of the huge computing power requirements due to the large number of elements within the geometry. Most researchers therefore simulated a unitary cell of the periodic plate structure. To make the unitary cell truly periodic, considering fully developed flow, the boundary conditions must be periodic for the flow field respectively "incomplete" or partial periodic for the temperature and pressure profiles. Temperature and pressure are intrinsically non-periodic quantities, as they must change along the flow path when heat is added and a pressure drop occurs. Where periodic fully developed conditions prevail, these quantities consist of a part that linearly changes over the flow length, superimposed with a constant cross section profile. Partial periodic conditions thus mean that the surface normal derivative is constant while the integrated values increase in flow direction. Such an idealized unitary cell simulation of course is unable to reflect effects like uneven flow distribution that affect the entire plate. Such effects would have to be studied with a larger plate model including the headers but having a much lower mesh resolution to make the simulation possible under current computing limits.

The influence of the wall thermal conductivity should not be neglected, as it can enhance heat transfer by equalizing the local differences of convection coefficients on opposite sites of the plate; it exists an optimum wall thickness [Ciofalo and Di Piazza, 2002]. Therefore conjugate, i.e. coupled conductive-convective, calculations are needed; the local heat transfer ultimately does affect the heat transfer coefficients.

In the remainder of this chapter, CFD calculations are laid out and the resulting local heat transfer coefficients are compared to the experimental data. The simulation considers turbulent flow and through a unitary cell of a PHE under uniform wall heat flux and temperature, respectively. The geometry, material properties and the boundary conditions are set analog to the experimental conditions in this study to facilitate the validation of the simulation model. The simulation is limited to a unitary cell that represents the vast majority of such cells and the significant part of the total PHE area, thus capturing the core flow and heat transfer characteristics. Clearly, entrance effects and flow maldistribution cannot be captured, as by definition for periodicity the entrance effects are subsided. Such fully developed conditions prevail in good approximation in the real apparatus after a small number of repeated corrugations after the headers in the greater part of the plate.

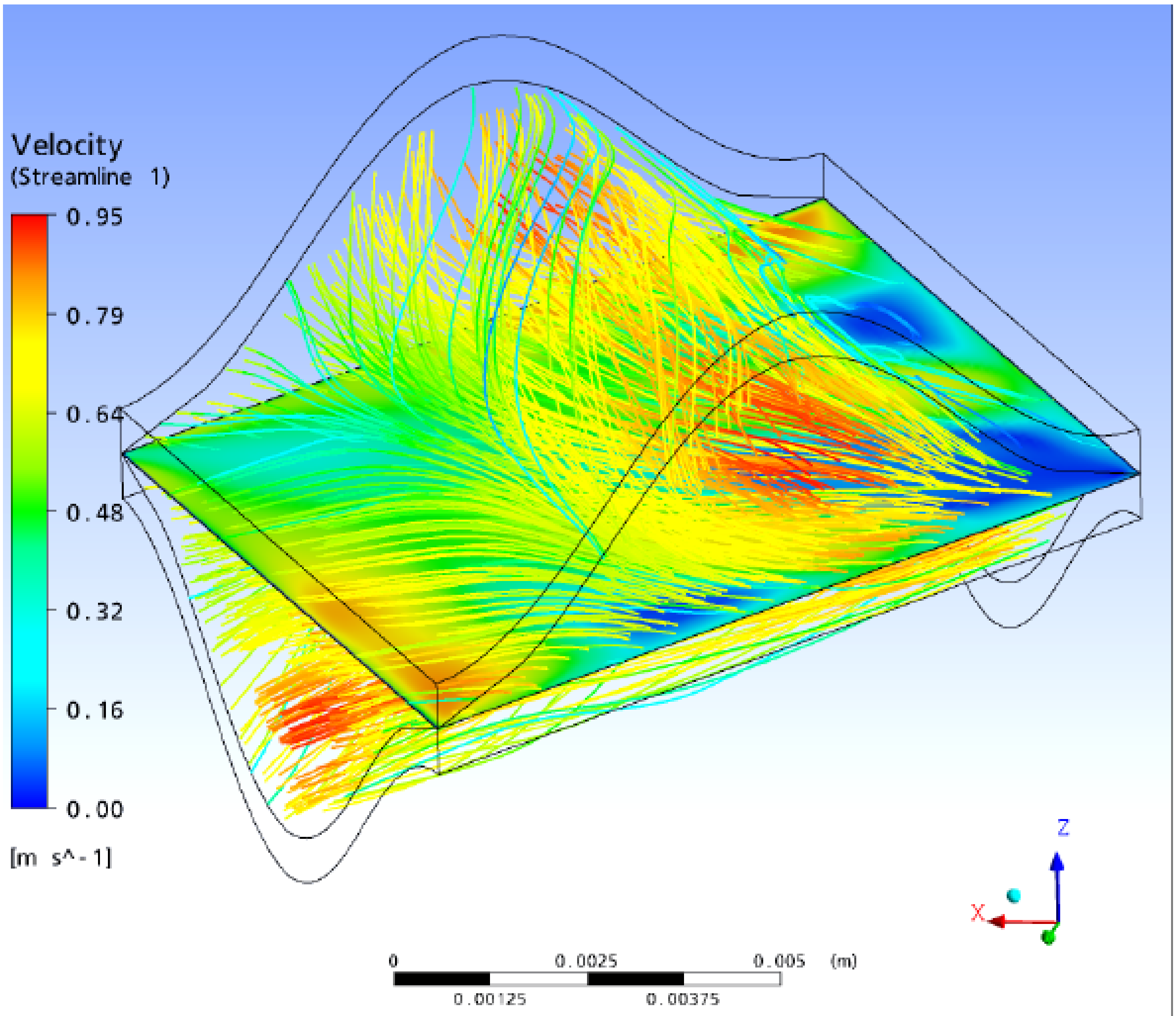

Figure 12.9: CFD data showing the velocity field and the swirling streamlines in a unitary cell of a PHE. Mean flow direction right to left along x-axis, *Re* = 2120.

12.2.2 Turbulence Modeling

CFD Simulations rely on a numerically discretized fluid domain; velocity, pressure and temperature can be calculated at the grid nodes according to a set of balance equations for a finite volume. Computations of turbulent flow fields can be conducted with the Reynolds averaged Navier Stokes (RANS) equations. These equations originate from the Reynolds decomposition of the instantaneous Navier Stokes equations of the turbulent flow field, into a steady mean component and a fluctuating part, the Reynolds stress tensor. These turbulent fluctuations are responsible for the small eddies, enhanced mixing and energy dissipation in turbulent flows. The Reynolds stress tensor is in most CFD simulations treated with a class of turbulence models called Eddy Viscosity Models (EVM's). Such models calculate the Reynolds stresses according to the Boussinesq hypothesis based on the respective velocity gradients, a turbulent kinetic energy k and an additional momentum diffusivity, the turbulent eddy viscosity. Commonly two-equation models are used that derive this number in the flow field involving transport equations for the turbulent kinetic energy k and the dissipation rate ε or the turbulence frequency ω with sets of empirical constants. For the sake of brevity, no derivation of the RANS equations and no further detailed review of the immense range of turbulence models will be provided here [Shah et al, 2001, Ansys CFX, 2006].

What applies to the momentum balance in the turbulent flow field, the RANS equations, applies in close analogy also to the energy balance, the Reynolds-averaged energy equations. Basically, heat transfer in turbulent flows can be described in much the same manner as in laminar flows with the addition of a turbulent eddy diffusivity according to the Bousinessq analogy, that relates the turbulent heat flux to the temperature gradient. For the closure of the Reynolds-averaged energy equations, this turbulent thermal diffusivity is derived in the standard k-ε model from the turbulent viscosity and a turbulent Prandtl number. The Turbulent Prandtl number is the ratio of the turbulent eddy diffusivity to the turbulent thermal diffusivity, in standard turbulence models it has a fixed value for a certain molecular Prandtl number; for gases e.g. it is commonly assumed to be 0.85 [Kays, Crawford, Weigand, 2005]. This stark simplification is an apparent reason for the results of turbulent heat transfer simulations being even less reliable than the flow field predictions. The challenging coupling of turbulent flow and heat transfer is of considerable research interest. The common approach to calculate the turbulent heat flux in EVM's as described above is isotropic, i.e. the turbulent heat flux in each dimension depends on the respective temperature gradient only, without accounting for the local gradients in other directions. However, Dietz, Neumann and Weigand [2007] point out that theoretical as well as numerical and experimental investigations have shown that the turbulent heat flux indeed is anisotropic and 3-D local temperature gradients should not be neglected in the calculation. Dietz et al. [2006, 2007] use an anisotropic algebraic approach, taking into account 3-D local velocity gradients and the Reynolds stresses from the flow field for the calculation of the turbulent heat flux.

The two equation Eddy Viscosity Models reveal limitations in their capability to predict detailed features of complex 3-D flow fields, which originate from the simplified isotropic modeling of the Reynolds stresses, without accounting for the directional influence of local 3-D velocity gradients. Reynolds-Stress Models (RSM's) are a promising approach to model complex flow fields more precisely. In RSM's, the Reynolds stresses are determined from six PDE transport equations for convection, stress production, turbulent and molecular diffusion, dissipation and pressure strain. Because an RSM resolves the Reynolds stresses more accurately and captures the 3-D turbulent behavior accounting for flow features such as rotation, swirl and streamline curvature, it is principally better suited for the prediction of complex flows than other RANS models. However, since some new unknowns are introduced with the transport equations, which have to be modeled based on various assumptions, the results of RSM's are superior to simpler RANS models only when these parameters are well adjusted. Another obstacle for the widespread implementation of RSM's is that the number of equations to be solved for each node more than doubles compared to two-equation EVM's, considerable increasing computation costs, while the numerical stability and convergence is often more critical [Etemad, Sunden, 2007, Shah et al., 2001]. Despite these drawbacks, the potential benefits of higher accuracy and the availability of anisotropic algebraic stress models for the turbulent heat flux make RSM's very interesting. The flow and heat transfer predictions from the cooperating researchers at the University of Stuttgart, Dietz et al. [2006, 2007], using an RSM with an explicit algebraic stress model (EASM) for the turbulent heat flux, agreed well with experiments involving complex flows in arrays of vortex generators (see Chapter 9 Vortex Generators). A performance comparison of various anisotropic turbulent heat flux models on test cases with reliable LES and DNS data showed significant improvements over isotropic models [Dietz, Neumann, Weigand, 2007]. Dietz implemented several EASM's into commercial CFD software including Ansys CFX [2006]. The EASM based on the work of Younis et al. [2005] and extended by Dietz to allow near-wall calculations without wall functions was found to be the most promising.

In the present study to model the flow and heat transfer in a unitary cell of a PHE, a commercial two-equation SST turbulence model and a BSL RSM employing Dietz' EASM implementation are used. The computations are carried out with the commercial CFD software package Ansys CFX 11 [2006]. The simulations with the simpler SST model were performed first, followed by RSM computations. This approach allows on one hand a comparison of the results from the SST and RSM models and on the other hand reduces the computation time needed for obtaining converged results with the RSM when setting the initial conditions to the results data from the SST model. The SST-model has been used in CFX as provided without any parameters changed. The EASM for the turbulent heat flux was implemented into the BSL RSM in CFX via a so-called junction box routine that incorporates user-provided compiled Fortran code into the solver.

The Shear-Stress-Transport (SST) – model, developed by Menter [1993], was chosen because it allows more accurate simulations of wall-bordering flows than alternative two equation turbulence models. Accuracy of the flow field near the wall is particularly important for wall-fluid heat transfer calculations. The SST is a hybrid model, using a low-Reynolds k-ω-model for the near wall region and a k-ε-model in the main flow. It has shown to be more precise than other models regarding wall effects like detaching and re-attaching and is widely used in aerodynamic simulations.

Turbulence models like the standard k-ε-model cease to provide meaningful results within the boundary layer close to a wall, where the turbulence is gradually decreasing to zero in the viscous sublayer. Even a low-Reynolds k-ω-model that is specifically suited for wall adjacent flow cannot always resolve the flow nearest to the wall, depending on the local grid resolution. Coupling the flow and the wall in CFD programs is therefore often achieved with turbulent wall functions. Wall functions [Ansys CFX, 2006] provide for a linear near-wall velocity profile in the viscous sublayer for $0 < y^+ < 11.06$ [Bejan, 1984] and a logarithmic velocity profile for $y^+ > 11.06$, where y^+ is a non-dimensional wall distance based on the wall shear stress and the kinematic viscosity:

$$y^+ = \frac{y\sqrt{t_W / r}}{n} \tag{12.2}$$

Standard wall functions are strongly dependent on the grid spacing and the nearest wall grid point, leading to potentially large errors in the boundary layer calculations when the mesh is locally unfitting. CFX employs „scalable wall functions“ that overcome this disadvantage by limiting the application of the wall functions to a range consistent with the linear and logarithmic profile. This is independent of the grid point locations and can be used with arbitrary fine grids. The optional „automatic“ wall function treatment allows employing the scalable wall functions in combination with a low-Reynolds k-ω-model to achieve a very precise resolution of the boundary layer. In the present computations, the mesh is sufficiently fine for the SST model as well as the RSM to resolve the flow near the wall accurately without the use of wall functions.

12.2.3 Geometry and Grid Generation

The fluid and the wall domain of a unitary cell of a PHE were discretized to yield a finite volume mesh to be used in CFX simulations. The geometry and the grid generation was performed in Ansys ICEM CFD 11 [2007], starting with providing a mathematical function based on the geometry parameters that creates prominent points, which were subsequently interconnected by spline curves and planes and faces to form the geometry. The fundamental geometry parameters for the unitary cell are given in Table 12.2:

Table 12.2: Plate Parameters.

Corrugation amplitude a	1.6 mm
Corrugation wave length L	12 mm
Plate thickness t_p	0.6 mm
Chevron pitch angle	63.3°

This leads to the periodic element referred to as the unitary cell of the PHE, which is cut between four contact points with a major axis of 26.707 mm, a minor axis of 13.432 mm and a height of 6.4 mm for the fluid respectively 7.6 mm for the fluid with the wall, shown in Figure 12.10:

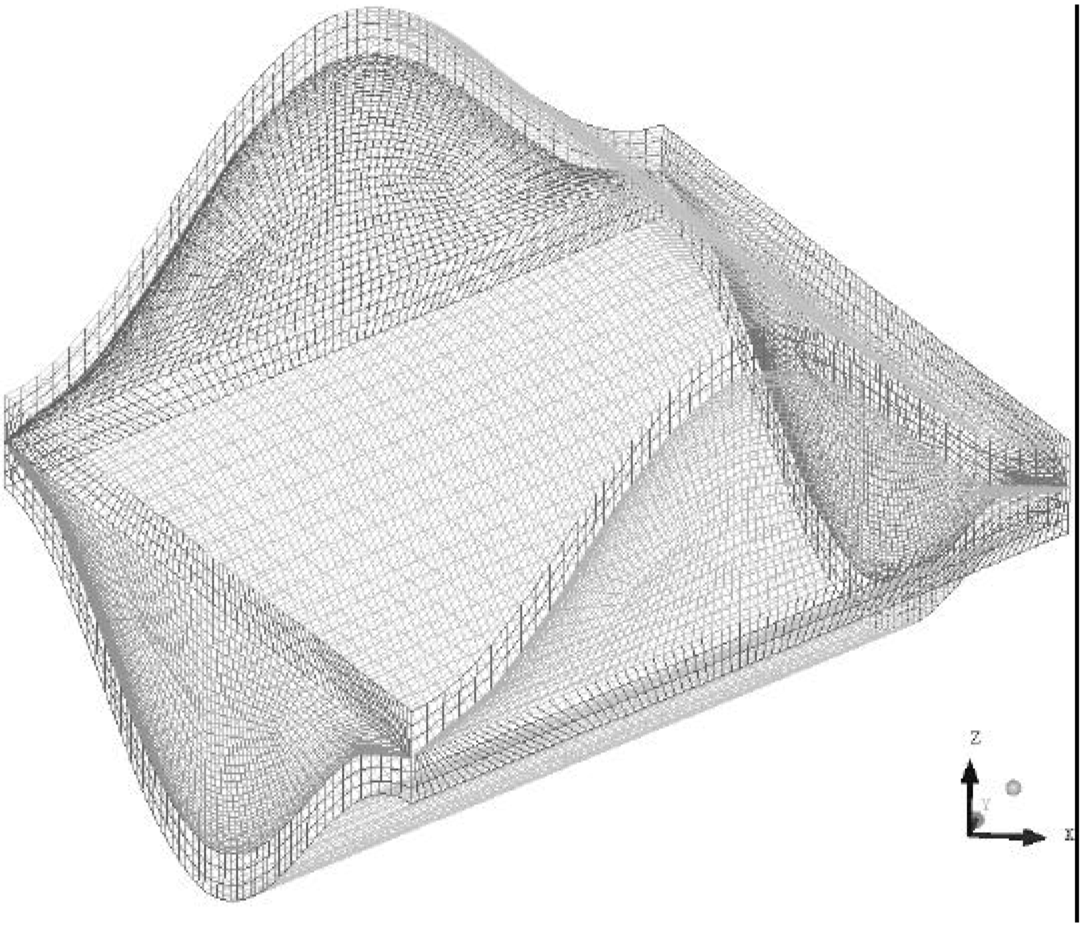

Figure 12.10 Mesh of the PHE unitary cell

The grid was generated as a fully structured hexahedra mesh using ICEM's 3-D multi-block features. A total of 56 blocks were created and associated with the geometry in the fluid and wall domains. The desired number of nodes and the spacing law was imposed onto each block's edges. For the wall neighboring nodes in the fluid, the spacing decreases exponentially to adequately resolve the sublayer with a distance down to 0.02 mm, ensuring a low y^+ about unity over the domain with an area-averaged $y^+ = 1.3$. The resolution within the wall itself was reduced to the maximum element size allowed by the node-to-node fluid-solid coupling and four elements for the wall thickness, since the good thermal conduction does not require a very fine grid compared to the fluid.

To prevent numeric problems at the corners of the geometry where the elements become very skewed, the asymptotically approaching sine curves were changed with a miniscule deviation into straight lines with a triangular approach; it can be seen in the corners of Figure 12.9 and Figure 12.10.

12.2.4 Boundary Conditions

To model a unitary cell that is representative for the large fully developed part of the PHE plate area, periodic boundary conditions have to be applied for flow and temperature field at the inlet and outlet. Boundary conditions (BC's) are applied in CFX on all faces of the mesh that were specified during grid generation. CFX Release 11 allows translational periodic boundary conditions be applied for the flow field with a specified mass flow. The velocities and turbulence variables are the same at the inlet and outlet faces, while the pressure decreases according to the pressure drop in the mass flow induced flow field. The mass flow is set to 0.01461 kg/s at each of both inlets, corresponding to the Reynolds number of 2120, as in experiments in the previous section.

Thermal BC's for the outer wall surfaces are set to a constant heat flux of 10000 W/m^2. The constant heat flux case is chosen because it corresponds closely enough to most PHE applications and can even be assumed in constant temperature cases because the area of the unitary cell is small compared to the overall area over which significant gradients occur. In turbulent flow the influence of the thermal BC on the heat transfer coefficient is generally small, as the upstream thermal history of the flow is blurred due to vortices and mixing. In reality, the heat flux will not be strictly constant over the inner surface area of the unitary cell because of the large local differences of the convection coefficients. It is assumed here that the high thermal conductivity of the wall equalizes such effects to an extend that their influence on the fluid heat transfer coefficient is not significant and the CFD results are realistic. The assumption of constant heat flux is also beneficial for the simulation as it allows an a-priori calculation of the bulk temperature increase. The thermal BC's for the inlet and outlet of the fluid have to be of partial periodic type, such that the bulk temperature may increase while the radial temperature gradient stays constant. This temperature gradient is the temperature profile at the periodic boundaries less the bulk temperature increase, which equals the heat flow into the domain divided by the fluid capacity rate:

$$\frac{dT_b}{dx} = \frac{q}{\dot{m}c}\frac{dA}{dx} \tag{12.3}$$

The implementation of such incomplete periodic BC's is beyond the standard capabilities of CFX; periodic temperature BC's exclude a bulk temperature gradient. A trick to work around that issue is applying a negative volume heat source S to counter the bulk temperature increase from the heat transfer and enable periodic boundary condition:

$$S = -\int q \, dA \, / \, V \tag{12.4}$$

However, the question rises how far this volumetric heat sink interferes with the temperature profile and such influences the heat transfer coefficients to be calculated. To investigate the effect of an internal heat source on the heat transfer coefficient, an analysis has been carried out on laminar pipe flow with constant wall heat flux. This flow configuration has been chosen because laminar flow can readily be evaluated analytically and because it exhibits a high sensitivity towards the radial temperature profile. Turbulent heat transfer coefficients are much less influenced by the temperature profile: if the influence of the internal heat source is small in laminar flow, it will be negligible in the turbulent case. The equation to start from to obtain the heat transfer coefficient is the energy differential equation for flow through a circular tube:

$$u\frac{dT_b}{dx} = a\,\frac{1}{r}\frac{\partial}{\partial r}\left(r\frac{\partial T}{\partial r}\right) + a\,\frac{S}{k}\,. \tag{12.5}$$

First, this differential equation is solved for the convection under constant heat flux with the mean velocity u_m and the surface temperature T_S at the pipe radius r_S to yield the fully developed temperature profile in laminar pipe flow:

$$T = T_S - \frac{dT_b}{dx}\frac{u_m}{8a}\left(\frac{r^4}{r_S{}^2} - 4r^2 + 3r_S{}^2\right) - \frac{1}{4}\frac{S}{k}\left(r^2 - r_S{}^2\right) \tag{12.6}$$

Here the bulk temperature gradient with the surface heat flux q is:

$$\frac{dT_b}{dx} = \frac{2q}{u_m\, r\, c r_S} + \frac{S}{u_m\, r\, c}\ , \tag{12.7}$$

which goes to zero for $S = -2q/r_S$. With the bulk temperature of the fluid with a parabolic velocity profile

$$T_b = \frac{2}{u_m r_S{}^2}\int_0^{r_S} u_m\left(1 - \frac{r^2}{r_S{}^2}\right) T\ r\ dr\ , \tag{12.8}$$

the Nusselt number finally becomes

$$Nu = \frac{96q}{22q + 3r_S S}\ , \tag{12.9}$$

which equals 6 for $S = -2q/r_S$, or for $S = 0$ the common value of 4.36. The analysis shows that even in laminar flow, which is unlike turbulent flow highly sensitive to the upstream temperature and heat flux profile, the difference between the heat transfer coefficient with and without the internal heat source is small, 37%. This justifies the assumption that for turbulent convection the use of an internal heat source to counter the bulk temperature gradient does not significantly influence the convection coefficient.

12.2.5 CFD Results

The CFD calculations were performed in Ansys CFX 11 [2006] using the PHE unitary cell model and the boundary conditions with the SST and the RSM turbulence model as described before. The isothermal flow field was computed first without solving the energy equation. The temperature field was then solved based on the flow field set as initial conditions. This decoupling was intended to speed up convergence and provide initial conditions for multiple calculations without starting over each time from an undeveloped flow field. A second order high-resolution advection scheme was employed in all simulations. Achieving convergence of the flow field was rather difficult and took considerable time and efforts. For the SST model it was required to relax the high-resolution scheme with a low blend factor towards a more robust upwind scheme to achieve acceptable convergence, which took about 1400 iterations with a physical timescale of 0.04 s for the flow field. The RSM showed generally better convergence behavior than the SST model and required 250 iterations for the flow field with a physical timescale of 0.02 s, starting from the SST solution. Specifically the RSM-EASM converged very well, solving for the temperature field with the EASM took only about 100 iterations until the residua stagnated, while the SST needed 1170 iterations. The RMS residuals for the flow field as well as for the heat transfer calculations are all below 10^{-5} and considered sufficient, although the original target of 10^{-6} was not reached for x- and y-velocity as well as for thermal energy.

The Reynolds number Re = 2120 is based on a hydraulic diameter of 5.5 mm and a mass flow rate of 2 x 0.0146 kg/s of water at a temperature of 25°C to give an average velocity in mean flow direction of 0.34 m/s consistent with the experimental conditions shown before. Both flow rates in the upper and lower half of the channel are equal according to the assumptions of periodicity, symmetry and even flow distribution. Figure 12.9 shows the streamlines and velocity from the SST model, indicating the complex swirling flow regime that leads to vortices and eddies, which cause strong mixing and the non-uniform distribution of the local convection coefficients. The maximum velocity of 0.95 m/s is about 3 times higher than the velocity in mean flow direction, which is about half of the average velocity in the domain of 0.6 m/s. The calculated pressure drop from the inlet to the outlet is 132 Pa. The turbulence kinetic energy over the cross section is shown in Figure 12.11 and Figure 12.12, perpendicular and parallel, respectively, to the mean flow direction. The findings are qualitatively very similar for the SST and the RSM simulation. The turbulence kinetic energy near the wall stems from vortices that act to thin the boundary layer by increased mixing, thereby enhancing the heat transfer coefficients. The light-colored zones near the wall in Figure 12.11 in the upper right and the lower left of the cross section contour point to the vortices that cause the heat transfer maximum along the decline of the corrugation wave, found also in the experimental data. These vortices reach right before the contact points, causing high convection coefficients here as well. The same can be observed in Figure 12.12 to the left. The CFD apparently underpredicts the viscosity that would have dampened eddies in the crevices of the corners. The high turbulence seen in the center is caused by the strong vortex formed by the opposing upper and lower streams.

The heat transfer coefficients are based on the local wall temperatures, the local heat flux and on the mass flow-averaged fluid temperature at the central cross section. This bulk temperature does not change noticeable from inlet to outlet. The data calculated with the SST and the RSM-EASM turbulence model are shown in Figure 12.13 a) and b). The contours can be directly compared with the measured heat transfer coefficients for a unitary cell in the middle of the plate at the same Reynolds number that is given in Figure 12.13 c). The CFD values are lower. The CFD data notably do not feature the distinct maximum before the contact points, but rather show a maximum spread along the decline of the corrugation wave in mean flow direction. The CFD data also lacks the local maxima around the ridge of the corrugation and features a region of minimal convection coefficients instead. However, upon closer investigation streaks of higher convection can be identified in the CFD data that are caused by similar vortices that may be responsible for the local maxima seen in the measured data. The minimum after the contact points is found in both data sets, however, in the CFD the minimum is interrupted by spots of enhanced convection in a recirculation zone. At the contact points themselves in the corners appears to be very high convection as pointed out by the high turbulence kinetic energy here seen in Figure 12.12. This is contrary to the measured data; the discrepancy may partially be due to slight geometric differences to the real plate and corner effects in the model. The extrema seen at the very edges of the CFD data may be artifacts from numerical errors at the periodic boundary conditions as there is no rational explanation based on the flow field.

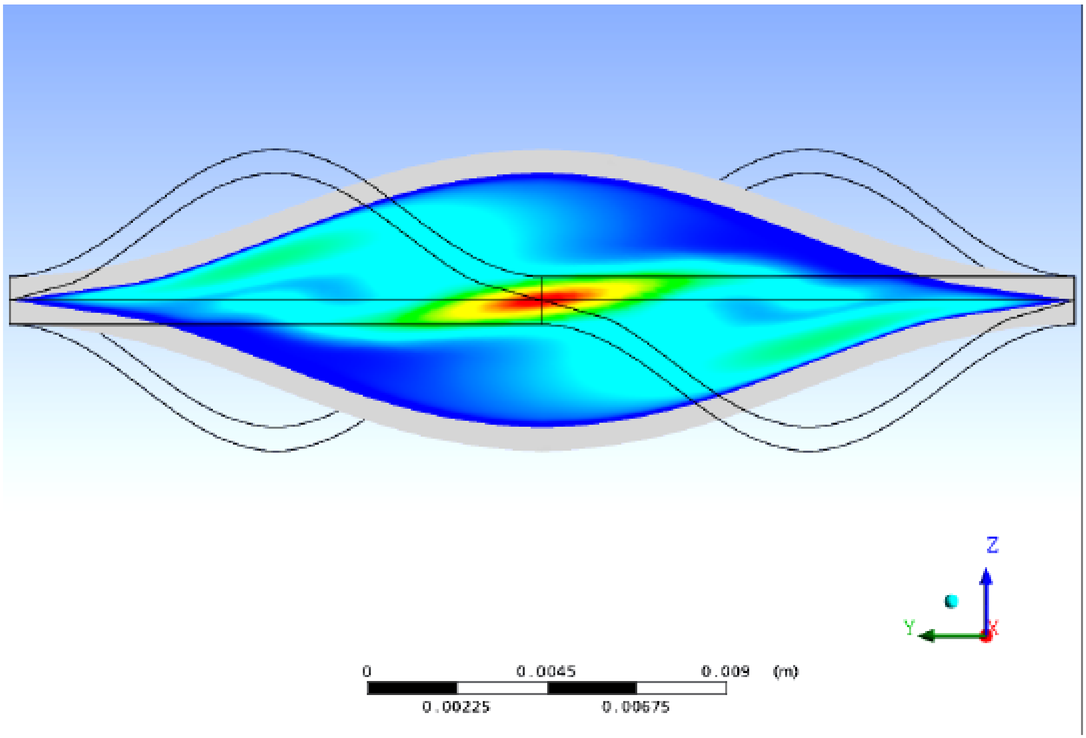

Figure 12.11: Turbulence kinetic energy k in the cross section of the unitary cell viewed in mean flow direction (SST model, $0 < k < 0.072$ m²/s²).

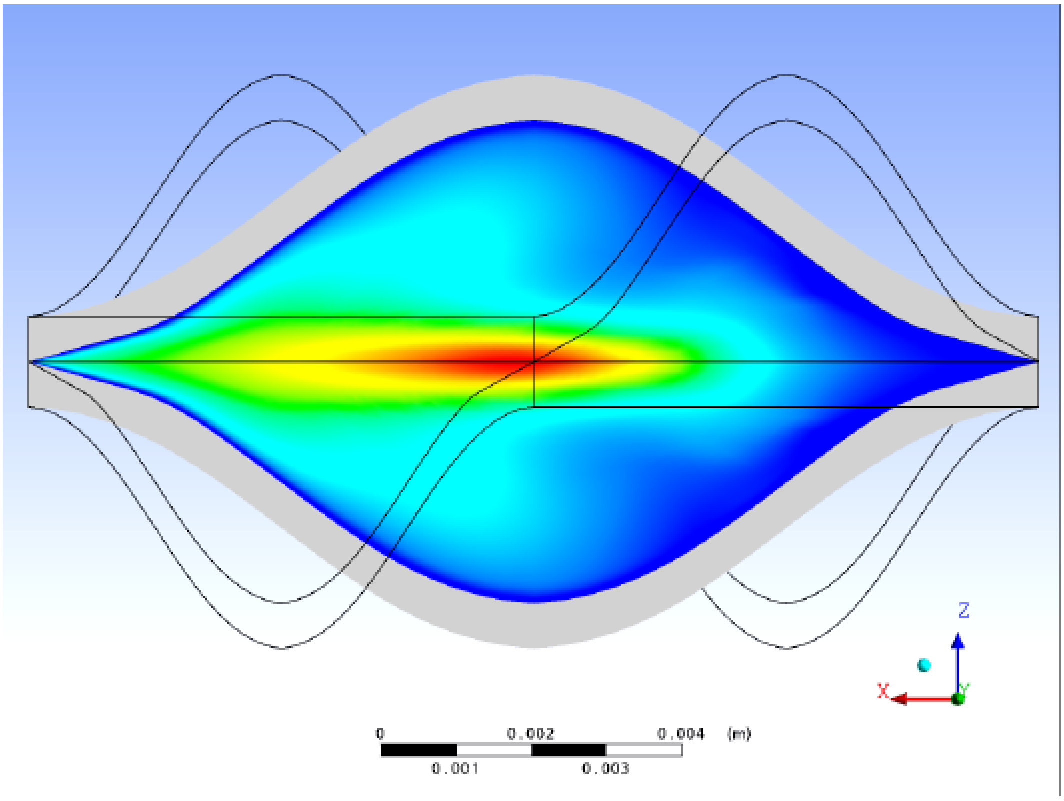

Figure 12.12: Turbulence kinetic energy k in the cross section of the unitary cell viewed perpendicular to the mean flow direction (SST model, $0 < k < 0.072$ m²/s²).

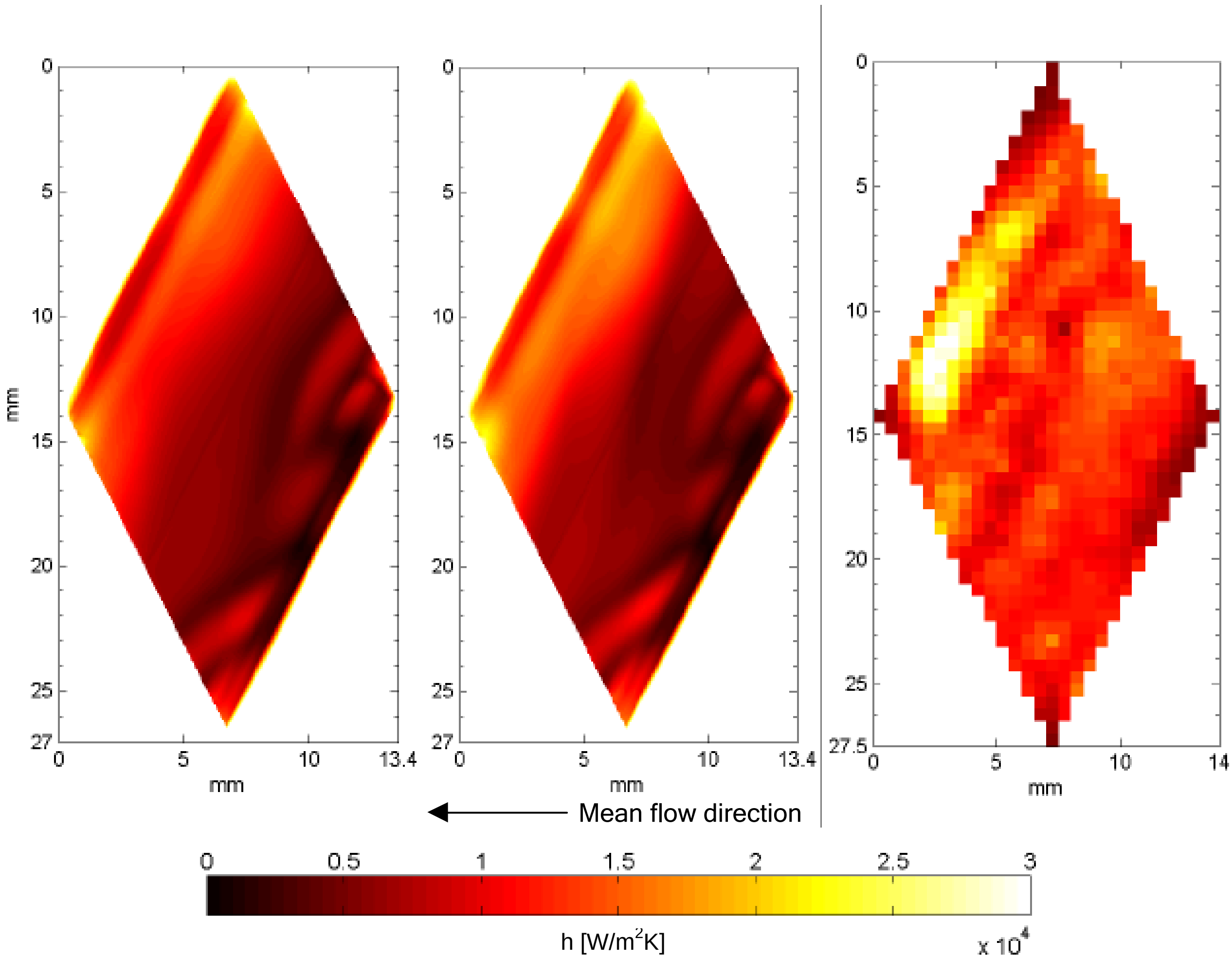

Figure 12.13: Heat transfer coefficients on the surface of a unitary cell at Re = 2120. CFD Simulation with a) SST turbulence model (left), b) RSM-EASM (middle) and c) TOIRT measurement (right).

The experimental data shown in Figure 12.13 and Table 12.3 were measured at a center section of the plate where typical and fully developed conditions prevail, specifically to be compared to the unitary cell simulation at *Re* = 2120. To find the exact position of the crossing points and crop the section equivalent to a unitary cell out of the array of measured data, another experiment was conducted without any fluid motion, in which the crossing points of the front- and backside plate profile became clearly visible. A laser was used as a heat source at 0.2 Hz and a Phoenix IR camera recorded the temperature oscillations. The uncertainty of the heat transfer coefficient measurement is about ±1560 W/m^2K (12%) for the arithmetically area-averaged number, based on an uncertainty of 2.5% for the material properties, 5% for the wall thickness and 0.02 for the phase delay, including a synchronization error.

Table 12.3: Mean heat transfer coefficients in the PHE, measured vs. CFD.

	SST	RSM-EASM	Measurement
$h_{m,T}$ [W/m^{2}K]	8908	9985	13264
$h_{m,q}$ [W/m^{2}K]	6380	6820	11821
$(h_{m,T} + h_{m,q})/2$ [W/m^{2}K]	7604	8403	12543

As shown in Table 12.3, the arithmetically averaged $h_{m,T}$ from the SST model is 33% lower, while the value from the RSM-EASM is only 25% lower than the reference measurement data. Larger differences occur between the harmonically area-averaged convection coefficients $h_{m,q}$, which both turbulence models underpredict by more than 40% (see chapter 1, equation (1.4) for constant temperature and (1.5) for constant heat flux). This indicates a less uniform distribution of the convection coefficients with a wider range from the minimum to the maximum of the CFD data than in the experimental reference data. A further simulation carried out using the standard BSL-RSM implemented in CFX led to results very similar to that of the EASM but about 4% lower on average; convergence was significantly slower with the standard BSL-RSM than with the EASM.

The CFD results help identifying features of the flow field and can partially explain the distribution of convection coefficients. From Figure 12.13 and Table 12.3 can be concluded that absolute local numbers may be off by more than 50%, yet the arithmetically averaged numbers agree better than the local ones. The RSM with explicit algebraic heat flux model yields results better than the simpler SST model but underpredicts the measured values by 25%. It is comforting, however, that the CFD calculated values are lower rather than higher compared to the measured data; for that reason a heat exchanger designed with CFD may perform better in reality than predicted.

13. Conclusions and Future Prospects

A novel method to measure local heat transfer coefficients on heat exchanger surfaces is presented in this thesis. The method is based on steady temperature oscillations induced into the heat-transferring wall by radiant heating through high power laser or incandescent lights. The surface temperatures are measured with an IR camera and processed to yield the phase delay between the heat flux and the temperature oscillation. From these data, the local heat transfer coefficients are derived by solving the ill-posed inverse problem iteratively with a complex number finite-difference model of the heat exchanger wall. This Temperature Oscillation IR Thermography (TOIRT) method has been successfully validated against empirical correlations, numerical simulations and experimental data from collaborating researchers. The TOIRT showed advantages compared to alternative measurement methods, including its following characteristics:

- Fast and simple
- Contact free and without fluid interaction
- Calibration free

The method was applied in this study to measure heat transfer in a pipe, at impinging air jets, at spray cooling systems, at vortex generators and in a plate heat exchanger. The results achieved with the TOIRT method are previously unreported maps of local heat transfer coefficients and were published in several scientific papers.

Theoretical considerations led to two equations for the area-mean heat transfer coefficient based on the local values, depending on the thermal boundary conditions. For a given distribution of local heat transfer coefficients, the mean heat transfer coefficient is higher for a constant temperature case than for constant wall heat flux. In real applications the mean heat transfer coefficient will be between these two limits.

From the experiments with vortex generator arrays at turbulent Reynolds numbers in a wind tunnel was found that an inline arrangement leads to higher heat transfer than a staggered array. The data from the vortex generator measurements agreed well with the data from collaborating researchers using the ammonia absorption and the TLC method.

For the spray cooling system, the local and area-integrated heat transfer coefficients revealed a significant maldistribution of heat transfer performance due to nozzle manufacturing tolerances, flow interaction and uneven draining, which are important findings for the design of next generation electronics cooling systems.

For the PHE, local distributions of the heat transfer coefficients with turbulent water have been obtained at three turbulent Reynolds numbers. The area-integrated values compare very well with literature data. The local values show a wide range with high peaks and a characteristic periodic distribution. The measurements also allowed identifying the flow distribution over the entire plate channel, which is remarkable even.

CFD simulations of a unitary cell of the PHE geometry employing an SST and an advanced Reynolds-Stress turbulence model were carried out. As far as CFD may have come today, the current results have shown that accurately predicting the turbulent heat flux in complex internal flow still poses a great challenge. The CFD results underpredict the measured heat transfer coefficients in turbulent flow. The RSM extended with an explicit algebraic stress heat flux model performed significantly better than the SST turbulence model, yielding an averaged convection coefficient that is 25% instead of 33% lower than the reference data. The simulations showed the capabilities and limits of the turbulence models and the observed flow features helped to explain the local heat transfer distribution of PHE's.

A future prospect is to use a further improved version of these advanced turbulent heat transfer models during design optimization of heat transfer devices such as plate heat exchangers. To optimize the geometry of heat transfer equipment, the conflict of simultaneously minimizing pressure loss and maximizing heat transfer can be solved with an objective of minimum total entropy generation. A comprehensive optimization approach would be an iterative CAD-CFD simulation process minimizing the entropy generation rate, that is based on CFD modeling like presented in this study combined with CAD geometry and grid modification. Finally, yet importantly, the author likes to note that no computer simulation whatsoever (not even ANSYS) will ever reproduce the pain and tediousness of real experiments.

13 Appendix

13.1 Matlab Script for Obtaining the Phase Delay from IR Camera Temperature Data

```
%IR Measured Temperature Data Analysis Tool
%Including data reading, drift compensation, square wave phase synchronization,
fourier analysis
format short g;
format compact;

%Read IR Data Files
clear;
name = 'IRDataFileName';

%Load multiple data files
path = strcat('D:\IRData\Folder\',name,'\');
first = 1; %First frame number
last = 600; %Last frame number
xmax = 320;
ymax = 256;
l = floor((last-first)+1);
m = single(zeros(ymax,xmax,l));% Memory preallocation
for i = start:ende
    fullname = strcat(path,name,int2str(i),'.MAT');
    s = load(fullname);
    k = round((i-first)+1); %Imageindex in array
    m(:,:,k) = single(s.(strcat(name,int2str(i))));
end
imax = max(k);
clear s path fullname first last l i k;
pack;

%Load single data file
load(strcat('D:\IRData\Folder\',name));
[xmax ymax imax] = size(imgseq);
m = (permute(imgseq,[2 1 3]));
clear imgseq;

% Evaluation Area Reduction
evalareax=(1+0:320-0);
evalareay=(1+0:256-0);
m = single(m(evalareay,evalareax,:));
pack;

% Calibration, optional
pcal = fliplr([1.361657e+003    -7.021147e-001  1.853623e-004   -2.546997e-008
1.938274e-012   -7.764084e-017  1.280581e-021]);
m = polyval(pcal, m);

%Fourier Analysis for Array m with n Periods of Measured Temperatures
[ymax, xmax, imax] = size(m);

p = 5; %Length of Periode s
dt = 1/40; %Time step per image for FPA
dtpix = 1.8021915e-6;  %Time step per pixel for Scanner Agema 900
tint = dtpix*xmax*ymax; %integration time from first pixel to full frame for
Scanner
dt = 1/round(1/tint);%Time step per image for Scanner Agema 900
tdelay = 0.01; %Heat source time delay; for laser: .01s, for halogen spot array
10s: .155s  / 5s: .139s / 8s: 0.147s
```

```
n = floor(imax*dt/p); %Number of periods in array
imax = n*p/dt;
i = 1:imax; %Image index in array
drift = 1; %Average temperature drift per period
LDC = 1; %Switch and counter for Linear Drift Compensation

%Drift Compensation and Mean Temperature
while drift^2 > 5*10^(-4)
    TmeanP = zeros(ymax,xmax,n);
    for pn = 1:n %period-wise
        ip = floor((pn-1)*p/dt+1:pn*p/dt); %Image index in n-th period
        for y = 1:ymax
            for x = 1:xmax
                TmeanP(y,x,pn) = sum(squeeze(m(y,x,ip)))/p*dt; %Period mean
temperature
            end
        end
    end
    Tmean = sum(TmeanP,3)/n; %Total mean temperature
    drift = (mean(mean(TmeanP(:,:,n)))-mean(mean(TmeanP(:,:,1))))/n; %average drift
per period

    %Linear Drift Compensation
    if  LDC >= 1
        Tdrift = single(zeros(ymax,xmax,imax)); %Memory preallocation
        for pn = 1:n %period-wise
            for ip = 1:round(p/dt) %image index in one period
                if (pn == 1)
                    Tdrift(:,:,ip) = ((TmeanP(:,:,pn+1) - TmeanP(:,:,pn)))*((ip-
1)/p*dt)+TmeanP(:,:,pn)-Tmean;
                elseif (pn==n)
                    Tdrift(:,:,ip+(n-1)*round(p/dt)) = ((TmeanP(:,:,pn)-
TmeanP(:,:,pn-1)))*((ip-1)/p*dt)+TmeanP(:,:,pn)-Tmean;
                else
                    Tdrift(:,:,ip+(pn-1)*round(p/dt)) = ((TmeanP(:,:,pn+1)-
TmeanP(:,:,pn-1))/2)*((ip-1)/p*dt)+TmeanP(:,:,pn)-Tmean;
                end;
            end
        end
        m = m - Tdrift;
        if LDC == 1
            Tdrifttotal = squeeze(Tdrift(:,:,imax)-Tdrift(:,:,1));
        end;
        LDC = LDC + 1;
    end;
if LDC == 0
    break;
end;
end;
clear TmeanP Tdrift;
m = m - min(min(min(m))); %Scale data by removing constant part
mmean(i) =squeeze(mean(mean(m(:,:,i))));%scaled frame mean temperature

%Square Wave Max/Min Phase Synchronization FOR 50% SQUARE WAVE HEAT FLUX ONLY
SPS = 1;% Curve fitting options:   0: =Off, 1: =Polyfit, 2: =Exponential sum fit,
3: =Linear fit

if SPS == 0
    nullphase = 0;
    sps_quality = [0;0];
end

if SPS == 1
for lrange = 1:2 %Sometimes the extrema can only be found in wider range
maxphase(1:n) = 0;
minphase(1:n) = 0;
for pn = 1:n %Period-wise
```

```
    ip = floor((pn-1)*p/dt+1:pn*p/dt-floor(pn/n)); %Image index in n-th period
    warning('');
    maxindices(pn) = find(diff(mmean(ip)) == min(diff(mmean(ip))))+round((pn-
1)*p/dt-lrange+1);%index Min diff each periode
    if maxindices(pn)-6 > 0 && maxindices(pn)+3 <= imax
        maxindices(pn) = find(mmean(maxindices(pn)-2:maxindices(pn)) ==
max(mmean(maxindices(pn)-2:maxindices(pn))))+maxindices(pn)-3;%index Max value near
Min diff
        if maxindices(pn) <= round((pn)*p/dt) && maxindices(pn) > round((pn-
1)*p/dt) %check if maxindices(pn) within pn
            fc1 = polyfit(maxindices(pn)-8:maxindices(pn)-1, mmean(maxindices(pn)-
8:maxindices(pn)-1),1);
            fc2 = polyfit(maxindices(pn)+1:maxindices(pn)+3,
mmean(maxindices(pn)+1:maxindices(pn)+3),2);
            x0 = [-(fc2(2)-fc1(1))/2/fc2(1) + sqrt((((fc2(2)-fc1(1))/fc2(1))^2)/4-
(fc2(3)-fc1(2))/fc2(1)), -(fc2(2)-fc1(1))/2/fc2(1) - sqrt((((fc2(2)-
fc1(1))/fc2(1))^2)/4-(fc2(3)-fc1(2))/fc2(1))]; %intersection of polyfits = actual
maxima
            if imag(x0) == 0
                if abs(maxindices(pn)-x0(1)) < abs(maxindices(pn)-x0(2))
                    maxindex(pn) = x0(1)-round((pn-1)*p/dt);
                else
                    maxindex(pn) = x0(2)-round((pn-1)*p/dt);
                end
                maxphase(pn) = 2*pi/p*((maxindex(pn)-1)*dt)-pi; % +tint/2 for
scanner
            end
        end
    end
    warning('');
    minindices(pn) = find(diff(mmean(ip)) == max(diff(mmean(ip))))+round((pn-
1)*p/dt-lrange+1);%index Max diff each periode
    if minindices(pn)-6 > 0 && minindices(pn)+3 <= imax
        fc1 = polyfit(minindices(pn)-8:minindices(pn)-1, mmean(minindices(pn)-
8:minindices(pn)-1),1);
        fc2 = polyfit(minindices(pn)+1:minindices(pn)+3,
mmean(minindices(pn)+1:minindices(pn)+3),2);
        x0 = [-(fc2(2)-fc1(1))/2/fc2(1) + sqrt((((fc2(2)-fc1(1))/fc2(1))^2)/4-
(fc2(3)-fc1(2))/fc2(1)), -(fc2(2)-fc1(1))/2/fc2(1) - sqrt((((fc2(2)-
fc1(1))/fc2(1))^2)/4-(fc2(3)-fc1(2))/fc2(1))]; %intersection of polyfits = actual
maxima
        if imag(x0) == 0
            if abs(minindices(pn)-x0(1)) < abs(minindices(pn)-x0(2))
                minindex(pn) = x0(1)-round((pn-1)*p/dt);
            else
                minindex(pn) = x0(2)-round((pn-1)*p/dt);
            end
            if minindex(pn)+round((pn-1)*p/dt) > minindices(pn)
                minphase(pn) = 2*pi/p*((minindex(pn)-1)*dt); % +tint/2 for scanner
            end
            if minphase(pn) > pi
                minphase(pn) = minphase(pn) - 2*pi;
            end
        end
    end
end

nullphase = meansqwt(nonzeros([maxphase minphase])); %square mean-deviation
weighted average phase angle from all periods at zero time
sps_quality = [std(nonzeros([maxphase minphase]))/2/pi*p; numel(nonzeros([maxphase
minphase]))];
if sps_quality(1)/p > 0.01 warning('Phase Sync Error >1%!'); end;
if (sps_quality(2)/n >= 1 && sps_quality(1)/dt < 0.333) break; end;
end
end

if SPS == 2
maxphase(1:n) = 0;
```

```
minphase(1:n) = 0;
c_inc_guess = [10 0.01 -10 -0.01];
c_dec_guess = [10 -0.01 10 -0.01];
fitrange = round(1/50*p/dt)+5;
options = optimset('MaxIter',1e4,'MaxFunEvals',1e4);
for pn = 1:n %Period-wise
    ip = floor((pn-1)*p/dt+1:pn*p/dt-floor(pn/n)); %Image index in n-th period %
    maxindices(pn) = find(diff(mmean(ip)) == min(diff(mmean(ip))))+round((pn-
1)*p/dt);%index Min diff each periode
    if maxindices(pn)-fitrange > 0 && maxindices(pn)+fitrange <= imax
        maxindices(pn) = find(mmean(maxindices(pn)-2:maxindices(pn)) ==
max(mmean(maxindices(pn)-2:maxindices(pn))))+maxindices(pn)-3;%index Max value near
Min diff
        if maxindices(pn) <= round((pn)*p/dt) && maxindices(pn) > round((pn-
1)*p/dt) %check if maxindices(pn) within pn
            i_inc = maxindices(pn)-fitrange:maxindices(pn)-1;
            i_dec = maxindices(pn)+1:maxindices(pn)+fitrange;
            x = maxindices(pn)-fitrange:maxindices(pn)+fitrange;
            c_inc = exp2curvefit(i_inc-(maxindices(pn)-fitrange),
mmean(i_inc),c_inc_guess, options);
            c_dec = exp2curvefit(i_dec-(maxindices(pn)+1),
mmean(i_dec),c_dec_guess, options);
            fitdiff = @(x) (c_inc(1)*exp(c_inc(2)*(x-(maxindices(pn)-
fitrange))+c_inc(3)*exp(c_inc(4)*(x-(maxindices(pn)-fitrange)))) -
(c_dec(1)*exp(c_dec(2)*(x-(maxindices(pn)+1)))+c_dec(3)*exp(c_dec(4)*(x-
(maxindices(pn)+1))));
            maxindex(pn) = fzero(fitdiff,maxindices(pn))-round((pn-1)*p/dt);
            maxphase(pn) = 2*pi/p*((maxindex(pn)-1)*dt)-pi; % +tint/2 for scanner
            if maxphase(pn) <- pi
                maxphase(pn) = maxphase(pn) + pi;
            end
        end
    end
    minindices(pn) = find(diff(mmean(ip)) == max(diff(mmean(ip))))+round((pn-
1)*p/dt);%index Max diff each periode
    if minindices(pn)-fitrange > 0 && minindices(pn)+fitrange <= imax
        minindices(pn) = find(mmean(minindices(pn)-6:minindices(pn)) ==
min(mmean(minindices(pn)-6:minindices(pn))))+minindices(pn)-7;%index Min value near
Max diff
        i_inc = minindices(pn)+1:minindices(pn)+fitrange;
        i_dec = minindices(pn)-fitrange:minindices(pn)-1;
        x = minindices(pn)-fitrange:minindices(pn)+fitrange;
        c_inc = exp2curvefit(i_inc-(minindices(pn)+1), mmean(i_inc),c_inc_guess,
options);
        c_dec = exp2curvefit(i_dec-(minindices(pn)-fitrange),
mmean(i_dec),c_dec_guess, options);
        fitdiff = @(x) (c_inc(1)*exp(c_inc(2)*(x-
(minindices(pn)+1)))+c_inc(3)*exp(c_inc(4)*(x-(minindices(pn)+1)))) -
(c_dec(1)*exp(c_dec(2)*(x-(minindices(pn)-fitrange)))+c_dec(3)*exp(c_dec(4)*(x-
(minindices(pn)-fitrange))));
        minindex(pn) = fzero(fitdiff,minindices(pn))-round((pn-1)*p/dt);
        minphase(pn) = 2*pi/p*((minindex(pn)-1)*dt); % +tint/2 for scanner
        if minphase(pn) > pi
           minphase(pn) = minphase(pn) - 2*pi;
        end
    end
end
nullphase = meansqwt(nonzeros([maxphase minphase])); %square mean-deviation
weighted average phase angle from all periods at zero time
sps_quality = [std(nonzeros([maxphase minphase]))/2/pi*p; numel(nonzeros([maxphase
minphase]))];
if sps_quality(1)/p > 0.01 warning('Phase Sync Error >1%!'); end;
end

if SPS == 3
maxphase(1:n) = 0;
minphase(1:n) = 0;
for pn = 1:n %Period-wise
```

```
    ip = floor((pn-1)*p/dt+1:pn*p/dt-floor(pn/n)); %Image index in n-th period %
    maxindices(pn) = find(mmean(ip) == max(mmean(ip)))+round((pn-1)*p/dt);%index
Max value
    if maxindices(pn)-8 > 0 && maxindices(pn)+5 <= imax
        if maxindices(pn) <= round((pn)*p/dt) && maxindices(pn) > round((pn-
1)*p/dt) %check if maxindices(pn) within pn
            fc1 = polyfit(maxindices(pn)-8:maxindices(pn)-1, mmean(maxindices(pn)-
8:maxindices(pn)-1),1);
            fc2 = polyfit(maxindices(pn)+1:maxindices(pn)+5,
mmean(maxindices(pn)+1:maxindices(pn)+5),1);
            x0 = (fc1(2) - fc2(2)) / (fc2(1) - fc1(1));
            maxindex(pn) = x0-round((pn-1)*p/dt);
            maxphase(pn) = 2*pi/p*((maxindex(pn)-1)*dt)-pi; % +tint/2 for scanner
        end
    end
    minindices(pn) = find(mmean(ip) == min(mmean(ip)))+round((pn-1)*p/dt);%index
min value
    if minindices(pn)-8 > 0 && minindices(pn)+5 <= imax
        if minindices(pn) <= round((pn)*p/dt) && minindices(pn) > round((pn-
1)*p/dt) %check if minindices(pn) within pn
            fc1 = polyfit(minindices(pn)-8:minindices(pn)-1, mmean(minindices(pn)-
8:minindices(pn)-1),1);
            fc2 = polyfit(minindices(pn)+1:minindices(pn)+5,
mmean(minindices(pn)+1:minindices(pn)+5),1);
            x0 = (fc1(2) - fc2(2)) / (fc2(1) - fc1(1));
            minindex(pn) = x0-round((pn-1)*p/dt);
            minphase(pn) = 2*pi/p*((minindex(pn)-1)*dt); % +tint/2 for scanner
            if minphase(pn) > pi
               minphase(pn) = minphase(pn) - 2*pi;
            end
        end
    end
end
nullphase = meansqwt(nonzeros([maxphase minphase])); %square mean-deviation
weighted average phase angle from all periods at zero time
sps_quality = [std(nonzeros([maxphase minphase]))/2/pi*p; numel(nonzeros([maxphase
minphase]))];
if sps_quality(1)/p > 0.01 warning('Phase Sync Error >1%!'); end;
end

if nullphase > pi
    nullphase = nullphase -2*pi;
end%SPS

%SFD Fourier Transformation
a = zeros(ymax,xmax); %preallocation 1st fourier coefficient
b = zeros(ymax,xmax); %preallocation 2nd fourier coefficient
t = (i-1).*dt;
for y = 1:ymax
    for x = 1:xmax
        a(y,x) = 2*sum(squeeze(m(y,x,i))'.*cos(2*pi/p.*t))/imax; %For FPA
        b(y,x) = 2*sum(squeeze(m(y,x,i))'.*sin(2*pi/p.*t))/imax; %For FPA
        a(y,x) = 2/imax*sum(squeeze(m(y,x,i))'.*cos(2*pi/p.*(i.*dt-dt+((x-1)+(y-
1)*xmax)*dtpix))); %For scanner
        b(y,x) = 2/imax*sum(squeeze(m(y,x,i))'.*sin(2*pi/p.*(i.*dt-dt+((x-1)+(y-
1)*xmax)*dtpix))); %For scanner

    end
end
amp = sqrt(a.^2+b.^2);
phi = min(max(atan2(a,b) + nullphase + tdelay/p*2*pi, -pi/2),0); %phase lag must be
-pi/2 < phi <0

%Image Results
colormap jet(32);
subplot(4,1,1), imagesc(phi), colorbar, title('Phase');
subplot(4,1,2), imagesc(amp), colorbar, title('Amplitude');
subplot(4,1,3), imagesc(Tmean), colorbar, title('Mean');
```

```
if LDC >= 1
subplot(4,1,4), imagesc(Tdrifttotal), colorbar, title('Drift');
end
set(gcf,'Position',[200,50,600,850]);

%Final Evaluation Area Cropping and Saving of Results
evalareax=(1+0:xmax-0);
evalareay=(1+0:ymax-0);
phi_full = phi;
phi = phi(evalareay,evalareax);

phi_ave = mean(mean(phi));
stdev = mean(std(phi));

save 'phi' name phi phi_full p;
name
phi_result = [phi_ave; stdev]
sps_quality
```

13.2 Matlab Script for 3D FDM Computation of the Local Heat Transfer Coefficients

```
%3D FDM Harmonic Conductive Wall Model to Compute Local Convection Coefficients
clear;
format short g;
format compact;

length = 27; %x-length in mm
d = 0.000605; %Thickness
xmax = 54; %Number of nodes in x
dxy = 0.001*length/xmax; %Resolution in mm

%Load Experimental Data"
load('phi.mat');
w = 2*pi/p;

%Material
%'1.4401';
dens = 7980;
shc = 500;
thcond = 15;

%Scaling of measured phase data
sf = size(phi,2)/xmax;
[X,Y] = meshgrid(1:size(phi,2),1:size(phi,1));
[XI,YI] = meshgrid(1:sf:size(phi,2),1:sf:size(phi,1));
phi_exp = interp2(X,Y,phi,XI,YI);
clear X Y XI YI;
phi_exp = min(phi_exp,-.1); %Limit outliers

ymax = size(phi_exp,1);
zmax = 4;
m = xmax*ymax*zmax;
k = spalloc(m,m,m*7); %Memory Preallocation for Coefficient Matrix
u = zeros(m,1); %Solution Vector Preallocation

Rz = d/(zmax-1)/thcond/(dxy^2);
Rxy = dxy/thcond/(d*dxy)*zmax;
C = shc*dens*dxy^2*d/zmax;

h_0 = 3; %Outside convection coefficients
h_start = 13000; %Initial value
```

```
hmin = 1000;
hmax = 40000;
h = zeros(ymax,xmax);
h = (phi_exp+pi/2).^2*h_start;

%FDM Error Reduction Factor
NumErrCorr = 765000/thcond*d^2/p*exp(h_start/2700*sqrt(p)/thcond);
if NumErrCorr > 0.01
    warning('FDM Error Reduction Factor > 1%, check expected value h_start');
end;
phi_exp = phi_exp.*(1+NumErrCorr);

%Result Vector Including Surface Irradiation
q  = spalloc(m,1,xmax*ymax);
q(1:xmax*ymax) = - 3200*0.1/(xmax*ymax*dxy^2)*0.95*dxy^2; %Constant heat flux from
halogen lamps
rl = 30; %laser spot radius in mm where intensity is decreased to e^-1/2 = 0.6070
qpeak = 2500; %Laser peak value
for y = 1:ymax %Laser heat flux with Gaussian area distribution
    for x = 1:xmax
        j = x+(y-1)*xmax;
        r = sqrt((x-xmax/2)^2+(y-ymax/2)^2)/xmax*length;
        q(j) = -qpeak* exp(-1/2*(r/rl)^2)*dxy^2;
        qfield(y,x)=q(j);
    end
end

%Array of Surface Node Numbers
for y = 1:ymax
    for x = 1:xmax
        z1nodes(y,x) = x+(y-1)*xmax;
    end;
end;

%Coefficient Matrix
for z = 1:zmax
    for y = 1:ymax
        for x = 1:xmax
            j = x+(y-1)*xmax+(z-1)*(xmax*ymax);
            if (x<xmax)     k(j,j+1)        = 1/Rxy; end;
            if (x>1)        k(j,j-1)        = 1/Rxy; end;
            if (y<ymax)     k(j,j+xmax)     = 1/Rxy; end;
            if (y>1)        k(j,j-xmax)     = 1/Rxy; end;
            if (z<zmax)     k(j,j+xmax*ymax)= 1/Rz;  end;
            if (z>1)        k(j,j-xmax*ymax)= 1/Rz;  end;
            if (z==1)
                if ((x==1)|(x==xmax)|(y==1)|(y==ymax))
                            k(j,j)          = - 3/Rxy - 1/Rz - (i*w*C) -h_0*dxy^2;
%Upper edges
                else        k(j,j)          = - 4/Rxy - 1/Rz - (i*w*C) -h_0*dxy^2;
%Upper surface
                end;
           elseif (z==zmax)
                if ((x==1)|(x==xmax)|(y==1)|(y==ymax))
                            k(j,j)          = - 3/Rxy - 1/Rz - (i*w*C) -
h(y,x)*dxy^2; %Lower edges
                else        k(j,j)          = - 4/Rxy - 1/Rz - (i*w*C) -
h(y,x)*dxy^2; %Lower surface
                end;
            else
                            k(j,j)          = - 4/Rxy - 2/Rz - (i*w*C); %Middle
volume
                if ((x==1)|(x==xmax)|(y==1)|(y==ymax))
                            k(j,j)          = - 3/Rxy - 2/Rz - (i*w*C); %Side
surfaces
                end;
                if (((y==1)|(y==ymax)) && ((x==1)|(x==xmax)))
                            k(j,j)          = - 2/Rxy - 2/Rz - (i*w*C); %Side edges
```

```
                end;
            end;

            if (((z==1)|(z==zmax)) && ((y==1)|(y==ymax)) && ((x==1)|(x==xmax)))
                                k(j,j)          = k(j,j)+1/Rxy;  %Corners
            end;
        end
    end
end

%Iterative Solution
for iter = 1:50
    u = minres(k,q,1e-6,50,[],[],u);
    phi = angle(u(z1nodes)); % Phase Angle Surface Nodes
    phierror = (phi-phi_exp)./phi_exp;
    phierror = smoothm(phierror,1); %Light area smoothing
    phierrorRMS(iter) = sqrt(sum(sum(phierror.^2))/xmax/ymax);
    if (iter > 10) && (phierrorRMS(iter-1) < phierrorRMS(iter)) % Convergence
condition when divergence starts
        break;
    end;
    h_old = h;
    h = h_old.*(phierror+1).^(1.5-iter/50);
    h = smoothm(h,0.125);
    h = min(max(h,hmin),hmax);
    for y=1:ymax
        for x=1:xmax
            j=x+(y-1)*xmax +(zmax-1)*(xmax*ymax);
            k(j,j) = k(j,j)+(h_old(y,x)-h(y,x))*dxy^2;
        end;
    end;
end;
Amp = abs(u(z1nodes));

h_mean = numel(h)/sum(sum(1./h));
h_ave = mean(mean(h));
h_std = mean(std(h))/h_ave;
hresult = [h_ave;h_mean;phierrorRMS(iter)];
save(name, 'h', 'phi_exp', 'hresult');
name
hresult

%Image Results
colormap jet(32);
surf(h), title('h'), xlabel(strcat('x', ' [', num2str(dxy*1000), ' mm]')),
ylabel(strcat('y', ' [', num2str(dxy*1000), ' mm]')), zlabel('h [W/m2K]');
axis([1 xmax 1 ymax hmin hmax]);
```

13.3 Matlab Script for Compensation of the Fluid Velocity Temperature Oscillation Effect

```
%Fluid Temperature Oscillation Phase Compensation
%Surface from exponential sum curvefit in x and parabolic fit in y
phi_exp = phi;
[ymax xmax] = size(phi);
y=1:ymax;
for x=1:xmax;
    cy(x,:) = polyfit(y, phi_exp(:,x)',2);
end
x=1:xmax;
cx_guess = [-1 0.01 1 -0.01];
cx_guess = exp2curvefit(x, (cy(x,1)*4+cy(x,2)*2+cy(x,3))',cx_guess, options);
options = optimset('MaxFunEvals',1e4,'MaxIter',1e4);
```

```
for y=1:ymax;
    cx(y,:) = exp2curvefit(x, (cy(x,1)*y^2+cy(x,2)*y+cy(x,3))',cx_guess, options);
    cx_guess = cx(y,:); %pretty clever...
end
for y=1:ymax;
    for x=1:xmax;
        phifit(y,x) = cx(y,1)*exp(cx(y,2)*x)+cx(y,3)*exp(cx(y,4)*x);
    end
end
phi = phi_exp-phifit+max(max(phifit));
```

13.4 Matlab Function for Exponential Sum Curve Fitting

```
%Function exp2curvefit for fitting a sum of two exponential functions
function [estimates, model] = exp2curvefit(xdata, ydata, start_points, options)
if nargin < 4, options = optimset; end
model = @expfun;
estimates = fminsearch(model, start_points, options);
    function [sse, FittedCurve] = expfun(params)
        a = params(1);
        b = params(2);
        c = params(3);
        d = params(4);
        FittedCurve = a.*exp(b.*xdata)+c.*exp(d.*xdata);
        ErrorVector = FittedCurve - ydata;
        sse = sum(ErrorVector .^ 2);
    end
end
```

13.5 Matlab Function for Squared Mean-Deviation Weighted Average

```
%Function meansqwt for sqared mean-deviation weighted average
%minimizes influence of outliers on average data
function meansqwt = meansqwt(data);
    sqwt = 1./(data-mean(data)+1e-12).^2;
    meansqwt = sum(sqwt.*data)/sum(sqwt);
end
```

13.6 Matlab Function for Smoothing Matrices

```
%Function smoothm for 2-D data smoothing by averaging the surrounding values
%smoothing parameter weight = 0...8, 0:=off, 8:=equal weights of all 8 with r = 1
surrounding pixels
function out = smoothm(m, weight)
[ymax, xmax] = size(m);
out = zeros(ymax,xmax);
if weight
    for y=2:ymax-1
        for x=2:xmax-1
            out(y,x) = (8/weight*m(y,x)+8*mean([m(y-1,x-1) m(y-1,x) m(y-1,x+1)
m(y,x-1) m(y,x+1) m(y+1,x-1) m(y+1,x) m(y+1,x+1)]))/(8+8/weight);
        end;
```

```
    end;
    for x=2:xmax-1
        y = 1;
        out(y,x) = (8/weight*m(y,x)+5*mean([m(y,x-1) m(y,x+1) m(y+1,x-1) m(y+1,x)
m(y+1,x+1)]))/(5+8/weight);
        y = ymax;
        out(y,x) = (8/weight*m(y,x)+5*mean([m(y,x-1) m(y,x+1) m(y-1,x-1) m(y-1,x)
m(y-1,x+1)]))/(5+8/weight);    end;
    for y=2:ymax-1
        x = 1;
        out(y,x) = (8/weight*m(y,x)+5*mean([m(y-1,x) m(y+1,x) m(y-1,x+1) m(y,x+1)
m(y+1,x+1)]))/(5+8/weight);
        x = xmax;
        out(y,x) = (8/weight*m(y,x)+5*mean([m(y-1,x) m(y+1,x) m(y-1,x-1) m(y,x-1)
m(y+1,x-1)]))/(5+8/weight);
    end;
    out(1,1) =       (8/weight*m(1,1)+3*mean([m(2,1) m(1,2) m(2,2)]))/(3+8/weight);
    out(1,xmax) =    (8/weight*m(1,xmax)+3*mean([m(2,xmax) m(1,xmax-1) m(2,xmax-
1)]))/(3+8/weight);
    out(ymax,1) =    (8/weight*m(ymax,1)+3*mean([m(ymax,2) m(ymax-1,1) m(ymax-
1,2)]))/(3+8/weight);
    out(ymax,xmax) = (8/weight*m(ymax,xmax)+3*mean([m(ymax-1,xmax) m(ymax,xmax-1)
m(ymax-1,xmax-1)]))/(3+8/weight);
else
    out = m;
end;
```

References

Ahrend, U., M. Buchholz, R. Schmidt, J. Köhler (2006). "Investigation of the Relation between Turbulent Fluid Flow and Heat Transfer in Fin-and-Tube Heat Exchangers". 13th Int. Heat Transfer Conference, Sydney, Australia.

Ahrend, U., S. Freund, M. Henze, J. Koehler (2007). "Experimental and Numerical Investigations of Heat Transfer in Complex Internal Flows With Vortex Inducing Elements - Introduction to a Joint Project and Typical Results -". 6th Int. Conference on Enhanced, Compact and Ultra-Compact Heat Exchangers, Potsdam, Germany.

ANSYS CFX (2006). Release 11. Ansys, Inc.

ANSYS ICEM CFD (2007). Release 11. Ansys, Inc.

Astarita, T., G. Cardone, G.M. Carlomagno, C. Meola (2000). "A survey on infrared thermography for convective heat transfer measurements." Optics & Laser Technology 32: 593-610.

AT (2002). IRLockIn. Trittau, AT-Automation Technology GmbH.

AT (2004). AT-Automation Technology GmbH. Various personal correspondences.

Baehr, H.D., S. Kabelac (2006). Thermodynamik, 13th ed., Springer-Verlag.

Baehr, H.D., K. Stephan (2004). Wärme- und Stoffübertragung, 4th ed., Springer-Verlag.

Barrett, R., M. Berry, T. F. Chan, et al., (1994). Templates for the Solution of Linear Systems: Building Blocks for Iterative Methods, SIAM, Philadelphia.

Bejan, A. (1984). Convection Heat Transfer, John Wiley & Sons.

Bejan, A. (1996). Entropy Generation Minimization. CRC Press.

Bell, J.C., E.F. Katz (1949). "A Method of Measuring Heat Transfer Using Cyclic Temperature Variations". Heat Transfer and Fluid Mechanics Institute, Preprints of Papers, Stanford: 243-254.

Benim, A.C., M. Cagan and D. Gunes (2004). "Computational Analysis of Transient Heat Transfer in Turbulent Pipe Flow". Int. J. Thermal Sciences 43: 725–732.

Blomerius, H. (1997). Strömungsstruktur, Wärmeübergang und Druckverlust in Kanälen mit gewellten Oberflächen, Cuvillier Verlag, Göttingen.

Boelter, L.M.K. , G. Young, H.W. Iversen (1948). Technical Note 1451. "An Investigation of Aircraft Heaters XXVII - Distribution of Heat-Transfer Rate in the Entrance Section of a Circular Pipe". NACA, Washington, DC.

Broussely, M., A. Levick, G. Edwards (2004). "Thermal Conductivity Measurement by Photothermal Radiometry as Part of a Multi Property Laser Absorption Radiation Thermometry Instrument". 4th European Thermal Sciences Conference, Birmingham, UK.

Carloff, R., A. Pross, K.-H. Reichert (1994). "Temperature Oscillation Calorimetry in Stirred Tank Reactors with Variable Heat Transfer". Chemical Engineering & Technology 17: 406-413.

Carlomagno, G.M., T. Astarita, G. Cardone (2002). "Convective Heat Transfer and Infrared Thermography". Int. Symposium on Visualization and Imaging in Transport Phenomena, New York Academy of Sciences.

Carslaw, H.S., J.C. Jaeger (1959). Conduction of Heat in Solids, Oxford University Press, UK.

Ciofalo, M., I. Di Piazza (2002). "A Computational Approach to Conjugate Heat Transfer between Two Fluids in Plate Heat Exchangers of Arbitrary Geometry." Int. J. Heat Exchangers 3.

Ciofalo, M., I. Di Piazza, J.A. Stasiek (2000). "Investigation of Flow and Heat Transfer in Corrugated-Undulated Plate Heat Exchangers." Heat and Mass Transfer 36(5): 449-462.

Ciofalo, M., J.A. Stasiek, M.W. Collins (1996). "Investigation of Flow and Heat Transfer in Corrugated Passages - II. Numerical Simulations." Int. J. Heat and Mass Transfer 39(1): 156-192.

Cotler, A.C., E. R. Brown, V. Dhir, and M.C. Shaw (2004). "Chip Level Spray Cooling of an LD-MOSFET RF Power Amplifier". IEEE CPT Trans., 27:411–416.

Croce, G., H. Beaugendre, and W. G. Habashi (2002). "Numerical Simulation of Heat Transfer in Mist Flow". Numerical Heat Transfer, Part A, 42:139–152.

Dano, P. E., J. A. Liburdy, and K. Kanokjaruvijit (2005). "Flow Characteristics and Heat Transfer Performance of a Semi-Confined Array of Jets: Effect of Nozzle Geometry". Int. J. Heat and Mass Transfer, 48:691–701.

Dietz, C. F., M. Henze, S.O. Neumann, J. von Wolfersdorf, B. Weigand (2005). "Numerical and Experimental Investigation of Heat Transfer and Fluid Flow around a Vortex Generator using Explicit Algebraic Models for the Turbulent Heat Flux". ISABE 2005 - The 17th Symposium on Air Breathing Engines, Munich, Germany.

Dietz, C.F., M. Henze, S.O. Neumann, J. von Wolfersdorf, B. Weigand (2006). "The Effects of Vortex Structures on Heat Transfer and Flow Field Behind Multielement Arrays of Vortex Generators". 13th Int. Heat Transfer Conference, Sydney, NSW, Australia.

Dietz, C.F., M. Henze, S.O. Neumann, J. von Wolfersdorf, B. Weigand (2007). "Flow and Heat Transfer Investigations Behind Vortex Inducing Elements as Benchmark for Complex Turbulence Models". 6th Int. Conference on Enhanced, Compact and Ultra-Compact Heat Exchangers, Potsdam, Germany.

Dietz, C.F., S.O. Neumann, J. von Wolfersdorf, B. Weigand (2007). "A Comparative Study of the Performance of Explicit Algebraic Models for the Turbulent Heat Flux". Numerical Heat Transfer, Part A, 52 (2):101-126.

Etemad, S., B. Sundén (2007). CFD-Analysis of Fully Developed Turbulent Flow and Heat Transfer in a Unitary Cell of a Cross Corrugated Plate Pattern Heat Exchanger. ASME-JSME Summer Heat Transfer Conference, Vancouver, BC, Canada.

Farid, M. S.-E. (1991). Infrared Scanning in Conjunction with Boundary Element Method to Determine Convective Heat Transfer Coefficients. Mechanical Engineering, University of Florida.

Farina, D.J., J.M. Hacker, R.J. Moffat, J.K. Eaton (1993). "Illuminant invariant calibration of thermochromic liquid crystals". In R.J. Simoneau and B.F. Armaly, Visualization of Heat Transfer Processes, ASME HTD Vol. 252:1-11, 29th National Heat Transfer Conference, Atlanta, GA.

Fernandes, Carla S., Ricardo Dias, J.M. Nóbrega, Isabel M. Afonso, Luis F. Melo and João M. Maia (2005). "Simulation of Stirred Yoghurt Processing in Plate Heat Exchangers". Journal of Food Engineering 69.

Filonenko, G. K. (1954)."Hydraulic Resistance in Pipes"(in Russian). Teploenergetika 1, No. 4, 40-44.

Freund, S., S. Kabelac (2005). "Measurement of Local Convective Heat Transfer Coefficients with Temperature Oscillation IR Thermography and Radiant Heating". ASME Summer Heat Transfer Conference, San Francisco, CA, USA.

Freund, S., S. Kabelac (2006). "Local Heat Transfer Coefficients in Plate Heat Exchangers Measured with Temperature Oscillation IR Thermography". 13th Int. Heat Transfer Conference, Sydney, Australia.

Freund, S., S. Kabelac (2007). "IR Measurement of Temperature Oscillations to Investigate Convective Heat Transfer Coefficients on Heat Exchangers". To appear in Int. J. Heat Exchangers.

Freund, S., S. Kabelac (2007). "Local Heat Transfer Coefficients at Aerodynamic Vortex Generators Measured with Temperature Oscillation IR Thermography". 6th Int. Conference on Enhanced, Compact and Ultra-Compact Heat Exchangers, Potsdam, Germany.

Freund, S., A.G. Pautsch, T.A. Shedd, S. Kabelac (2007). "Local Heat Transfer Coefficients in Spray Cooling Systems Measured with Temperature Oscillation IR Thermography." Int. J. Heat and Mass Transfer.

Gaiser G., V. Kottke (1989). "Flow Phenomena and Local Heat and Mass Transfer in Corrugated Passages". Chem. Eng. Tech. 12: 400-405.

Gnielinski, V. (1975). "Neue Gleichungen für den Wärme- und Stoffübergang in turbulent durchströmten Rohren und Kanälen". Forschung im Ingenieurwesen 41(1): 8-16.

Grijspeerdt, K., B. Hazarika, D. Vucinic (2003). "Application of Computational Fluid Dynamics to Model the Hydrodynamics of Plate Heat Exchangers for Milk Processing". Journal of Food Engineering 57(3): 237-242.

Hausen, H. (1976). Wärmeübertragung im Gegenstrom, Gleichstrom und Kreuzstrom, Springer-Verlag Berlin Heidelberg New York.

Henning, C. D., Parker, R. (1967). "Transient Response of an Intrinsic Thermocouple". ASME Transactions, Journal of Heat Transfer 89: 146-154.

Henze, M., C. Dietz, B. Weigand, J. von Wolfersdorf, O. Neumann (2007). "Heat Transfer in Complex Internal Flows - Wedge Shaped Vortex Generators". 6th Int. Conference on Enhanced, Compact and Ultra-Compact Heat Exchangers, Potsdam, Germany.

Henze, M., C. Dietz, S.O. Neumann, J. von Wolfersdorf, B. Weigand (2005). "Heat Transfer Enhancement from Single Vortex Generators". ASME Turbo Expo GT2005: Power for Land, Sea and Air, June 6-9., Reno-Tahoe, NV, USA.

Herwig, H., C.H. Kautz (2007). Technische Thermodynamik. Eine Systematische Einführung, Pearson Studium.

Herwig, H., A. Moschallski (2006). Wärmeübertragung. Vieweg.

Hohmann, C., P. Stephan (2002). "Microscale Temperature Measurement at an Evaporating Liquid Meniscus". Experimental Thermal and Fluid Science 26(2-4): 157-162.

Horacek, B., J. Kim, and K. T. Kiger (2003). "Effects of Noncondensable Gas and Subcooling on the Spray Cooling of an Isothermal Surface". Proc. ASME IMECE2003-41680, Washington, D.C..

Horacek, B., K.T. Kiger, and J. Kim (2005). "Single Nozzle Spray Cooling Heat Transfer Mechanisms". Int. Journal of Heat and Mass Transfer, 48:1425– 1438.

Horny, N., B. Lannoy (2003). "Lock-In Thermography with A Focal Plane Array." Measurement Science and Technology 14: 439-443.

Incropera, F.P., D.P. DeWitt (1996). Introduction to Heat Transfer, John Wiley & Sons.

Kabelac, S., S. Freund (2007). "Local Two-Phase Flow Heat Transfer in Plate Heat Exchangers". ASME-JSME Summer Heat Transfer Conference, Vancouver, BC, Canada.

Kakac, S, R. K. Shah, W. Aung (1987). Handbook of Single-Phase Convective Heat Transfer, John Wiley & Sons.

Kays, W.M., M.E. Crawford and B. Weigand (2005). Convective Heat and Mass Transfer, McGraw-Hill.

Kays, W.M., A.L London (1984). Compact Heat Exchangers, 3rd ed., McGraw Hill.

Kho, T., H.U. Zettler, H. Müller-Steinhagen, D. Hughes (1997). "Effect of Flow Distribution on Scale Formation in Plate and Frame Heat Exchangers". 5th UK National Heat Transfer Conference, Institution of Chemical Engineers.

Lee, C., K. Lee, J. Senda and H, Fujimoto (2001). "A Study on the Spraywall Interaction Model Considering Degree of Superheat in the Wall Surface". Numerical Heat Transfer Part B: Fundamentals, 40(6): 495–513.

Lienhard IV, J.H., J.H. Lienhard V (2001). A Heat Transfer Textbook. Cambridge, MA, Phlogiston Press.

Lin, L., R. Ponnappan (2003). "Heat Transfer Characteristics of Spray Cooling in a Closed Loop". Int. Journal of Heat and Mass Transfer, 46(20): 3737– 3746.

Martin, H. (1977). "Heat and Mass Transfer Between Impinging Gas Jets and Solid Surfaces." Advances in Heat Transfer 13: 1-60.

Martin, H. (1997). Druckverlust und Wärmeübergang in Plattenwärmeübertragern. VDI Wärmeatlas, Springer-Verlag Berlin Heidelberg New York.

Matulla, H., A.F. Orlicek (1971). "Bestimmung der Wärmeübergangskoeffizienten in einem Doppelrohrwärmetauscher durch Frequenzganganalyse." Chemie-Ingenieur-Technologie 43(20): 1127-1130.

Menter, F. R. (1993). "Zonal Two Equation k-ω Turbulence Models for Aerodynamic Flows". AIAA 93 (2906).

Meola, C., G.M. Carlomagno, A. Squillace, G. Giorleo (2002). "Non-destructive Control of Industrial Materials by Means of Lock-In Thermography". Measurement Science and Technology 13: 1583–1590.

Merker, G.P. (1987). Konvektive Wärmeübertragung, Springer-Verlag.

Mudawar, I., K.A. Estes (1996). "Optimizing and Predicting CHF in Spray Cooling of a Square Surface". Journal of Heat Transfer, 118:672–679.

Muscio, A., E. Grinzato (2002). "The Lock-in Heating-Cooling Method for the Measurement of the Thermal Diffusivity of Solid Materials." Heat Transfer Engineering 23(2).

Myers, G.E. (1971). Analytical Methods in Conduction Heat Transfer, McGraw-Hill.

Özisik, M.N. (1993). Heat Conduction. John Wiley & Sons.

Paige, C.C., M.A. Saunders, "Solution of Sparse Indefinite Systems of Linear Equations". SIAM J. Numer. Anal., Vol.12, 1975, pp. 617-629.

Patankar, S. V., C. H. Liu, E. M. Sparrow (1977). "Fully Developed Flow and Heat Transfer in Ducts Having Streamwise-Periodic Variations of Cross-Sectional Area." ASME Transactions, Journal of Heat Transfer 99: 180-186.

Pautsch, A.G. (2004). Heat Transfer and Film Thickness Characteristics of Spray Cooling with Phase Change. Master’s thesis, University of Wisconsin-Madison.

Pautsch, A.G. and T.A. Shedd (2005). "Spray Impingement Cooling with Single- and Multiple-Nozzle Arrays Part I: Heat Transfer Data Using FC-72". Int. Journal Heat and Mass Transfer, 48: 3167–3175.

Pautsch, A.G. and T.A. Shedd (2006). "Adiabatic and Diabatic Measurements of the Liquid Film Thickness during Spray Cooling with FC-72". Int. Journal of Heat and Mass Transfer, 49:2610–2618. Proceedings of IPACK’01, The Pacific Rim/ASME International Electronic Packaging Technical Conference and Exhibition: 617–624.

Pautsch, G. (2001). "An overview on the System Packaging of the CRAY SV2 Supercomputer". Proc. IPACK’01, The Pacific Rim/ASME International Electronic Packaging Technical Conference and Exhibition: 617–624.

Prandtl, L. (1904). "Über Flüssigkeitsbewegung bei sehr kleiner Reibung". Int. Mathematiker-Kongress, Heidelberg, p. 484-491.

Prinzen, S. (1991). Experimentelle Bestimmung örtlicher Wärmeübergangskoeffizienten mittels Temperaturschwingungen der Wand, VDI-Verlag.

Rockni, M., T. Gaski (2001). "Predicting Turbulent Convective Heat Transfer in Fully Developed Duct Flows". Int. J. Heat and Fluid Flow 22: 381-392.

Roetzel, W., M. Wandelt (1997). "Temperature Oscillation Thermography as a Measurement Technique in Heat Transfer". Experimental Heat Transfer, Fluid Mechanics and Thermodynamics: 193-200.

Roetzel, W., Sarit K. Das, X. Luo (1994). "Measurement of the Heat Transfer Coefficient in Plate Heat Exchangers Using a Temperature Oscillation Technique". Int. J. Heat and Mass Transfer 37(1): 325-331.

Schlichting, H. (1979). Boundary-Layer Theory, McGraw-Hill.

Schmidt, J., H. Boye (2001). "Influence of Velocity and Size of the Droplets on the Heat Transfer in Spray Cooling". Chem. Eng. Technol 24(3): 255-260.

Shah, R.K., M.R. Heikal, B. Thonon, P. Tochon (2001). "Progress in the Numerical Analysis of Compact Heat Exchanger Surfaces". Advances in Heat Transfer 34.

Shedd, T. A. and A. G. Pautsch (2005). "Spray impingement cooling with single- and multiple-nozzle arrays Part II: Visualization and empirical models". Int. J. Heat and Mass Transfer, 48:3176–3184.

Siegel, R., Sparrow, E.M. (1959). "Turbulent Flow in a Circular Tube with Arbitrary Internal Heat Sources and Wall Heat Transfer". ASME Transactions, Journal of Heat Transfer: 280-287.

Stasiek, J.A. (1997). "Thermochromic Liquid Crystals and True Colour Image Processing in Heat Transfer and Fluid-Flow Research". Heat and Mass Transfer, 33:27–39.

Stasiek, J.A., M. W. Collins, M. Ciofalo, P. E. Chew (1996). "Investigation of Flow and Heat Transfer in Corrugated Passages - I. Experimental Results". Int. J. Heat and Mass Transfer 39(1): 149-164.

Thonon, B. (1995). "Echangeurs à plaques: dix ans de recherche au GRETh. Partie I. Ecoulements et transferts de chaleur en simple phase et double phase". Revue Générale de Thermique. Institut Français des Combustibles et de l'Énergie, Paris. 397: 77-90.

Turnbull, W.O., P.H. Oosthuizen (1998). "The Use of Square Wave Surface Heat Fluxes and Phase Delay Information to Measure Local Heat Transfer Coefficients". 11th Int. Heat Transfer Conference, Seoul, Korea.

Turnbull, W.O., W.E. Carscallen, T. Currie (2002). "A New Infrared Based Periodic Experimental Technique for Measuring Local Heat Transfer Coefficients". 12th Int. Heat Transfer Conference, Grenoble, France.

Utriainen, E., B. Sunden (2001). "A Numerical Investigation of Primary Surface Rounded Cross Wavy Ducts". Heat and Mass Transfer 38.

VDI-Wärmeatlas (1997). VDI-Wärmeatlas. Berlin, Heidelberg, New York, Springer-Verlag.

Wagner E., C. Sodtke, N. Schweizer, P. Stephan (2006). "Experimental study of nucleate boiling heat transfer under low gravity conditions using TLCs for high resolution temperature measurements". Heat Mass Transfer 42: 875–883.

Wandelt, M., W. Roetzel (1997). "Lock-In Thermography as a Measurement Technique in Heat Transfer". Quantitative Infrared Thermography 96 - Eurotherm Series 50: 189-194.

Wang, G., S.P.Vanka (1995). "Convective Heat Transfer in Periodic Wavy Passages". Int. J. Heat and Mass Transfer 38(17).

Younis, B.A., C.G. Speziale, T.T. Clark (2005). "A Rational Model for the Turbulent Scalar Fluxes". Proceedings Royal Society London, 461:575–594.

Zettler, H.U., H. Müller-Steinhagen, R.N.G. Foster, P. Fowles (2001). "Positron Emission Particle Tracking - A New Technique to Investigate the Flow Pattern in a Plate and Frame Heat Exchanger with Corrugated Plates". 3rd Int. Conference on Compact Heat Exchangers and Enhancement Technologies for the Process Industry, Davos, Switzerland.

Lebenslauf

Sebastian Freund, geboren 09.03.1978 in Hannover

Ausbildung

1997	Abitur in Hannover.
Seit 1997	Mitglied des Technischen Hilfswerks, Bergungsgruppe, Höhenrettungsgruppe.
09.1997 – 08.2001	Studium des Maschinenbaus an der Universität Hannover, Studienrichtung: Energie- und Verfahrenstechnik.
09.1999	Vordiplom an der Universität Hannover.
08.2001 – 01.2003	Studium Mechanical Engineering an der University of Wisconsin-Madison.
12.2002	Master of Science Mechanical Engineering University of Wisconsin-Madison.

Berufliche Tätigkeiten

02.2003 – 02.2004	Consulting Engineer am Industrial Refrigeration Consortium, Madison, WI.
Seit 03.2004	Wissenschaftlicher Mitarbeiter am Institut für Thermodynamik, Helmut-Schmidt-Universität Hamburg unter Leitung von Prof. Dr.-Ing. S. Kabelac

Hamburg, Dezember 2007